Complete theoretical optical characterization of axisymmetric nanostructures

By

Kenneth Holms, MSci

A thesis submitted for the
degree of Doctor of Philosophy
at the University of Strathclyde

Department of Physics

May 2010

Acknowledgments

Firstly I would like to thank my supervisors Francesco Papoff and Ben Hourahine. This work would not have been possible without their guidance, for which I am extremely grateful and I wish them every success in the future.
Thanks also to my friends, I'd like to say it wouldn't have been possible without them but that wouldn't be true: Cod, Hanlon, Griff, Edo, Craigy, PC, Fleming, Dougie, Sarah, John, Thomas. It never would've been as much fun without you all.
I'd like to thank Pat and Tom Craigie for their support, help, understanding and genuine interest in my studies. My time at university has been made much easier and more fun thanks to their presence and both Catriona and I are extremely grateful to them in so many ways.
To Jennifer, Stephen, Cameron and Niamh - family is the most important thing in life, and spending time with you has helped me keep a smile on my face even when I'm stressed, tired and feel like my head might explode. We both miss you all.
I wouldn't be where I am today without my parents. I thank them for the roof, the money, the food, the clothes, and - well - more of the money. The greatest thing my Mum and Dad have ever given me, however, is the belief in myself that I can achieve anything I set my mind to with hard work and dedication. That's not an easy thing to do for someone, but it's the defining quality of what it means to be great parent. For this, I thank them.
Finally, I met my wife Catriona just before I started my PhD, and if you'd told me then that in four years time I'd be a married homeowner living in the south of England, I wouldn't have believed you. Some people still don't believe me, actually. I won't go into every aspect of how my life has changed, but it has a direction and a focus now that I didn't realize was missing four years ago, and this work could not have been accomplished without her love.

For Catriona

Abstract

We find accurate optical responses of metallic and dielectric axisymmetric nanoparticles in the resonant region - where the particle has at least one dimension comparable to the excitation wavelength - at any point in space by defining surface Green functions (SGF's) for the particles in terms of a finite number of exact solutions of the Maxwell equations. We study both the near and far field properties of these particles, offering a flexibility that is unsurpassed by alternative techniques. For each problem, we carefully monitor the convergence and error in our solutions to justify our results, a process often overlooked in similar studies. By optimizing these SGF's, we minimize the error in our solutions and are able to study wide families of particles to examine how the size, shape and composition of the particles affects their optical properties at all points in space.

List of Publications

This thesis is based in the following publication:

1. K. Holms, B. Hourahine, F.Papoff, Calculation of internal and scattered fields of axisymmetric nanoparticles at any point in space, J. Opt. A 11, 054009 (2009).

Contents

List of Figures

Chapter 1

Introduction

We shall begin in this chapter by examining the historical background to modern electromagnetic analysis and highlighting why the optical properties of nanoparticles have received constant and varied scientific interest for well over one hundred years. We will outline the fundamental electromagnetic theory required throughout our study and introduce several modern solution methods used widely, specifically their advantages and limitations. Finally we will outline very briefly the general problem we wish to solve in this work.

1.1 A brief history of nano-optics

Nanoparticles are generally considered to be an invention of modern science, although they have a history that dates back thousands of years. They have been used for their striking optical properties as decoration in materials such as glass and pottery, albeit unknowingly, since Roman times [2]. Of course, at this time, there was no real understanding that the optical properties of these materials were due to the presence of very small particles which had intriguing optical properties. The use of nanomaterials in this capacity continued for thousands of years without any understanding of the mechanisms at work.

It was the chemist, Michael Faraday, who provided the first scientific

study of the optical properties of nanoparticles in his seminal 1847 publication [3]. In this work he outlined his findings that the optical properties of gold colloids differed from those of bulk gold. Many consider this to be the birth of the scientific field of nanoscience, even though the properties of these metallic nanoparticles was not fully understood at this time.

Some twenty-five years later and in the field of atmospherics, Lord Rayleigh outlined theory that showed that the blue sky could be explained by the scattering of light by small particles [4]. Assuming that the scatterers were small in comparison to the wavelength of the incident light, Rayleigh showed that the scattered intensity was inversely proportional to the fourth power of the wavelength of the incident light, and that this was in excellent agreement with the spectral distribution of the light experimentally observed. Although particles in air are typically smaller than the colloidal particles described by Faraday, Rayleigh's analysis made fundamental steps to the advancement of nanoscience by providing a mathematical description to the optical properties of small particles.

In the intermediate period between Rayleigh's research and the beginning of the 20^{th} century, there was a large gap in the theory of the optical properties of nanoparticles. Very small particles could be adequately described in the far field by Raleigh theory, while geometrical optics [5] could describe the properties of large particles. The range between these two extremes where the wavelength of excitation was comparable to the size of the particle - the so called resonant region - remained a theoretical gap.

It was not until 1908 that the German physicist Gustav Mie outlined a a theory for spheres that was independent of the relative size of the particle to the incident light [6]. Mie theory allowed the fields of interest to be determined at any point in space, but did not prove useful for decades to come due to the enormous amount of calculations required in an age before the advent of the computer.

Decades later, with the advent of the computer Mie theory became a

realistically usable theory and since WWII there has been an explosion in the number of scattering theories reliant on computational techniques. Due to the breadth of the field, we will not study all of the various techniques in this work but we will investigate some of the important areas of modern computational electromagnetics in more detail in Section. 1.5. For now, we shall move on to study from a modern perspective a few examples from the vast range of exciting particles that can be produced and the corresponding optical properties of these nanoparticles.

1.2 Nanoparticle production and types

The field of nanoscience is progressing at a rate faster than ever due to modern production techniques allowing the fabrication of wide ranges of sizes and shapes of materials from an equally wide variety of materials. The field of nanoparticle fabrication is a vast science in itself and we will not study all the production methods here. The main methods of fabrication, however, are by attrition [7], pyrolysis [8] and wet chemistry techniques [9]. Of primary interest to our study is the shapes, sizes and materials of particles that can be produced via these various methods. We will concern ourselves in this study with particles having a rotational axis of symmetry. This is not a significant limitation as most fabrication methods in practice produce rotationally symmetric particles. Also, many of the physical effects of interest we shall describe in Section. 1.3 are precisely due to the particle symmetries. In Fig. 1.1 [10] we show a selection of polystyrene nanoparticles which have been produced by so called "bottom down" techniques (spheres that have been reduced down by chemical processes to form new axisymmetric particles). We can see in Fig. 1.1 a wide range of both oblate and prolate nanoparticles and we will discover in our studies that these particles can have drastically different optical properties. Examples of commercially available metallic nanoparticles are shown in Fig. 1.2. The elongated metallic par-

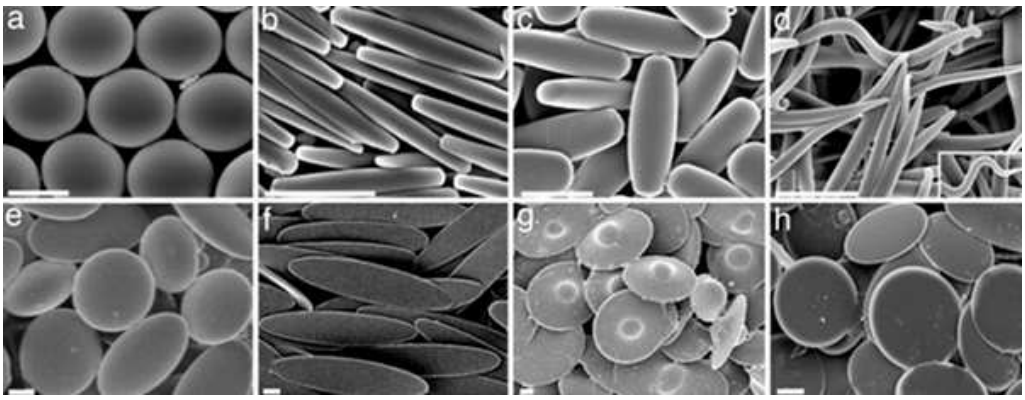

Figure 1.1: *Examples of various shapes of both prolate and oblate dielectric nanoparticles with a size range of* $500nm$ *shown on each.*

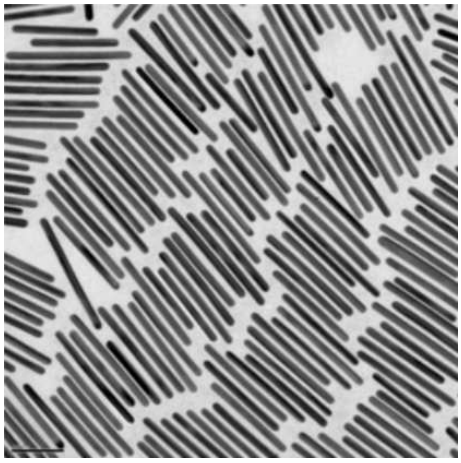

Figure 1.2: *Examples of commercially available elongated gold nanoparticles of length* $\approx 1\mu m$.

ticles shown in Fig. 1.2 have particularly interesting practical applications due to the high field enhancements possible with such particles, which we discuss further in Section. 1.3. As can be seen from the examples presented, elongated (and flat) nanoparticles tend in practice to have rounded edges as straight edges tend to be difficult to manufacture via the available production techniques. As a result, in this work we shall model most particles with rounded ends to recreate practically produced nanoparticles faithfully. These brief examples are by no means an exhaustive list of the variety of

nanoparticles that can be produced today, but serve to illustrate the variety of geometries available. Now that we have shown some of the various structures that can be produced with nanoparticles, in Section 1.3 we shall discuss some of the optical properties of these particles that makes them so interesting.

1.3 Optical properties of nanoparticles

Throughout the rest of this work we shall confine ourselves to study the optical properties of axisymmetric nanoparticles in the resonant region, between the limits of the Rayleigh regime and the regime of geometrical optics. We note, however, this is by no means any real restriction due to the wealth of optical properties nanoparticles in this range produce. We will briefly introduce some of the key properties of dielectric and metallic particles in both the near and far field.

1.3.1 Far field properties of particles

Although the majority of recent interest in nanoparticles has been in near field effects, accurately modeling the far-field properties of nanoparticles is of great interest in many different fields. In atmospherics, the ability to study how satellite communications are affected by clouds, dust and ice is of importance [11]. Also, the investigation of the optical properties of cosmic dust grains detected in astronomical objects is of importance in astrophysics [12].

1.3.2 Near field effects

Nanojets

Photonic nanojets are intense, narrow beams emerging from the shadow side surface of plane wave illuminated dielectric cylinders or spheres of diameter

greater than approximately one wavelength [13]. Nanojets can appear for a wide range of diameters of the cylinder or sphere and for a variety of refractive indices [14]. Typically, the jets can propagate with little divergence for several wavelengths into the surrounding medium while maintaining a transverse beam width smaller than the illuminating wavelength. In fact, transverse beam widths as small as 0.3λ have been reported [15]. We show a real nanojet imaged via confocal microscopy in Fig. 1.3. Nanojets such as

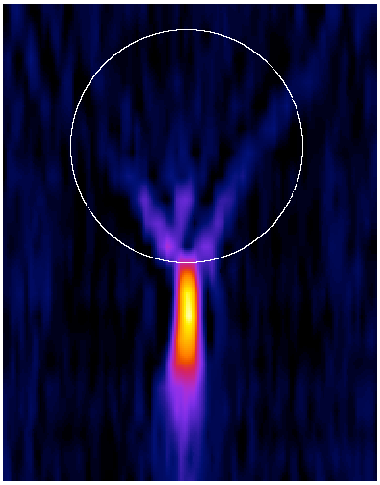

Figure 1.3: *Image of an experimentally observed photonic nanojet from a dielectric sphere of radius* $2.5\mu m$ *taken via confocal microscopy [1]. The intensity of the field has been sampled around the particle via confocal microscopy and a composite image formed to show the spatial variation.*

the example shown in Fig. 1.3 have received significant interest recently as obtaining the finest possible optical resolution is of relevance to a wide range of areas. Potential applications include high-density optical data storage [15] and microscopy [16], where nanojet microscopy obviously holds many advantages over conventional electron microscope based techniques, since in biological applications the sample need not be killed to be imaged.

Nano resonators

Ever since the discovery of very high quality factor micro resonators in spherical particles [17] there has been constant interest in such structures along with a wide range of publications, many aiming to find the largest possible Q value particles. The interest in micro and nanoparticle resonators has been driven by the diverse range of related studies from investigations of strong coupling in quantum electrodynamics [18] to ultra-sensitive bio-sensing [19].

Surface Plasmon Resonances

One of the most exciting properties of metallic nanoparticles first described by Mie in 1908 is that the interaction of light with the particle can result in the collective oscillation of its free electrons. This oscillation is referred to as the surface plasmon resonance (SPR) [20].

This SPR can produce large optical polarizations which result in a huge local electric field enhancement at the nanoparticle surface as well as strongly enhanced light absorption and scattering by the particle, provided the incident field is at the SPR frequency. This SPR frequency depends not only on the material, but also on the size and shape of the nanoparticle [21, 22], the dielectric properties of the surrounding medium [23], and inter-particle interactions [24]. These properties provide a large degree of tunability to the response of the particle to the incident field.

These strongly enhanced and tunable absorption and scattering properties of such metal nanoparticles have made them invaluable as optical and spectroscopic tags for biological sensing and imaging [25] and for biomedical applications [26]. Also, the SPR sensitivity to the host medium refractive index and inter-particle interactions has also been used for the optical detection of biological and chemical species [27].

The huge local electric field resulting from the SPR can lead to a strong enhancement of the spectroscopic signal from molecules in the vicinity of an SPR active particle [28]. Important examples of this include surface enhanced

fluorescence [29], and surface-enhanced Raman scattering (SERS) [30, 31] with enhancement factors large enough to allow single molecular detection [32, 33].

A detailed understanding of the laws which govern electromagnetics is required in our studies, and we shall present a brief introduction in Section. 1.4.

1.4 Fundamentals of electromagnetics

The relationships showing the behavior of the macroscopic electric and magnetic fields in a media were formulated by James Clerk Maxwell and are of the form [34]:

$$\nabla \times \mathbf{E} = -\frac{\partial \mathbf{B}}{\partial t} \tag{1.1}$$

$$\nabla \times \mathbf{H} = \mathbf{J} + \frac{\partial \mathbf{D}}{\partial t} \tag{1.2}$$

$$\nabla \cdot \mathbf{D} = \rho \tag{1.3}$$

$$\nabla \cdot \mathbf{B} = 0 \tag{1.4}$$

where $\mathbf{E}$ is the electric field, $\mathbf{H}$ the magnetic field, $\mathbf{B}$ the magnetic induction, $\mathbf{D}$ the electric displacement, $\mathbf{J}$ the current density, ρ the free electric charge density and t is time.

Also, it is trivial to show from Maxwell's equations the continuity equation for electric charge is of the form

$$\nabla \cdot \mathbf{J} + \frac{\partial \rho}{\partial t} = 0 \tag{1.5}$$

Since the Gauss magnetic field law and the charge continuity equation can be obtained from the first three Maxwell's equations, they are sometimes thought of as being supplementary or dependent equations.

The charge and current densities are associated with free charges and for a source free medium $\mathbf{J} = 0$ and $\rho = 0$. For this case, only the first two of

Maxwell's equations are independent.

Throughout our study, we shall assume that the fields and sources are time harmonic with an angular frequency ω and can be written in the form

$$\mathbf{E}(\mathbf{r},t) = Re\{\mathbf{E}(\mathbf{r})e^{-i\omega t}\} \tag{1.6}$$

With similar relations for the other fields of interest. Thus it can be seen that in the time domain that the field $\mathbf{E}(\mathbf{r},t)$ is a real quantity. However, in the frequency domain $\mathbf{E}(\mathbf{r})$ is a complex quantity and Maxwell's laws in the frequency domain are of the form

$$\nabla \times \mathbf{E} = i\omega\mathbf{B} \tag{1.7}$$

$$\nabla \times \mathbf{H} = \mathbf{J} - i\omega\mathbf{D} \tag{1.8}$$

$$\nabla \cdot \mathbf{D} = \rho \tag{1.9}$$

$$\nabla \cdot \mathbf{B} = 0 \tag{1.10}$$

1.4.1 Boundary conditions

If more than one medium is involved, the fields at the boundary of two media may be discontinuous. However, a boundary condition is associated with each of Maxwell's equations. If we consider a boundary between two media separated by a surface S which has an outward unitary normal (see Appendix. C) vector $\hat{\mathbf{n}}$ as shown in Fig. 1.4 it is possible to show that the tangential component of $\mathbf{E}$ is continuous while the tangential component of $\mathbf{H}$ is discontinuous:

$$\hat{\mathbf{n}} \times (\mathbf{E_2} - \mathbf{E_1}) = 0 \tag{1.11}$$

$$\hat{\mathbf{n}} \times (\mathbf{H_2} - \mathbf{H_1}) = \mathbf{J}_s \tag{1.12}$$

Where $\mathbf{J}_s$ is the surface current density and, conversely, the normal component of $\mathbf{B}$ is continuous while the normal component of $\mathbf{D}$ is discontinuous:

$$\hat{\mathbf{n}} \cdot (\mathbf{B_2} - \mathbf{B_1}) = 0 \tag{1.13}$$

$$\hat{\mathbf{n}} \cdot (\mathbf{D_2} - \mathbf{D_1}) = \rho_s \tag{1.14}$$

where ρ_s is the surface charge density.

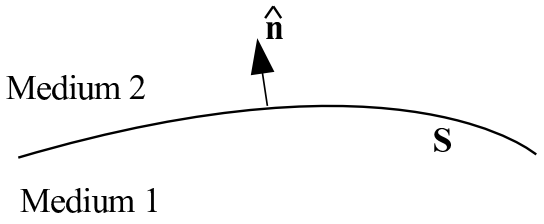

Figure 1.4: *The interface between two linear isotropic media showing the outward unitary normal at the surface S.*

1.4.2 Poynting's Theorem

Energy conservation follows from Maxwell's equations and Poynting's theorem in the time domain states that:

$$\nabla \cdot (\mathbf{E} \times \mathbf{H}) + \mathbf{H} \cdot \frac{\partial \mathbf{B}}{\partial t} + \mathbf{E} \cdot \frac{\partial \mathbf{D}}{\partial t} = -\mathbf{E} \cdot \mathbf{J} \tag{1.15}$$

and the Poynting vector is given by:

$$\mathbf{S} = \mathbf{E} \times \mathbf{H} \tag{1.16}$$

which be interpreted as the power flow density. By integrating over a finite domain D with surface S and using Gauss' theorem we find that:

$$-\int_D \mathbf{E} \cdot \mathbf{J} dV = \int_S \mathbf{S} \cdot \hat{\mathbf{n}} dS + \int_D \left(\mathbf{H} \cdot \frac{\partial \mathbf{B}}{\partial t} + \mathbf{E} \cdot \frac{\partial \mathbf{D}}{\partial t} \right) dV \tag{1.17}$$

Which simply describes that the power supplied by the sources within the volume is equal to the sum of the increase in electromagnetic energy flowing out of the volume.

In a similar fashion, the Poynting vector can be represented in the frequency domain as:

$$\nabla \cdot (\mathbf{E} \times \mathbf{H}) = i\omega(\mathbf{B} \cdot \mathbf{H}^* - \mathbf{E} \cdot \mathbf{D}^*) - \mathbf{E} \cdot \mathbf{J}^* \tag{1.18}$$

where the asterisk denotes the usual complex conjugation. The complex Poynting vector is defined as:

$$\mathbf{S} = \mathbf{E} \times \mathbf{H}^* \tag{1.19}$$

However, practically, it is not possible for real devices to respond at optical frequencies and so what is actually measured is the time averaged power flow. The time averaged Poynting vector is given by:

$$\langle \mathbf{S} \rangle = \frac{1}{2} Re\{\mathbf{E} \times \mathbf{H}^*\} \tag{1.20}$$

1.4.3 Constitutive Relations

The first three independent Maxwell's equations are, in themselves, insufficient to form a complete system of equations to solve for all unknown scalar functions since there are sixteen unknown scalar functions and only seven scalar differential equations.

If we consider a source free medium, the number of unknown scalar functions decreases to twelve with six scalar differential equations. To make the equations definite additional information is required about the interdependencies of the vector fields. This additional information is given by constitutive relations. We note that from this point onwards we will assume all fields to be time harmonic and so the frequency domain form of the Maxwell equations apply. The frequency domain constitutive relations for isotropic

media are:

$$\mathbf{D} = \epsilon \mathbf{E} \tag{1.21}$$

$$\mathbf{B} = \mu \mathbf{H} \tag{1.22}$$

$$\mathbf{J} = \sigma \mathbf{E} \;\; (Ohm's\ Law) \tag{1.23}$$

where ϵ is the electric permittivity, μ is the magnetic permeability and σ is the electric conductivity. The above equations provide nine scalar relations that make the number of equations and unknowns in Maxwell's equations compatible, and for the source free medium, only the first two constitutive relations are required. We draw special attention to Ohm's Law, which quantifies the conductivity (σ) of a medium. In this work we shall study the electromagnetic properties of real metallic materials that have finite conductivities and as such support internal fields to the particle. For the case of metallic particles, the large conductivity produces rapidly attenuated internal fields.

In free space, the electric permeability and magnetic susceptibility are given by $\epsilon_0 = 8.85 \times 10^{-12} Fm^{-1}$ and $\mu_0 = 4\pi \times 10^{-7} Hm^{-1}$ respectively. Inside a medium, however, the permeability and susceptibility are determined by the electric and magnetic properties of the medium.

Dielectric materials can be characterized by two terms, one free space term and one polarization vector term, $\mathbf{P}$, such that:

$$\mathbf{D} = \epsilon_0 \mathbf{E} + \mathbf{P} \tag{1.24}$$

where the polarization vector is the average electric dipole moment per unit volume and is quantified by:

$$\mathbf{P} = \epsilon_0 \chi_e \mathbf{E} \tag{1.25}$$

where χ is the electric susceptibility. Similarly, magnetic materials can be

described by a free space term and magnetization vector term, $\mathbf{M}$, such that:

$$\mathbf{B} = \mu_0\mathbf{H} + \mu_0\mathbf{M} \tag{1.26}$$

where M is the magnetic dipole moment per unit volume:

$$\mathbf{M} = \chi_m\mathbf{H} \tag{1.27}$$

where χ_m is the magnetic susceptibility. Throughout our study we shall deal only with nonmagnetic media where the permeability is given by $\mu = \mu_0$. For isotropic media, the permeability and susceptibility can be written as:

$$\epsilon = \epsilon_0\epsilon_r = \epsilon_0(1 + \chi_e) \tag{1.28}$$

$$\mu = \mu_0\mu_r = \mu_0(1 + \chi_m) \tag{1.29}$$

1.4.4 Index of Refraction

For source free media, the simplest solution to Maxwell's equations is the vector plane wave solution. The behavior of the plane wave is determined by the dispersion relation

$$k = \omega\sqrt{\epsilon\mu} \tag{1.30}$$

which relates the angular frequency of the wave, ω, to the wavenumber k. The dimensionless quantity

$$n = c\sqrt{\epsilon\mu} = c\sqrt{\epsilon_0\mu_0}\sqrt{\epsilon_r\mu_r} \tag{1.31}$$

is the refractive index of the medium where c is the speed of light (c=$1/\sqrt{\epsilon_0\mu_0}$), ϵ_0 and μ_0 are the free space permittivity and permeability and ϵ_r, μ_r are the relative permittivity and permeability of the material in question.

1.5 Computational electromagnetics

There are countless real-world situations where the interaction of electromagnetic radiation with structures is of great importance. Examples include the design and modeling of telecommunication systems, antenna, radar, satellite communication systems, the study of nanophotonic devices, high speed silicon electronics and medical imaging. However, very few of these problems are analytically solvable and as a result numerical methods must be employed. The multitude of methods that are employed in the solution of this broad range of problems forms the wide and growing field of computational electromagnetics. The typical aim of computational electromagnetic techniques is to solve the problem of computing the electric and magnetic fields in and around some object, which is subject to an incident excitation. Some solution methods allow the solution fields to be found across all space, while others only allow the fields to be found in a predefined area or grid. There are a wide variety of computational electromagnetic techniques and the exact method employed to solve a particular problem depends on the nature of the object being studied and the area for which a solution is desired. Almost all methods aim to take advantage of natural symmetries and three dimensional problems can often be reduced to problems of lower dimension providing a specific symmetry exists. In this work we are mainly interested in the simulation of how electromagnetic fields interact with axisymmetric nanostructures, and a brief overview of some of the main techniques used in this field as well as advantages and disadvantages of each will be outlined. Specifically, we will briefly outline Mie theory, the Finite Difference Time Domain method, the Discrete Dipole Approximation and the Extended Boundary Condition Method with Distributed Sources. Currently, these are the most widely used techniques in the study of the optical properties of nanoparticles.

1.5.1 Mie Theory

As we discussed in Section. 1.1, Gustav Mie's motivation was the characterization of the optical properties of colloids, which were mainly in the resonant region of the incident excitation, i.e. between the Rayleigh and geometrical optics limits. Mie ultimately formulated a solution to the scattering of electromagnetic plane waves by spheres and so Mie scattering theory is named after him.

Unlike Rayleigh scattering, Mie theory is applicable to all aspect ratios of particle size to incident light wavelength and is one of the few analytical solutions of the Maxwell equations for particles electromagnetics. It represents the various incident, internal and scattered fields as expansions of a set of functions and is an exact solution to Maxwell's equations provided infinite expansions are used. As previously discussed, at the time of its inception, Mie theory's viability was questionable since it required a large number of computations. The computer age has allowed the fast and accurate computation of these large sums of special functions, and as a result Mie's paper's influence continues even today and in fact Mie's original paper receives around 160 citations each year.

As we outlined in Section. 1.2, modern production techniques have allowed the manufacture of a wide range shapes of nanoparticles and Mie theory cannot be directly used to solve problems involving non-spherical particles. However, since scattering of a plane electromagnetic wave by a sphere is one of the few analytically solvable problems in electromagnetics, Mie theory is frequently used as a standard reference to validate methods designed for more complex electromagnetic problems.

1.5.2 Finite Difference Time Domain Method

The Finite Difference Time Domain (FDTD) method is a time domain method which involves the direct solution of Maxwell's time dependent curl equations

[35]. It uses simple central-difference approximations [36] to evaluate the space and time derivatives of the fields of interest. The region being studied is represented by two interlaced grids of discrete points. One grid contains the points at which the magnetic field is evaluated, the second contains the points at which the electric field is evaluated. By alternately calculating the electric and magnetic fields at a series of time steps, the fields of interest are propagated throughout the grid. Time stepping is continued until a steady state solution with appropriate precision is reached. The main advantages of the FDTD method are that is does not involve the solution of system of linear equations and frequency domain results can be obtained by applying a discrete Fourier transform to the time domain results. Also, the particle being studied can be of arbitrary shape and this makes the method particularly suited to the study of non-axisymmetric particles. There are however some significant disadvantages of the FDTD method. Firstly, the fields of interest can only be found on the predefined grid and, because the basic elements are cubes, curved surfaces on a scatterer must be stair- cased as illustrated in Fig. 1.5. Of course, by increasing the resolution of the FDTD method the area which is not modeled can be decreased arbitrarily, but in reality the computational requirements of the FDTD method are significant and increasing the resolution comes with significant additional computational cost. Furthermore, no matter how high the resolution is made, there will always be areas which are not modeled. Probably the most major disadvantage of the FDTD method, however, is that if either the particle or input field change, the entire calculation must be performed again. Since one calculation can take hours or even days to complete, it makes evaluating the behavior of a particle for a range of incident fields difficult. For these reasons, FDTD methods tend to be used to periodically confirm the results of other more efficient computational methods.

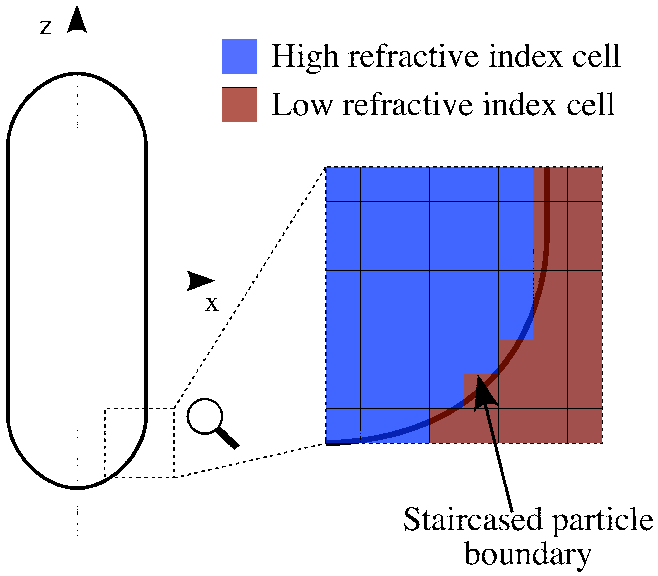

Figure 1.5: *A diagramatical representation of a staircasing effect in the near field of a particle calculated via the FDTD method.*

1.5.3 Discrete Dipole Approximation

One of the most most well known and widely used methods in computational scattering analysis is the Discrete Dipole Approximation (DDA) [37]. Using DDA, an arbitrarily shaped particle is treated as three dimensional collection of dipoles. When subject to an incident field, the points acquire dipole moments which interact with one another as well as the incident field. For this reason the DDA is also sometimes referred to as the coupled dipole approximation. By taking into account the interaction of all the dipoles with each other and the incident field, it is possible to form a linear system of equations, and, by solving this system the fields of interest may be found. DDA has the main advantage that the dipoles that form the object can be placed in any configuration and so even irregularly shaped particles without any symmetry can be studied. However, the main disadvantage of DDA (as with FDTD) is that the linear equations generated need to be solved for each incident field which can be computationally demanding.

1.5.4 Extended Boundary Condition Method with distributed sources

The Extended Boundary Condition Method (EBCM) is a multipole method which connects the coefficients of the expansions of the scattered and incident fields in terms of a complete system of the vector basis functions via a matrix commonly known as the T-Matrix. It was first described by Waterman in his seminal paper [38]. Due to the matrix relations between the expansion coefficients being at the heart of the theory, the EBCM is often referred to as the T-Matrix method. There have been many modifications of the EBCM since its inception, for elongated or flat particles the most important modification of the EBCM is use of distributed multipole sources within the particle, as opposed to sources defined from a single origin [39].

The main advantages of the distributed source formulation of the EBCM are the low computational costs and wide range of particle shapes, materials and sizes that can be modeled [40]. One of the major drawbacks of the EBCM, however, is the inability to model the near field effects of many of the particles it can model in the far field. This is due to the fact that the method can only determine the fields inside and outside the particles smallest and largest circumscribing spheres respectively as shown in Fig. 1.6. The volume of space that cannot be modeled in the near field increases as the aspect ratio increases, making this method unsuitable for near field studies in non spherical particles. Due to this limitation, the method is primarily used in far field studies where this disadvantage is not important.

1.6 Statement of our problem

In this study, we wish to characterize the electromagnetic fields at all points in space due to an input field being imposed on an axisymmetric nanoparticle. We assume that the nanoparticle and surrounding medium are both

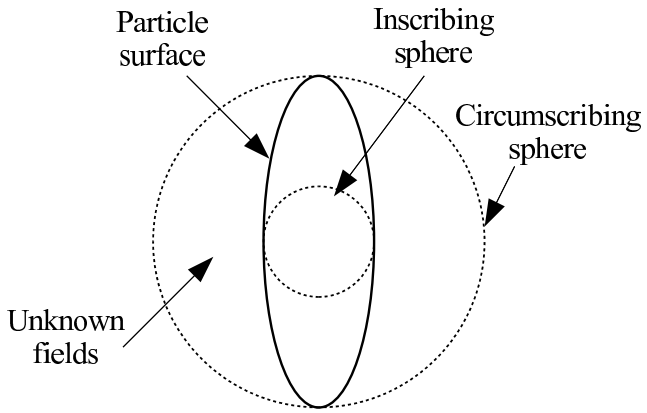

Figure 1.6: *Near field diagram showing the area between the inscribing and circumscribing spheres that the EBCM with distributed sources cannot find, the main limitation of the model.*

linear and isotropic, and that the surrounding medium is infinitely extended. A diagramatical representation of a particle with an input field incident upon it is shown in Fig. 1.7. We note in Fig. 1.7 that the particle is axisymmetric since it is produced by the revolution of the generatrix about the symmetry axis (the z-axis). We will make use of both Cartesian and spherical polar coordinates in this work, the relationship between the two is given in Appendix. A.

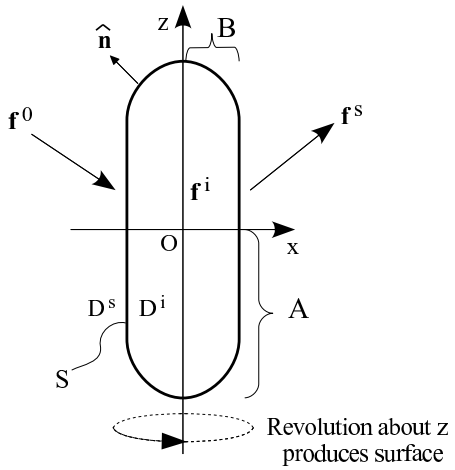

Figure 1.7: *The geometry of a general particle we wish to model showing the surface S separating the internal and external domains D^i and D^s, the incident, internal and scattered fields $\mathbf{f}^{0,i,s}$ (which can be electric or magnetic), the outward unitary normal to the surface $\hat{\mathbf{n}}$ and the major and minor semi axes A, B along z and x, respectively. The surface of the particle is produced by the revolution of a line, or generatrix, about the z axis.*

Chapter 2

Electromagnetic Properties via the Surface Green Function

In this chapter we shall lay down the theory that will enable us to find the electromagnetic properties of axisymmetric nanoparticles as described in Section. 1.6.

2.1 Multipole expansions in electromagnetics

In this study, we represent electric and magnetic fields as expansions over some set of appropriate functions. We deem functions to be appropriate if they satisfy certain criteria. Firstly, we require that the functions are exact solutions to the Maxwell equations. In this way, we can be assured that any linear combination of these functions we produce via a multipole expansion are also solutions to the Maxwell equations. We also require that our functions (and hence field expansions) satisfy the radiation condition at infinity [41]:

$$\frac{\mathbf{r}}{r} \times \sqrt{\mu_s}\mathbf{H}^s + \sqrt{\epsilon_s}\mathbf{E}^s = 0(\frac{1}{r}), \quad as \quad r \to \infty \tag{2.1}$$

The radiation condition assures that the scattered fields propagate away from the particle i.e. the energy of the scattered field propagates outward from

the particle and assures uniqueness in our solutions. Additionally, we require that the set of functions we use is complete and linearly independent [42]. Requiring the functions to be complete ensures that we can represent any field in our multipole expansions to an arbitrary precision by carrying out the expansion to high enough order. Linear independence ensures that the there is no degeneracy in our system of functions. There are many sets of functions which satisfy these criteria [43] , although we choose to work with the Spherical Vector Wavefunctions (SVWF's) $\mathbf{M}$ and $\mathbf{N}$ which are introduced in detail in Appendix. B.

The expansions of the various fields are written in terms sums over the SVWF's such that for the internal field:

$$\mathbf{E}^i = \sum_{n=1}^{\infty} \sum_{m=-n}^{n} a_{mn}^i \mathbf{M}_{mn}^1 + b_{mn}^i \mathbf{N}_{mn}^1 \tag{2.2}$$

and for the scattered field

$$\mathbf{E}^s = \sum_{n=1}^{\infty} \sum_{m=-n}^{n} a_{mn}^s \mathbf{M}_{mn}^3 + b_{mn}^s \mathbf{N}_{mn}^3 \tag{2.3}$$

where m, n are the indices of the SVWF's $\mathbf{M}$ and $\mathbf{N}$ (m is the azimuthal mode and n is the order of the Legendre polynomial within the SVWF), $1, 3$ specify the type of radial function within the SVWF (1 specifies the regular functions used for expanding the incident and internal fields in terms of Bessel functions and 3 specifies the radiating functions used for expanding the scattered fields which are in terms of Hankel functions.) and $a_{mn}^{i,s}$ and $b_{mn}^{i,s}$ are the expansion coefficients for the internal and scattered fields. There are of course similar relations for the magnetic fields.

Practically, however, we must use truncated expansions and so the sums

in the above expressions become:

$$\sum_{n=1}^{\infty}\sum_{m=-n}^{n} \rightarrow \sum_{n=1}^{N}\sum_{m=-M}^{M} \tag{2.4}$$

where N, M are the truncation parameters for n, m that control the size of the sum.

Throughout our study, we will refrain from writing out such bulky expansions, instead we use the compact notation which combines the electric and magnetic fields as:

$$|\mathcal{F}^{i/s}> = |\mathbf{E}^{i/s}, \mathbf{H}^{i/s}> = c^{i/s}_{\nu/\mu}|\mathbf{F}^{i/s}_{\nu/\mu}> \tag{2.5}$$

where $\mathcal{F}^i$ represents the internal electric and magnetic fields we wish to approximate, c^i_ν contains the expansion coefficients, ν is a multi-index that contains both m and n, $\mathbf{F}_\nu$ contain the SVWF's such that $\mathbf{F}^i_\nu = |\mathbf{M}^i_\nu, -iC^i\mathbf{N}^i_\nu>$ for $1 \leq \nu \leq \nu_M/2$ and $\mathbf{F}^i_\nu = |\mathbf{N}^i_\nu, -iC^i\mathbf{M}^i_\nu>$ for $\nu_M/2+1 \leq \nu \leq \nu_M$ and ν_M is the number of functions we use in the expansion of the internal fields where $C^i = \sqrt{\frac{\epsilon^i}{\mu^i}}$. There are similar expressions for the scattered fields, for which the index and total number of functions used in the expansion are μ, μ_M, since we need not use the same number of functions for the internal and external field expansions, which we shall discuss in more detail later.

2.1.1 Surface Green Functions

The surface Green function (SGF), G, gives an exact relation between the internal and scattered fields and the incident fields, $\mathcal{F}^{\mathbf{0}}$, in terms of the surface integral [44, 45],

$$\mathcal{F} = \int_S G\mathcal{F}^{\mathbf{0}} ds, \tag{2.6}$$

where $\mathcal{F}$ represents the internal fields inside the particle and the scattered fields outside the particle. The SGF is a function solely of the particle in

question (not the incident field), and, once calculated, can be used to find the field at any point from any incident field. We show in this section how to find numerically efficient approximations of Eq.(2.6) by using the boundary conditions on **E,H** at the particle surface.

We can enforce the boundary conditions at the particle surface by matching the expansions of the fields in SVWF's so that the residual of the surface fields is minimised around the particle in a least squares sense [46]. Consider U_p, D_p, an auxiliary system of (possibly generalized) vector functions which are linearly independent and have the component orthogonal to S identically null. Using a finite subset of these functions with $p \leq N_p$ and the boundary conditions, we can define the matrix equation relating the incident fields , $\mathcal{F}^{\mathbf{0}}$, to the internal and scattered fields

$$\begin{bmatrix} < U_p|F^i_\nu > & < U_p|F^s_\mu > \\ < D_p|F^i_\nu > & < D_p|F^s_\mu > \end{bmatrix} \begin{bmatrix} c^i_\nu \\ -c^s_\mu \end{bmatrix} = \begin{bmatrix} < U_p|\mathcal{F}^{\mathbf{0}} > \\ < D_p|\mathcal{F}^{\mathbf{0}} > \end{bmatrix}, \tag{2.7}$$

where we use the notation $< a|b >= \int_S a^* \cdot b ds$ to indicate the surface integral of the scalar product of complex vector functions over the surface S. Note that we can find a least-square solution for the expansion coefficients $c^{i/s}_{\nu/\mu}$ even when the left hand side matrix in Eq. 2.7 is rectangular by calculating, through Singular Value Decomposition (SVD) [47], the Moore-Penrose pseudo-inverse, a generalised matrix inverse defined for non-square complex matrices which we will discuss in greater detail in Section 2.1.3. By solving Eq. 2.7, we can find an approximate surface Green function,

$$G^{\nu_M+\mu_M,N_p} = [F^i_\nu I_i, -F^s_\mu I_s] L^{-1}_{\nu+\mu,p} \begin{bmatrix} U_p \\ D_p \end{bmatrix}, \tag{2.8}$$

where I_i is 1 inside the particle and 0 elsewhere, I_s is 0 inside the particle and 1 elsewhere, and L^{-1} is the pseudo-inverse of the left hand side matrix in Eq.(2.7). For fixed ν_M, μ_M, the value of N_p at which one reaches conver-

gence depends on the choice of U_p, D_p. It can be shown that by increasing ν_M, μ_M and N_p, $G^{\nu_M+\mu_M,N_p}$ converges to G [48]. The algorithm requires $O(N_p^3)$ operations, but uniquely determines the fields at all points in space. Furthermore, once $G^{\nu_M+\mu_M,N_p}$ has been determined, it need not be evaluated for each individual input field, offering a computational saving over methods such as the Finite Difference Time Domain technique and DDA.

In this study we take advantage of the fact that, for axisymmetric scatterers, the azimuthal modes decouple and we can thus project on each harmonic $\exp(im\phi)$ and solve each azimuthal mode individually. We consider particles whose surface can be parametrized by the angles θ and ϕ and use generalised projection functions $|U_p>=[u_p,0]^T$, $|D_p>=[0,u_p]^T$ with

$$\begin{aligned} u_p \circ \mathcal{S} &\equiv \int \delta(\theta-\theta_p)\frac{e^{-im\phi}}{2\pi}[\hat{n}(\theta)\times\hat{\phi}(\theta,\phi)]\cdot[\hat{n}(\theta)\times\mathcal{S}(\theta,\phi)]d\theta d\phi \\ &= \frac{1}{2\pi}\int e^{-im\phi}[\hat{n}(\theta_p)\times\hat{\phi}(\theta_p,\phi)]\cdot[\hat{n}(\theta_p)\times\mathcal{S}(\theta_p,\phi)]d\phi, \end{aligned} \tag{2.9}$$

for $1 \le p \le N_p$ and

$$\begin{aligned} u_p \circ \mathcal{S} &\equiv \int \delta(\theta-\theta_p)\frac{e^{-im\phi}}{2\pi}\hat{\phi}(\theta,\phi)\cdot[\hat{n}(\theta)\times\mathcal{S}(\theta,\phi)]d\theta d\phi \\ &= \frac{1}{2\pi}\int e^{-im\phi}[\hat{n}_r(\theta_p)\mathcal{S}_\theta(\theta_p,\phi)-\hat{n}_\theta(\theta_p)\mathcal{S}_r(\theta_p,\phi)]d\phi, \end{aligned} \tag{2.10}$$

for $N_p+1 \le p \le 2N_p$. In this work we choose p as an index for points on the surface where the boundary conditions are matched. $\hat{\phi}$ is the unitary vector along ϕ in spherical polar coordinates, $\delta(\theta_p)$ is the Dirac delta at the point θ_p on the surface of the particle and $\hat{n}(\theta_p)\times\hat{\phi}(\theta_p,\phi), \hat{\phi}(\theta,\phi)$ are tangent to S and orthonormal. This choice of functions leads to a point matching system, where the matrix equations must be overdetermined, i.e. the number of points must be larger than the number of functions used in the expansion of the fields.

Now that we have described the formulation of the SGF method we must

find reliable and accurate ways of numerically calculating the SGF for various particles. The formulation requires that we invert a non-square matrix, and we will discuss practical methods of doing so in Sections. (2.1.3-2.1.6).

2.1.2 Physical Interpretation of SGF system

Much work in the area Greens functions is mathematically dense but this need not be off-putting as the underlying physical concept is very straightforward. Greens functions simply allow us to represent the fields in one area of space to the fields at different area of space. They are simply a mapping of how the known fields in one area are combined to produce the fields in some other area. In our case we know the fields at the particle surface via the boundary conditions of Maxwell's equations and wish to find the solution fields at different points in space away from this surface. Since the area in which we know our fields is a surface, the resultant Greens function mapping is referred to as a Surface Green Function. So, physically, the SGF we derive is simply a set of mathematical rules which tell us how we can combine the fields at the surface to approximate the fields at all other points in space. In other works Free Space Green Functions and Volume Green Functions are often referred to, these are simply a different variation to the SGF where the field is known not just on a surface, but in free space and within a volume.

Furthermore, the compact notation used in this work may be somewhat opaque at first glance. It is used such that bulky systems of equations need not be written out multiple times. So, for the avoidance of doubt, we show in Fig. 2.1 a more physical representation of the point matching equation matrix at the heart of our method (L in Eqn. 2.8). From Fig. 2.1 we can see that we are using two sets of projection functions ($\mathbf{D_1}$ and $\mathbf{D_2}$) to project the electric and magnetic fields at the particle surface. The fields shown in this diagram are the superpositions of the internal and scattered fields at the particle surface, since the incident field it contained on the right hand side of the system of equations. The width of the matrix depends on how many

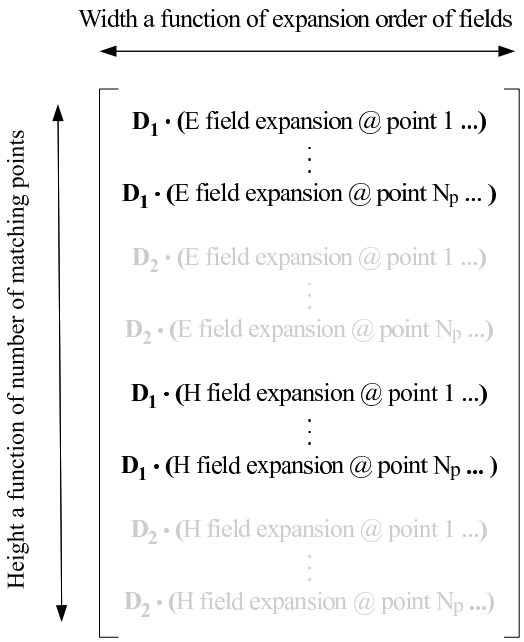

Figure 2.1: *Boundary condition matrix at the heart of the SGF approach presented in this work. N_p is the number of matching points on the surface.*

expansion functions we use in our solution while the height depends on how overdetermined our system is. We can see from this diagram that we are simply sampling the electric and magnetic fields along two directions on the surface of the particle.

2.1.3 Matrix inverses

Matrix inverses are used in many areas of mathematics, statistics and the sciences and are crucial in the solution of linear systems of equations. A brief introduction to matrix inverses is given in Appendix. D. Since in our study we aim to find the matrix inverse of a rectangular matrix, we employ the Moore-Penrose pseudoinverse as described in Appendix. D.3. The pseudoinverse can be calculated in a variety of ways using for example QR-factorization [49] and iterative methods [50]. The most popular method, however, due to its computational simplicity and accuracy is the calculation

of the pseudoinverse via Singular Value Decomposition [47], which we will introduce in the Section 2.1.4.

2.1.4 Singular Value Decomposition

The SVD is a matrix decomposition which is one of the methods which can be used to calculate the Moore-Penrose pseudoinverse. We shall examine the underlying theory of the SVD carefully as it is crucial to our solution and will become increasingly important in our analysis in Chapter. 3.

The SVD exists for any matrix $\mathbf{A}$ with entries $a_{ij} \in \mathbb{C}$ and decomposes the matrix into a product of three matrices:

$$\mathbf{A} = \mathbf{U}\mathbf{S}\mathbf{V}^H \tag{2.11}$$

where $\mathbf{U}$ is an $m \times m$ unitary matrix with entries $u_{ij} \in \mathbb{C}$, $\mathbf{V}$ is an $n \times n$ unitary matrix with entries $v_{ij} \in \mathbb{C}$ and $\mathbf{S}$ is an $m \times n$ matrix which is zero everywhere except for the main diagonal which contain entries $\sigma_i \in \mathbb{R}$ with $\sigma_i \geq 0$. The diagonal entries of $\mathbf{S}$ are usually ordered in decreasing magnitude such that $\sigma_i \leq \sigma_j$ for $j \geq i$. Thus, when using SVD on a 5×3 matrix, the structure of the matrix $\mathbf{S}$ would be:

$$\begin{bmatrix} \sigma_1 & 0 & 0 \\ 0 & \sigma_2 & 0 \\ 0 & 0 & \sigma_3 \\ 0 & 0 & 0 \\ 0 & 0 & 0 \end{bmatrix} \tag{2.12}$$

with

$$\sigma_1 \geq \sigma_2 \geq \sigma_3. \tag{2.13}$$

In this simple example $\mathbf{U}$ would be a 5×5 square matrix and $\mathbf{V}$ is a 3×3 square matrix.

2.1.5 Singular values and vectors

The diagonal elements of **S** are referred to as the singular values of **A**. For each singular value there are corresponding left and right singular vectors which are stored in the matrices **U** and **V** respectively. A singular value for which we can find two left (or right) singular vectors that are linearly independent is said to be degenerate. Non-degenerate singular values always have unique left and right singular vectors, consequently, if all singular values of **A** are non-degenerate and non-zero, then its singular value decomposition is unique.

2.1.6 Pseudoinverse via SVD

The singular value decomposition can be used for computing the pseudoinverse of a matrix. The definition of the SVD

$$\mathbf{A} = \mathbf{U}\mathbf{S}\mathbf{V}^H \tag{2.14}$$

was defined in Section. 2.1.4. We know since **U,V** are unitary and from trivial matrix properties that the pseudoinverse of the matrix is then given by:

$$\mathbf{A}^{-1} = \mathbf{V}^H\mathbf{S}^{-1}\mathbf{U}^H \tag{2.15}$$

Where we have calculated the inverses of the unitary matrices **U,V** by taking the Hermitian conjugate. The inverse of the matrix **S** is also trivially found by taking the reciprocal of the non-zero diagonal elements and transposing the matrix. It can therefore be seen that calculation of the SVD of a matrix essentially produces the pseudoinverse of the original matrix, aside from a few matrix operations.

2.1.7 Quality of results and errors

We have now laid down the basic theory for the SGF method and have studied some of the tools we use to enable us to approximate SGF's for particles. We must now ensure we have a robust measure of the error in our solutions such that we can justify the validity of our simulations. In our point matching implementation of the SGF our aim is to solve a linear system of equations which minimizes the sum of the residual field at the particle surface in a least squared sense such that:

$$|\mathbf{f}^0 - \mathbf{f}^i + \mathbf{f}^s|^2 \tag{2.16}$$

is minimal across the surface of the particle, where we have used $\mathbf{f}$ to denote the tangent components we are point matching along at the particle surface:

$$|\mathbf{f}^{0,i,s}> = |\mathbf{e}^{0,i,s}, \mathbf{h}^{0,i,s}> = |\hat{\mathbf{n}} \times \mathbf{E}^{0,i,s}, \hat{\mathbf{n}} \times \mathbf{H}^{0,i,s}> \tag{2.17}$$

where $\hat{\mathbf{n}}$ is the outward unitary normal at the particle surface. The points p at which matching occurs are usually chosen to be equally spaced around the particle generatrix. From this we can define the error at a specific point p on the surface to be

$$\delta_p = \frac{|\mathbf{f}_p^0 - \mathbf{f}_p^i + \mathbf{f}_p^s|^2}{|\mathbf{f}_p^0|^2}, \tag{2.18}$$

where $\mathbf{f}_p^{0,i,s}$ are the fields evaluated at the point p. This gives us the fractional size of the residual at the particle surface with respect to the incident field at that point. We can also study the maximum and average errors as a function of matching point position, and these are defined by:

$$\delta_{max} = max(\delta_p) \tag{2.19}$$

and

$$\delta_{av} = \frac{\sum_{p=1}^{N_p} \delta_p}{N_p} \tag{2.20}$$

We note that in similar studies, the far field results have been shown to be stable provided that the surface error $\delta_{av} \leq 10^{-3}$ [51]. This is the cutoff that we shall use in this work for the maximum error we deem acceptable.

2.2 Precursor to results

Before we progress to study the electromagnetic properties of various examples using the SGF method, we will briefly introduce some of the results we shall be studying. Some of these results are produced as standard in nearly all scattering studies, such as the scattering cross sections. Some are less common, such as the near field to the particle and the surface error variation as a function of matching point position. It is useful before continuing to review the geometry and parameters associated with of our particle in Fig. 1.7.

2.2.1 Excitation field

We can excite our particle with any incident field we wish such as a plane wave, Gaussian beam or spherical wave. However, throughout this work we will consider all particles to be illuminated by an infinitely extended plane wave, which we expand in terms of SVWF's consistent with the notation used in [52, 34]. This is the standard excitation field used in most literature and allows us to easily compare our simulations to accepted results. We shall characterize the input field by the direction of propagation with respect to the particle's symmetry axis (Ω_k). Ω_k is the angle the wavevector of the incoming plane wave makes with the symmetry (z) axis of the particle as shown in Fig. 2.2. The particle coordinate system (x,y,z) is shown in red while the input field coordinate system is shown by dashed lines. Throughout this work axial incidence is taken to mean $\Omega_k = 0°$.

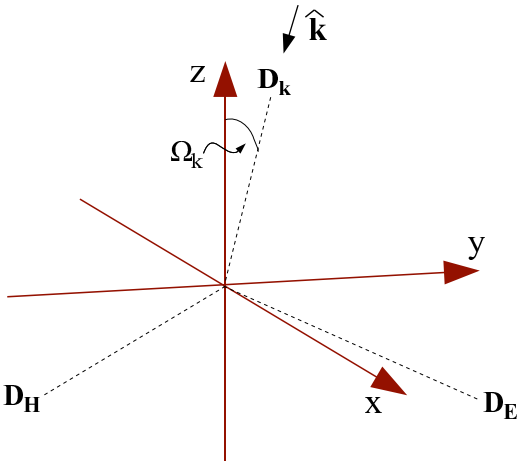

Figure 2.2: *For an input infinitely extended plane wave, the incident angle of the wavevector is specified by Ω_k, the field can be polarized in any direction by the rotation of* $\mathbf{E}, \mathbf{H}$ *about* $\hat{\mathbf{k}}$*. In this diagram the direction of polarization of* $\mathbf{E}$ *and* $\mathbf{H}$ *is shown to be* $\mathbf{D_E}$ *and* $\mathbf{D_H}$ *respectively.*

2.2.2 Particle descriptors

It is typical to label particles with characteristic dimension (i.e. largest length along one of the semi axes A,B as shown in Fig. 1.7) D by their size parameter (SP):

$$SP = \frac{2\pi D}{\lambda} \tag{2.21}$$

where $D = max(A, B)$. The aspect ratio, AR, is defined from Fig. 1.7 as:

$$AR = \frac{A}{B} \tag{2.22}$$

where A is the real dimensional length of the semi-axis along the z direction and B is the real dimensional length of the semi axis along the x direction. Note that the size parameter and aspect ratio are dimensionless. Additionally, we use the convention of calculating the aspect ratio of the particle as $AR = A/B$ (always the semi axis length along the z-axis on the numerator) such that prolate particles have $AR > 1$ and oblate particles have aspect

ratio $AR < 1$.

We generalize our study further by using adimensional units in all our calculations, such that all lengths are scaled by $2\pi/\lambda$ (the wavenumber in free space) and are thus dimensionless. We can then re-label our particle lengths with $a = 2\pi A/\lambda$ and $b = 2\pi B/\lambda$, the rescaled dimensionless sizes along z and x respectively, such that the characteristic dimension is now $d = 2\pi D/\lambda$ and the size parameter and aspect ratio are redefined as:

$$SP = d \tag{2.23}$$

and

$$AR = \frac{a}{b} \tag{2.24}$$

where all variables are adimensional. This adimensional formulation means that all solutions that we shall solve in this study are applicable to a family of scalable particles, which could be of any physical size as long as the wavelength of excitation is in the same ratio with respect to the particle size as the solution. This is of course providing that the dispersion relation [53] for the refractive index is a constant over the range we consider, which may or may not be a reasonable approximation depending on the material and range considered. We will discuss this fact in greater detail when we begin demonstrate our results for real metallic particles. We note that with this rescaling, the new dimensionless free space wavenumber is $k_s = 1$ while the internal wavenumber is simply $k_i = n_{rel}$, the relative refractive index of the particle we are considering with respect to the surrounding medium.

2.2.3 Differential scattering cross-section

The differential scattering cross-section (DSCS) is an important measure used in scattering analysis and gives the angular distribution of electric field intensity as the observation point tends to infinity [54]. The DSCS used in this work has units of area. It is also a very useful test of the convergence of scat-

tering methods as it should theoretically converge on constant distribution as we expand the scattered fields with progressively more functions.

$$\sigma_{P,S}^{s} = \lim_{r\to\infty} |e^{-ik_s r} r \mathbf{E}_{\theta,\phi}^{\mathbf{s}}|^2 \tag{2.25}$$

where the P and S polarizations refer to the θ and ϕ components in the far field respectively. It is standard practice when comparing far field results from various methods to use the **total** DSCS by adding the P and S polarizations over the range which they are evaluated:

$$\sigma_T^s = \sigma_P^s + \sigma_S^s \tag{2.26}$$

where σ_T^s is the total cross section. Throughout this study, we will take DSCS to mean the total DSCS unless otherwise stated. Due to typically large order of magnitude variations in the DSCS's as a function of angle we plot DSCS's on a logarithmic scale. When we plot the DSCS's the angular range will be over the range 'DSCS angle', such that a particle illuminated axially will have a maximum in the DSCS at a DSCS angle of 0°, i.e., the forward direction.

In order to evaluate the DSCS we make use of the asymptotic form of the SVWF's. We may denote these asymptotic forms by $M_{mn}^{\infty}, N_{mn}^{\infty}$ and are given by [55]:

$$M_{mn}^{\infty} \sim \frac{\exp ik_s r_p}{r}(-i)^{n+1}\mathbf{m}_{mn}(\theta,\phi) + 0(\frac{1}{r^2}) \tag{2.27}$$

$$N_{mn}^{\infty} \sim \frac{\exp ik_s r_p}{r}(-i)^{n}\mathbf{n}_{mn}(\theta,\phi) + 0(\frac{1}{r^2}) \tag{2.28}$$

where the functions $\mathbf{m}_{mn}$ and $\mathbf{n}_{mn}$ are the angular part of the SVWF's, i.e. the SVWF's with the Hankel functions removed. Note the radial variation is contained within an exponential multiplier which decays as $1/r$. We build the asymptotic form of the electric field in the same way as our usual field

expansions:

$$\mathbf{E}^{\infty} = \sum_{n=1}^{N_s} \sum_{m=-M}^{M} a_{mn}\mathbf{M}_{mn}^{\infty} + b_{mn}\mathbf{N}_{mn}^{\infty} \tag{2.29}$$

where a_{mn} and b_{mn} have been determined from our SGF applied to a particular incident field and N_s is the number of functions used to expand the scattered field, i.e. the number of functions contained within the multi-index μ_M in Section. 2.1.1.

2.2.4 Near field plots

There has been a significant increase in interest recently in the study of the near field properties of nanoparticles. One of the main advantages of our SGF formulation is that we are able to find the fields at any point in space, whether internal or external to the particle. We plot near field electric field intensity plots in order to view the distribution of energy in and around particles. We use colour plots to picture the near field plots, and a typical example along with the colour scale is shown in Fig 2.3. It should be noted that these colour plots are on a linear scale and each image has maximum numerical value of the brightest point set equal to unity when the colour map is applied.

2.2.5 Error plots

For particles we study we will show the corresponding error plot as function of position on the particle surface, as well as the maximum and average errors. This enables us to gain an overall impression of how accurate the solution is for a particular particle, as well as showing how the error varies across the surface. This could be of relevance to applications which involving multiple particles in contact with each other. In such cases we may wish to drive down the error at the point of contact, for instance at the pole of the particle.

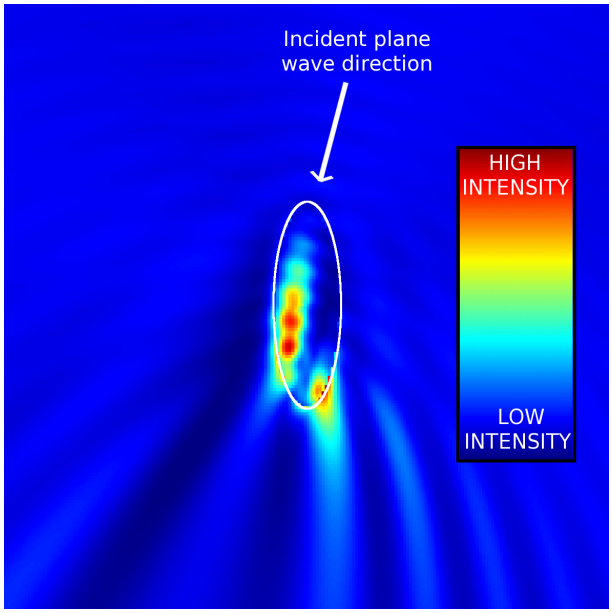

Figure 2.3: *An example of a near field plot slice through the $x-z$ plane showing the colour key that will be used in this work.*

2.2.6 Convergence plots

We will also study how various measures converge as we change a solution parameter. For instance, we may study how the error varies as we increase the number of functions we use in the solution of our problem.

One of the standard tests for far field results to ensure convergence is to monitor how the cross section varies when more functions are used in the solution of the problem. Typically, convergence is said to be attained when a certain percentage of the DSCS elements remain within some tolerance of each other when the problem is solved for two consecutive numbers of functions. So a single point on the DSCS plot is said to be convergent if:

$$(1-\delta_{DSCS})DSCS_p^i \leq DSCS_p^{i+1} \leq (1+\delta_{DSCS})DSCS_p^i \tag{2.30}$$

where $DSCS_p^{i+1}$ is the DSCS at an angle indexed by point p evaluated for $i+1$ functions, $DSCS_p^i$ is the same DSCS element evaluated for one less

function and δ_{DSCS} is a variable parameter which controls how closely the points must match in order to be said to be convergent. The entire DSCS is then said to be convergent if a certain fraction of all the points on the scattering cross section fulfill this criteria. Thus, if the number of points convergent across the DSCS is is N_{conv} and the total number of angles for which the DSCS is evaluated is N_{DSCS} then the cross section is said to be convergent if:

$$\frac{N_{conv}}{N_{DSCS}} \geq \Delta_{DSCS} \tag{2.31}$$

Where Δ_{DSCS} is our DSCS convergence fraction. Typical tolerances that are used in literature are $\delta_{DSCS} = 0.05$ and $\Delta_{DSCS} = 0.8$ [55], i.e. cross sections are said to converge if 80% of the points on the DSCS are within 5% of their previous value when the problem is solved for one less function. This standard convention will be used in this work.

2.3 Simulations for spherical particles

We shall now study the results of our simulations for spherical particles, and we will study both dielectric and real metallic particles. As previously discussed, there are very few analytical solutions in computational electromagnetics, however, for spheres there is an analytical solution, namely Mie theory. By implementing widely available routines for Mie theory [56], we can compare the far field results calculated via SGF's to exact solutions. The functions we use for the solution of spherical particles are the SVWF's, defined at the origin of the particle as shown in Fig. 2.4.

2.3.1 Dielectric spheres

We will begin by studying some examples of dielectric spheres. Such nanoparticles have been of increasing interest in recent years due to applications such as photonic nanojets. In our first example, we will consider a spherical

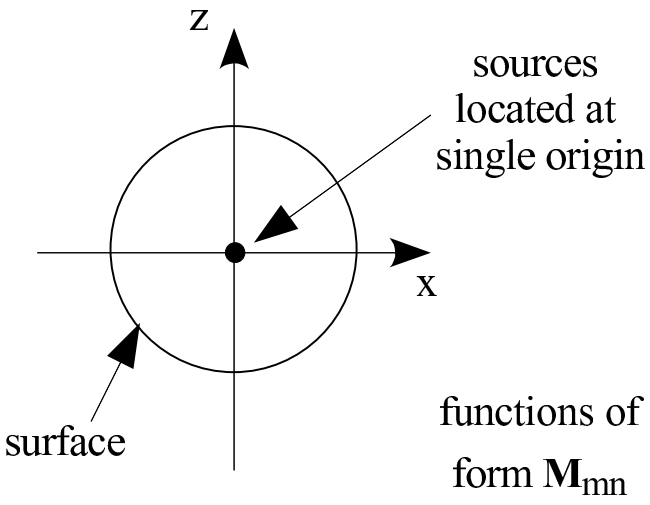

Figure 2.4: *A spherical particle with SVWF sources defined at the origin of coordinates.*

nanoparticle with refractive index $n = 1.50$ and $SP = 10$, typical values that can be produced practically [13]. In Fig. 2.5 we study the average error in our solution as a function of the number of functions used in the calculation of the SGF, for a particle illuminated axially. We can see that the error

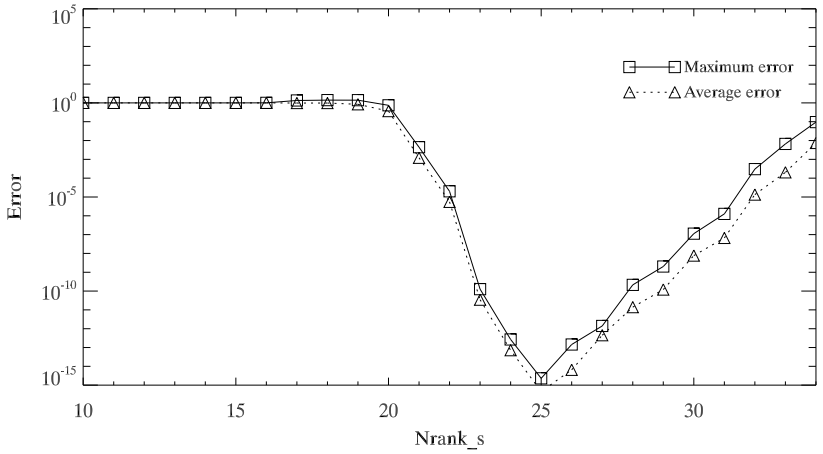

Figure 2.5: *Variation of δ_{av} and δ_{max} for a dielectric particle with SP=10, AR=1, n=1.5 illuminated axially for increasing numbers of solution functions.*

varies strongly as a function of the number of functions used in the expansion. By selecting the appropriate number of solution functions ($N_s = 25$ in this case) we see that errors of the order $\delta_{av} = 10^{-16}$ are obtainable. As we increase the number of functions beyond this value, the solution becomes more unstable and eventually becomes unusable. Such behavior is common for methods based on sources defined from the origin of coordinates, such as the non distributed source formulation of the EBCM, which can have narrow ranges of solution convergence.

We can also study the convergence of the scattering cross section which is shown in Fig. 2.6 , where we use the standard definition of convergence used in section 2.2.6. We see that the DSCS converges (80% of points converge

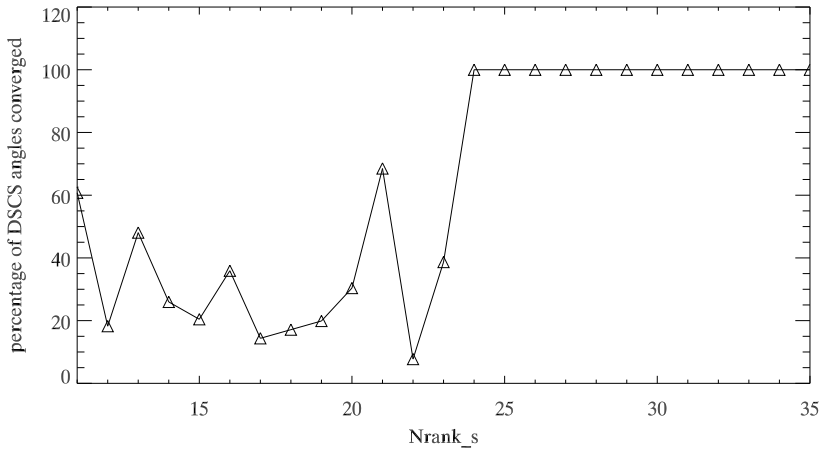

Figure 2.6: *Convergence of the DSCS for a dielectric particle with SP=10, AR=1, n=1.5 illuminated axially for increasing numbers of solution functions.*

within 5% of their previous value) at $N_s = 24$, ultimately progressing to total convergence at $N_s = 25$ where it remains converged over the range considered. If we then select the solution with the number of sources at which we obtain the lowest error result we can study how the error varies over the surface of the particle, which we show in Fig. 2.7. The surface error (δ_p) at the surface varies by almost three orders of magnitude and is maximal at the poles and

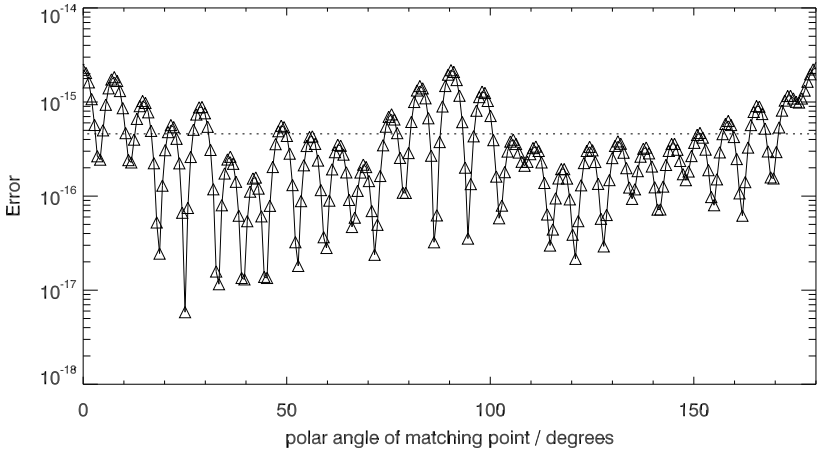

Figure 2.7: *Variation in δ_p as a function of matching point on the particle surface for a dielectric particle with SP=10, AR=1, n=1.5 illuminated axially for $N_s = 25$ functions, showing $\delta_{av} = 4.477 \times 10^{-16}$.*

equator of the sphere. These results satisfy our requirements of a convergent DSCS with average error less than $\delta_{av} = 10^{-3}$ as outlined in 2.1.7. We are therefore confident in the quality of our solution and proceed to calculate the scattering properties in both the near and far field. We show the near field and DSCS in Fig. 2.8 and note the exceptional agreement with Mie theory for the DSCS. We can see the formation of a strong intensity spot on the shadow side of the particle which is close to a photonic nanojet, although we shall study the formation of jets in more detail in the next section.

Nanojets

We may carry out a systematic calculation of the near field properties of families of various sizes of dielectric spheres. By examining these results, we are able to find particles which exhibit photonic nanojets and study the jet properties. We saw in our example Fig. 2.8 that we had what appeared to be the beginnings of a jet like structure. By increasing the size parameter of the sphere in question we find that at $SP = 16.2$ we find a very strong

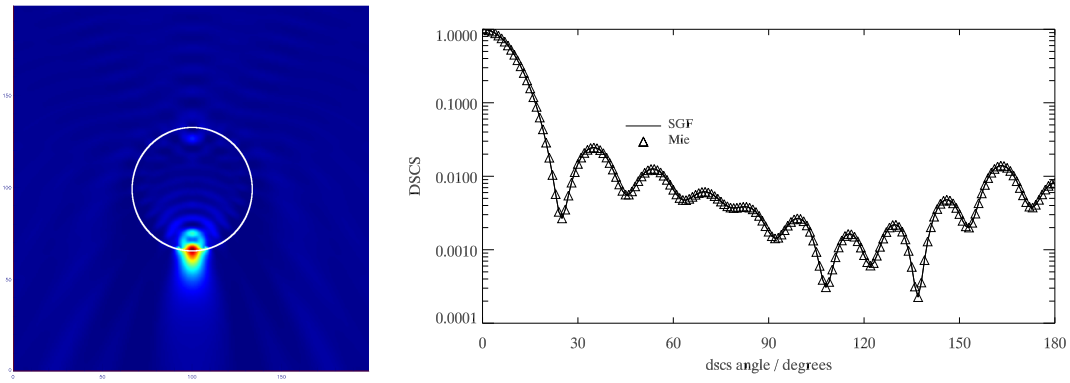

Figure 2.8: *Near field and DSCS for a dielectric particle with SP=10, AR=1, n=1.5 illuminated axially for* $N_s = 25$ *functions. We overplot the results of Mie theory in the DSCS for comparison and see that the agreement between results is excellent.*

photonic nanojet as shown in 2.9. This nanojet is typical of results found in

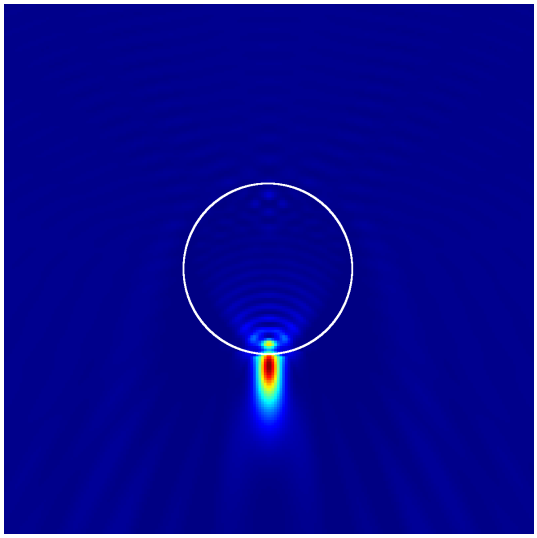

Figure 2.9: *A dielectric sphere with* $n = 1.5$*,* $SP = 16.2$ *and* $AR = 1$*, under axial incidence from a plane wave showing a photonic nanojet on the shadow side of the particle. The jet extends for several wavelengths and has a Full Width at Half Maximum (FWHM) of* 0.62λ*.*

literature, with a full width at half maximum less than the wavelength which extends outwards from the particle for several wavelengths.

2.3.2 Metallic spheres

As previously discussed, the optical properties of metallic nanoparticles makes them one of the most interesting areas in nano-science, and such materials possess complex refractive indices. With these complex refractive indices, the arguments of the spherical Bessel and Hankel functions used in the computation of the SGF also become complex. The complex nature of the arguments causes the functions to oscillate extremely rapidly, which in general makes the modelling of such particles more difficult than for dielectric particles. This has in fact been a widely known problem in computational electromagnetics for many years, and intuitively it is understandable that the modelling of a real metal is more difficult than a dielectric particle, due to the more rapidly oscillating fields. Accordingly, the range of the size parameter of the spheres which are able to be accurately modeled via the SGF method is smaller for metallic particles than for dielectrics. We shall see throughout this work, however, that we are still able to accurately model metallic particles over a a wide range.

Refractive index of metallic particles

Very careful consideration must be taken when selecting the refractive index of the metallic particles we consider. Obviously, in general all materials possess a frequency dependent refractive index, that is, they exhibit dispersion. However, for metallic particles the refractive index is strongly frequency dependent (much more so than for dielectrics) and so for the avoidance of ambiguity we must select a material and frequency of incident excitation. Due to its wide range of potential applications, we choose gold as our standard metallic material and the refractive index to be that of gold in the range $\lambda \approx 600 - 700nm$, which is $n \approx 0.32 + 3.18i$ [57].

2.3.3 Results for metallic spheres

We examine gold particles in much the same way as we did for dielectric particles. First we ensure that we have convergent solutions with respect to our surface errors and scattering cross sections, and then we study the near and far field properties of the particles. The variation in the average surface error as a function of the number of expansion functions is shown in Fig. 2.10. We can again see that the error varies strongly as a function of the number

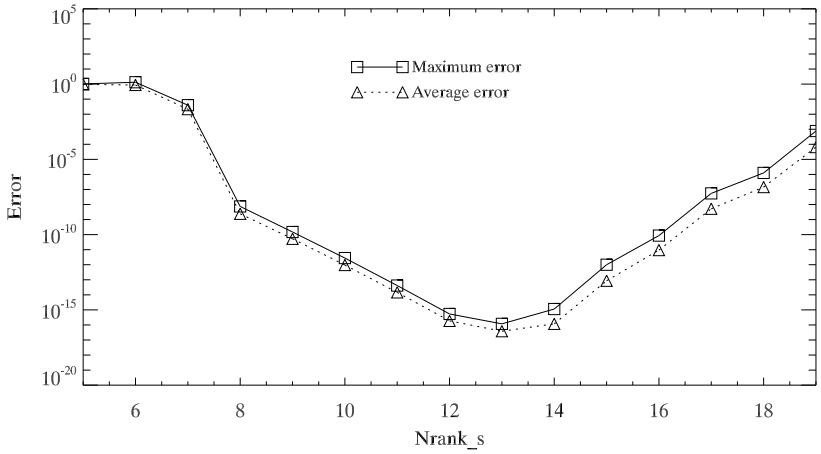

Figure 2.10: *Variation of δ_{av} and δ_{max} for a metallic sphere with $n \approx 0.32 + 3.18i$, $SP = 3$ and $AR = 1$ illuminated axially for increasing numbers of solution functions.*

of functions used in the expansion and by selecting the appropriate number of solution functions ($N_s = 13$), we obtain errors in the range $\delta_{av} = 10^{-16}$. The convergence of the scattering cross section is shown in Fig. 2.11. We see that the DSCS converges for a lower number of solution functions than for the larger dielectric particle we considered in Section. 2.3.1, as we would expect due to the smaller size relative to the excitation wavelength. We also observe strongly convergent behavior in the DSCS. If we then study the solution with the number of sources at which we obtain the lowest value of δ_{av} we can view how the error varies over the surface of the particle, which we

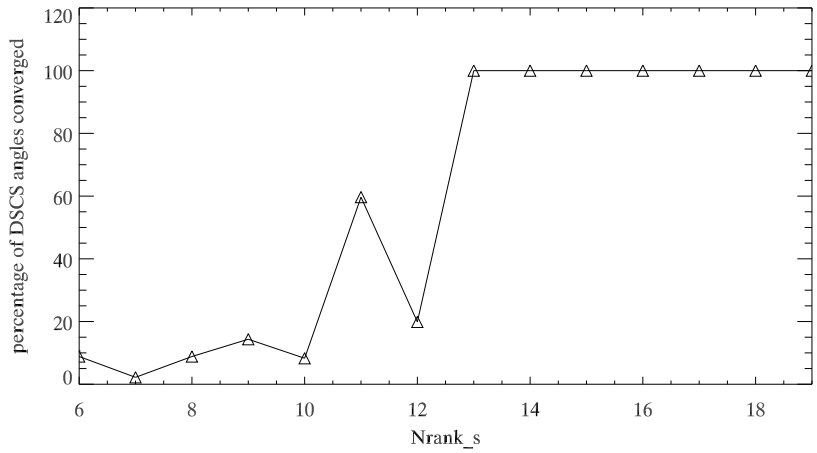

Figure 2.11: *Convergence of the DSCS for a gold particle with* $n \approx 0.32 + 3.18i$*,* $SP = 3$ *and* $AR = 1$ *illuminated axially for increasing numbers of solution functions.*

show in Fig. 2.12. The average surface error at the surface varies by around

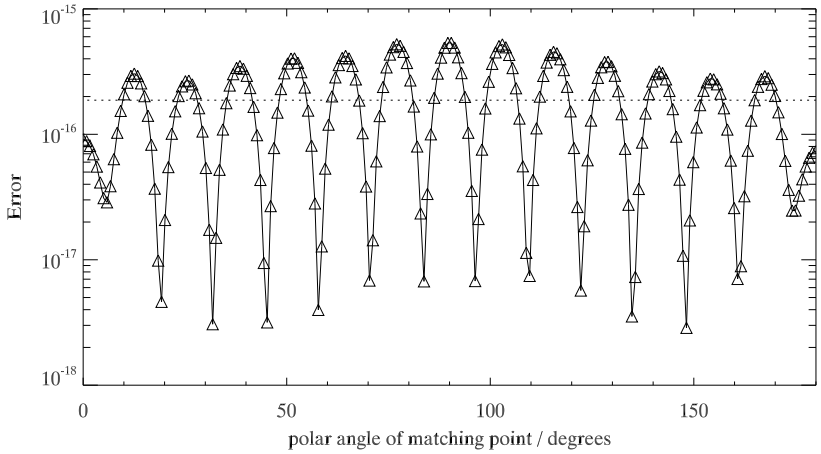

Figure 2.12: *Variation in* δ_p *as a function of matching point on the particle surface for a gold particle with* $n \approx 0.32 + 3.18i$*,* $SP = 3$ *and* $AR = 1$ *illuminated axially for* $N_s = 13$ *functions showing* $\delta_{av} = 1.942 \times 10^{-16}$*.*

two orders of magnitude and is maximal at the equator of the sphere. These results satisfy our requirements of a convergent DSCS with average error less

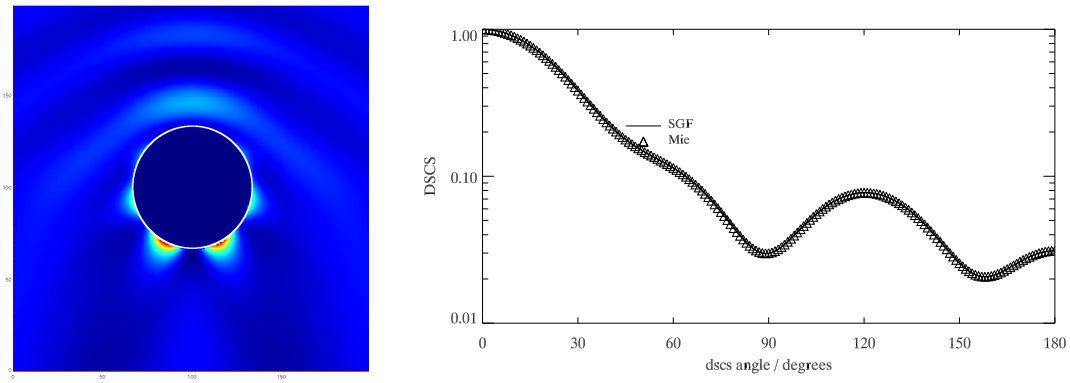

Figure 2.13: *Near field and DSCS for a gold particle with* $n \approx 0.32 + 3.18i$*,* $SP = 3$ *and* $AR = 1$ *illuminated axially for* $N_s = 13$ *functions. We overplot the results of Mie theory in the DSCS for comparison and see that the agreement between results is excellent.*

than $\delta_{av} = 10^{-3}$ as outlined in 2.1.7. We are confident in the quality of our solution and proceed to calculate the scattering properties in both the near and far field. We show the near field and DSCS in Fig. 2.13 and note the exceptional agreement with Mie theory for the DSCS. Obviously, metals are opaque in the visible region and as a result the internal field is present only within a very small skin depth. We note, however, the presence of strong hot spots on the surface of the sphere. These are common features of metallic particles we will see throughout our study.

2.4 Elongated particles

We now turn to consider the properties of elongated (prolate) particles. It is important to have clearly in mind the geometry we are studying since the terms prolate and oblate are often confused. For prolate particles, it is often helpful to think of the particles as being elongated or stretched, resembling a grain of rice as shown in Fig. 2.14. This geometry has very different scattering properties to oblate particles which we will consider in Section. 2.5.

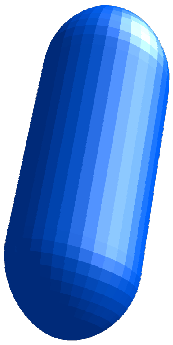

Figure 2.14: *Geometry of an elongated (prolate) rounded top cylinder.*

2.4.1 Limitations of the SVWF's for non-spherical particles; Localized and Distributed sources

If we apply the SGF method we used for spheres in Section. 2.3.1 to elongated particles, we find that although the problem can be solved to a high quality for particles with low aspect ratio, the errors associated with larger aspect ratio particles rapidly increase making such solutions unusable. This is illustrated in Fig. 2.15. We can see that the error rapidly increases as a function of aspect ratio, the same is true if the particle is flattened to a disk shape also. The error increases as the problem is poorly posed. As the aspect ratio increases, the distance from the origin to the matching points on the surface varies over a wide range and as a result the matrix elements corresponding to these points can vary by orders of magnitude. The pseudo-inversion of such a matrix is difficult, and the matrix and corresponding system of equations is said to be ill-conditioned. Obviously, this is much less of a problem for spheres as the distance from the origin to each of the matching points is a constant.

Since we know that the reason our matrix becomes difficult to invert is due to these large variations in matrix elements, we can aim to try to alter our SGF method such that we minimize the ill conditioning of the

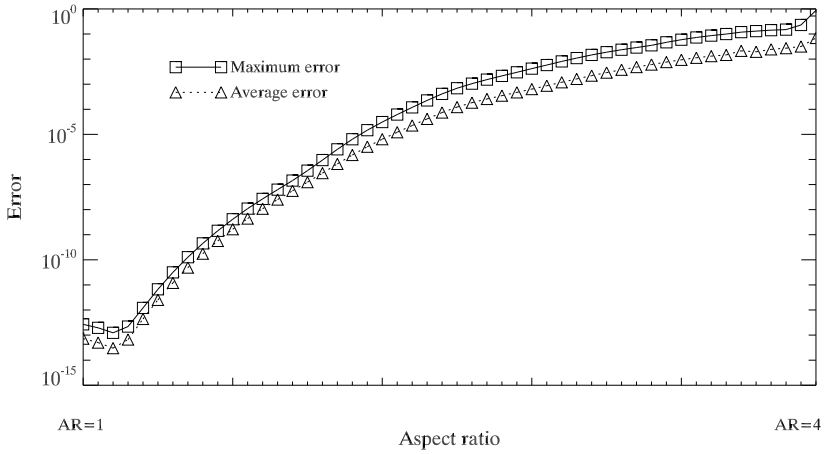

Figure 2.15: *δ_{av} and δ_{max} as a function of aspect ratio for a dielectric particle with $n = 1.5$ and $SP = 10$ showing a marked increase in surface errors as the particle becomes more elongated.*

matrix which produces the SGF. One of the most successful techniques aimed at improving the conditioning of problems involving elongated particles is the use of distributed sources [58]. Instead of having our usual system of SVWF's which are defined from one origin of coordinates, we can instead use a spatially distributed set of functions which are defined on multiple origins as illustrated in Fig. 2.16. The distributed functions we choose to use are the lowest order SVWF's for a particular azimuthal mode m, and are distributed along the axis of symmetry of the particle. Using the symmetry axis ensures that surface integrals over such functions reduce to line integrals as in Section. 2.1.1. The third index q in Fig. 2.16 allows us to index the spatially distributed sources. The term $max(1, |m|)$ is present to ensure that the index $n \neq 0$ since the SVWF's are zero for this case and $n \geq m$, i.e. to ensure that the angular quantum number is high enough to produce the azimuthal quantum number of the specific mode we are studying. Physically, we use **lowest order** functions so that the functions at the surface are as regular as possible to help improve the conditioning of the matrix since lower order functions vary less rapidly. Also, we **distribute** the functions

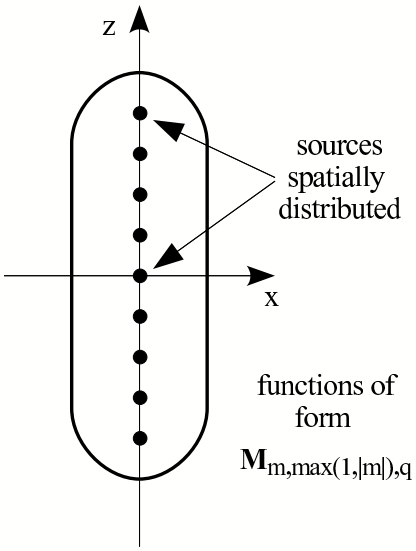

Figure 2.16: *The spatial distribution of SVWF sources along the symmetry axis of an elongated particle.*

such that each point on the particle surface has a source close to it, this ensures that we no longer deal with matrix elements which vary over many orders of magnitude. Of course, we still have the same requirements on our functions that was discussed in Section. 2.1, namely that the functions we use are complete, linearly independent solutions of the Maxwell equations. It is possible to show that the distributed lowest order SVWF's do indeed satisfy these criteria [55]. We will henceforth refer to the distributed lowest order SVWF's as distributed sources. Correspondingly, we shall refer to the functions defined at a single origin as localized sources. In order to distinguish the localized and distributed sources, we will label the distributed sources as $\tilde{\mathbf{M}}_{m,q}$ (with a tilde) where we have contracted the first two indices to a single index m (they are both functions of only m) and the second index q is the index of the position of the source.

2.4.2 Formulation of the SGF method with distributed sources.

Since our distributed sources satisfy all the criteria we require to be used in our electromagnetic problem, we can use the results of section Section. 2.1.1 directly and define our SGF in exactly the same way, the only difference is that the internal and scattered fields are now expanded as sums over distributed sources:

$$\mathbf{E}^{i,s} = \sum_{q=1}^{N_{i,s}} \sum_{m=-M}^{M} a_{mn}^{i,s} \tilde{\mathbf{M}}_{m,q}^{1.3} + b_{mn}^{i,s} \tilde{\mathbf{N}}_{m,q}^{1.3} \tag{2.32}$$

Where there are also corresponding terms for the magnetic fields.

2.4.3 Asymptotic form of distributed SVWF's

We saw in Section. 2.2.3 that the localised SVWF sources had corresponding asymptotic representations which we used in the calculation of the far field properties of particles. In order to find the far field properties of particles modeled with SVWF sources, we need to find the asymptotic form of these functions also. Consider the geometry illustrated in Figure. 2.17. Obviously,

$$r = a + b = L\cos(\theta) + r'\cos(\alpha). \tag{2.33}$$

However, as the point P moves further from particle, $r \to \infty$ and $\alpha \to 0$, therefore it can be shown that

$$r' \to r - L\cos(\theta) \tag{2.34}$$

and

$$\theta' \to \theta \tag{2.35}$$

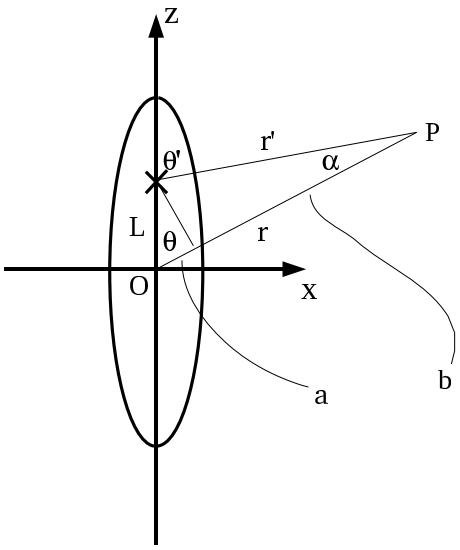

Figure 2.17: *Geometry of distributed SVWF sources. Consider a source point denoted by a cross located a distance L along the axis from the particle coordinate origin O. The angle of an observation point P is given by θ, θ' for the global and source origins respectively and, similarly, the distance to P is given by r, r'. The angle between r and r' is α and the distance r can be subdivided into a and b which are separated by the normal to r which passes through the source.*

and also obviously

$$\phi' = \phi. \tag{2.36}$$

From these relations we can define the asymptotic form of the distributed functions as a modification to Eqns. 2.28, where each individual source on the symmetry axis is deposited some distance L_q from the global origin:

$$\tilde{\mathbf{M}}^{\infty}_{mq} \sim \exp\left(-ik_s L_q \cos\theta\right) \frac{\exp ik_s r}{r} (-i)^{n'+1} \mathbf{m}(\theta,\phi)_{m,n'} + 0(\frac{1}{r^2}) \tag{2.37}$$

$$\tilde{\mathbf{N}}^{\infty}_{mq} \sim \exp\left(-ik_s L_q \cos\theta\right) \frac{\exp ik_s r}{r} (-i)^{n'} \mathbf{n}(\theta,\phi)_{m,n'} + 0(\frac{1}{r^2}) \tag{2.38}$$

with $n' = \max(1, |m|)$ and $\mathbf{m}(\theta,\phi)_{m,n'}$, $\mathbf{n}(\theta,\phi)_{m,n'}$ the vector spherical harmonics. Thus we have expressed the asymptotic form of the distributed spherical wavefunctions as an exponential term which is a function of the source position multiplied by a corresponding spherical harmonic. This al-

lows us to readily compute the scattering cross sections for elongated particles calculated via distributed sources.

2.4.4 Elongated particle results

We shall now progress to study the optical properties of elongated nanoparticles using the SGF via distributed sources. We should note that there are no analytical solutions for the general problem of elongated axisymmetric particles and so we do not have exact solutions to compare our results against. Instead, we will compare our far field results to the results of Doicu et. al. [55] (where available, these solutions do not apply to metallic particles) who implement the Extended Boundary Condition Method (EBCM) as discussed in Section. 1.5.4.

2.4.5 Elongated dielectric particles

We will begin our analysis of the electromagnetic properties of elongated particles by studying an illustrative example of a dielectric rounded top cylinder. We choose our rounded cylinder to have $n = 1.50$, $SP = 13$ and $AR = 4.33$. First, in Fig. 2.18, we check the behavior of the surface errors as a function of the number of solution functions. We can see form Fig. 2.18 that the error varies as a function of the number of functions used in the expansion. We see that the behavior in the error is different to that which was observed for spheres, the error decreases steadily and is still decreasing at the end of the range considered. For larger numbers of sources the error decreases by a small amount, but there is significant additional computational expenditure for little error reduction. By selecting the largest number of functions considered ($N_s = 50$ in this case) we see that errors of the order $\delta_{av} = 10^{-5}$ are obtainable. At first glance this seems larger than the errors for spheres, but errors in this range are typical for nonspherical particles, however the average error is still below our cutoff of $\delta_{av} = 10^{-3}$. In Chapter. 3 we will

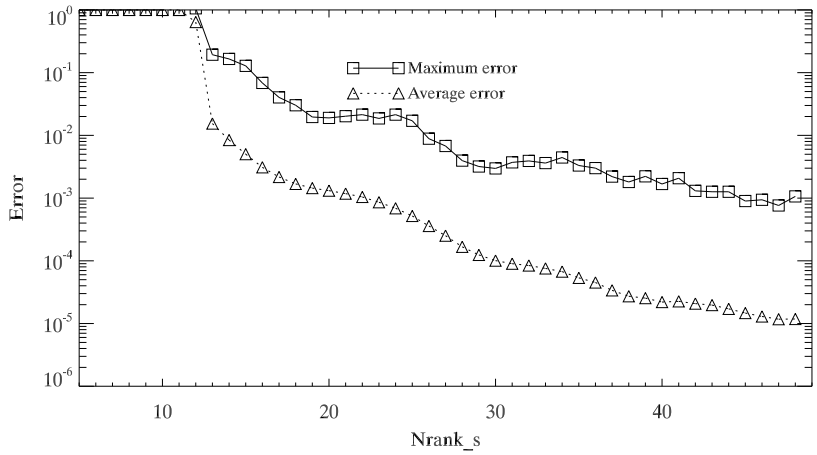

Figure 2.18: *Variation of δ_{av} and δ_{max} surface errors for a dielectric particle with $n = 1.50$, $SP = 13$ and $AR = 4.33$ illuminated axially for increasing numbers of solution functions.*

study ways of optimizing our solutions in order to decrease the error, but for the time being our errors are sufficiently low for us to be able to accurately model the near and far field properties of a wide range of particles. The convergence behavior of the DSCS is shown in Fig. 2.19. We note that by the standard definition of convergence, we would deem the DSCS to be converged at $N_s = 10$ functions, where the surface error is still appreciable. With more solution functions, there is a dip in the percentage conversion before the graph rises to 100% where it remains converged over a wide range. Careful attention must be paid to such convergence behavior since the DSCS may seem to converge but the large error indicates a poor quality of the solution. In fact, the shape of the DSCS curve at the first point where it first becomes "converged" often bears no appreciable similarity to the correct curve found with a higher number of solution functions and lower error. These "false convergencies" are common in the particles we shall study, and highlight a major flaw in using the convergence criteria of the DSCS as the sole measure of convergence in our solution. This is one of the main reasons we also study the error conversion plots, and we are confident in our solutions

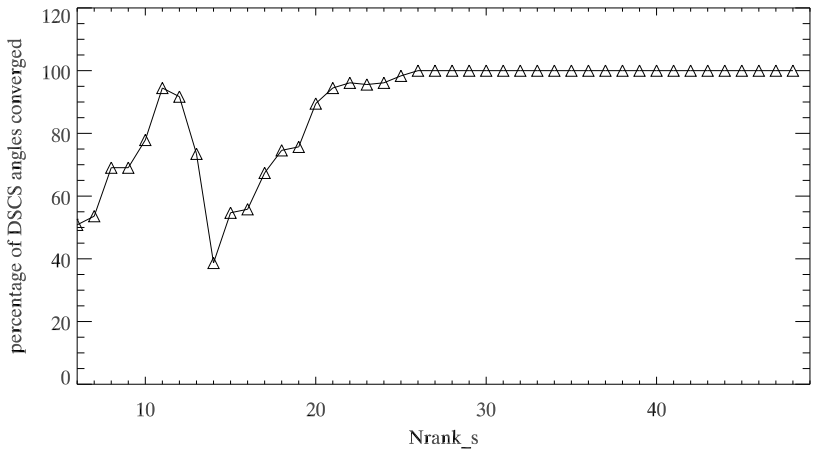

Figure 2.19: *Convergence of the DSCS for a dielectric particle with* $n = 1.50$*,* $SP = 13$ *and* $AR = 4.33$ *illuminated axially for increasing numbers of solution functions.*

only when we have a converged far field **and** low average error. If we then select the solution with the largest number of sources (and lowest error) and plot the surface error variation we obtain Fig. 2.20. The error at the surface

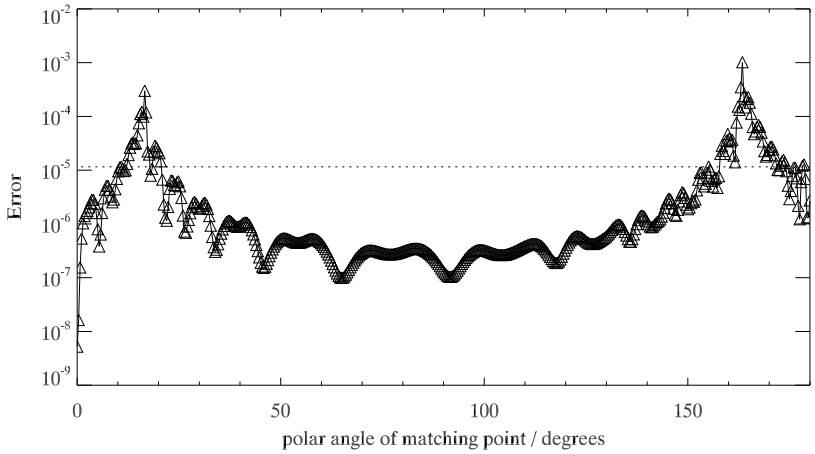

Figure 2.20: *Variation in* δ_p *as a function of matching point on the particle surface for a dielectric particle with* $n = 1.50$*,* $SP = 13$ *and* $AR = 4.33$ *illuminated axially for* $N_s = 50$ *functions* $\delta_{av} = 1.214 \times 10^{-5}$*.*

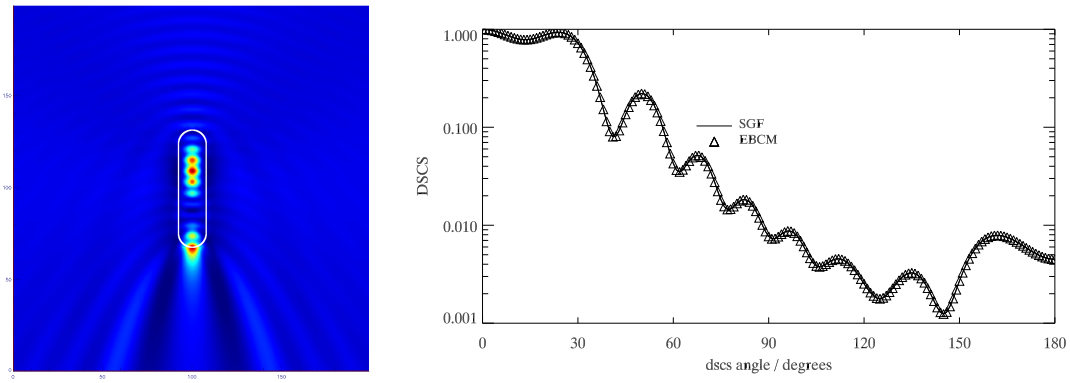

Figure 2.21: *Near field and DSCS for a dielectric particle with* $n = 1.50$*,* $SP = 13$ *and* $AR = 4.33$ *calculated for* $N_s = 50$ *functions. We overplot the results of the EBCM in the DSCS for comparison and see that the agreement between results is excellent.*

varies by a larger range than for spheres, varying by around five orders of magnitude. It can be seen that the error at the top pole of the particle is extremely small and there are two distinct peaks in the error where it climbs towards $\delta_p = 10^{-3}$. These peaks coincide with the location of the discontinuity in the derivative of the surface curvature, since we are modelling a particle formed by joining a cylinder with two hemispherical tops. However, we are satisfied that average error in our solution is low enough to provide convergence we proceed to calculate the scattering properties in both the near and far field which we show in Fig. 2.21. We note from Fig. 2.21 that there are strong intensity spots within the particle and, again, the formation of a jet like structure on the shadow side of the particle.

Results for $\Omega_k \neq 0$

We note that the plots shown in Figs.(2.18-2.21) are all for a single input wave which is axially incident. Additionally, in section 2.3.1 we did not study the properties of spheres for non axial incidence since the solution fields are simply rotated by the same angle at which the input field is rotated. However,

for non spherical particles this symmetry disappears and we cannot obtain the scattering properties at different incident angles by the simple rotation of the solution fields of the same particle illuminated at axial incidence. We thus have to calculate the electromagnetic properties for each incident field individually. This means that for each input field for the same particle, we have individual convergence and surface error variations. We will refrain from showing all of these convergence and error plots for each particle and incident field we study, we do however observe exactly the same type of behavior in these plots as for axial incidence. For non axial incidence, we will simply show the near and far fields and state the average surface error, in this way we can be clearly quantify the quality of our solutions. We will therefore study the near and far fields for this particle as a function of input beam angle. If we illuminate the particle at angles $\Omega_k = 30°, 60°, 90°$ and solve for an appropriate number of azimuthal modes (usually between $M = 3$ to $M = 6$; in this case $M = 3$), we produce the near and far field results shown in Figure. 2.22. We can see that the intensity distribution is very sensitive to the input beam angle. For the axially incident case, the majority of the intensity is located within the particle whereas at $\Omega_k = 90°$ we see that almost all of the intensity is located outside the particle. As with the spheres studied in Section. 2.3.1, most of the intensity is located in the forward direction, which is reflected in the scattering cross sections also. We shall study the effect of size, shape and material on near field energy distribution in more detail in Chapter. 3 where we shall make some qualitative arguments to justify what is observed in our simulations. For the cross sections, we can see that the position of the maximum rotates as the input beam angle is varied, as expected. We can also see that the far field results are in excellent agreement with those calculated with the EBCM.

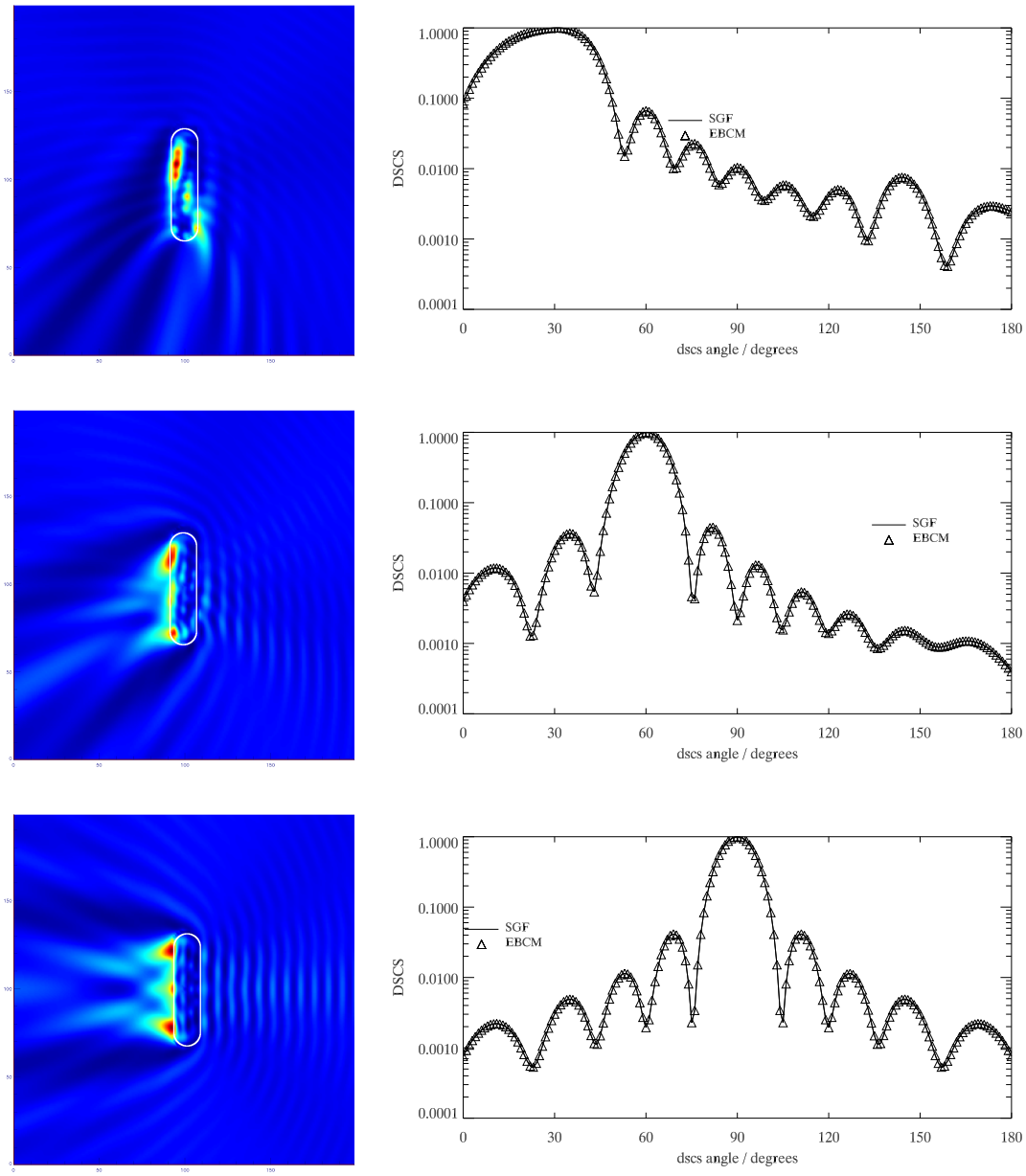

Figure 2.22: *Near fields and DSCS's for a dielectric particle with SP=13, AR=4.33, n=1.5 illuminated at* $\Omega_k = 30°, 60°, 90°$ *(from top to bottom). The corresponding errors are* $\delta_{av} = 1.332 \times 10^{-5}$, $\delta_{av} = 3.904 \times 10^{-5}$ *and* $\delta_{av} = 2.360 \times 10^{-5}$, *respectively.*

2.4.6 Elongated metallic particles

We may also use the SGF method with distributed sources to study materials with a complex refractive index. We shall study a gold particle with $n \approx 0.32 + 3.18i$, $SP = 4$ and $AR = 2$ and in the same way as was previously discussed we may view the convergence of the average surface error and scattering cross section in Figs.(2.23-2.24) respectively. Again, we see in

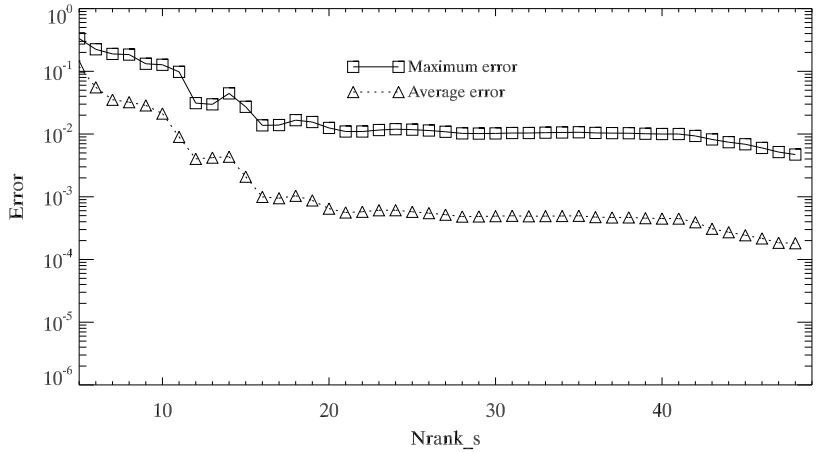

Figure 2.23: *Variation of δ_{av} and δ_{max} surface errors for a gold particle with $n \approx 0.32 + 3.18i$, $SP = 4$ and $AR = 2$ illuminated axially for increasing numbers of solution functions.*

Fig. 2.23 that the error decreases to around $\delta_{av} = 10^{-4}$ where it appears to vary by a small amount, although the smallest error is for the largest number of functions used in the expansion. In Fig. 2.24 we see that the DSCS converges rapidly for this particle, after displaying false convergence for a lower number of functions. The lowest error solution is obtained at $N_s = 50$ and we study how the error varies over the surface of the particle in Fig. 2.25. The error at the surface varies by around five orders of magnitude and is maximal at the poles where the error is large, but the low average error makes us confident in the quality of our solution and we proceed to calculate the scattering properties in both the near and far field in Fig. 2.26.

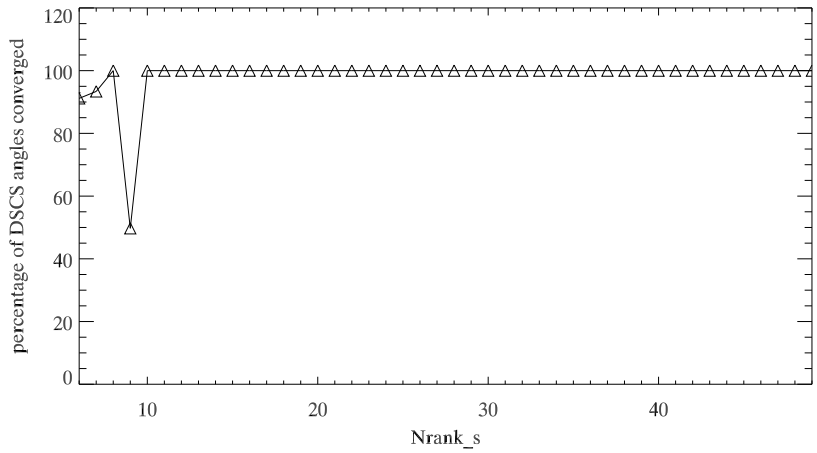

Figure 2.24: *Convergence of the DSCS for a gold particle with* $n \approx 0.32 + 3.18i$*,* $SP = 4$ *and* $AR = 2$ *illuminated axially for increasing numbers of solution functions.*

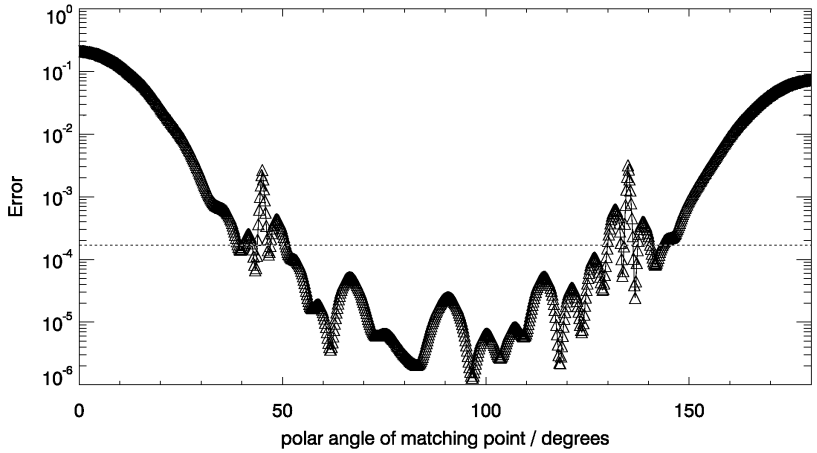

Figure 2.25: *Variation in* δ_p *as a function of matching point on the particle surface for a gold particle with* $n \approx 0.32 + 3.18i$*,* $SP = 4$ *and* $AR = 2$ *illuminated axially for* $N_s = 50$ *functions showing* $\delta_{av} = 1.822 \times 10^{-4}$*.*

Results for non axial incidence

We can study the near and far field variation as a function of input beam angle for this metallic particle, which is shown in Fig. 2.27. We note that

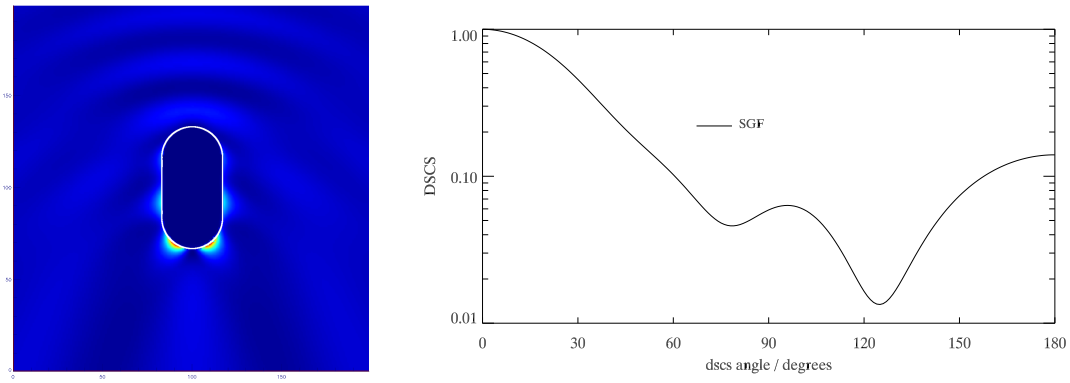

Figure 2.26: *Near field and DSCS for a gold particle with* $n \approx 0.32 + 3.18i$*,* $SP = 4$ *and* $AR = 2$ *calculated for* $N_s = 50$ *expansion functions.*

the surface hot spots change position as the beam rotates and, of course, the internal field is almost zero throughout due to the small skin depth.

2.5 Flat particles

We now turn to study the electromagnetic properties of flat (oblate) particles. Again, it is important to have clearly in mind the geometry we are studying. For oblate particles, it is often helpful to think of the particles as being flat or squashed, resembling a pancake as shown in Fig. 2.28.

2.5.1 Modifications to distributed sources; imaginary sources

We saw in Section. 2.4.4 that the conditioning of our matrices could be greatly improved by using distributed sources which were distributed on the symmetry axis of the particle, such that all points on the particle surface had a source within close proximity. By doing so we found that we could accurately model much more elongated particles than with conventional localised sources. However, for flat particles the major axis does not coincide with the

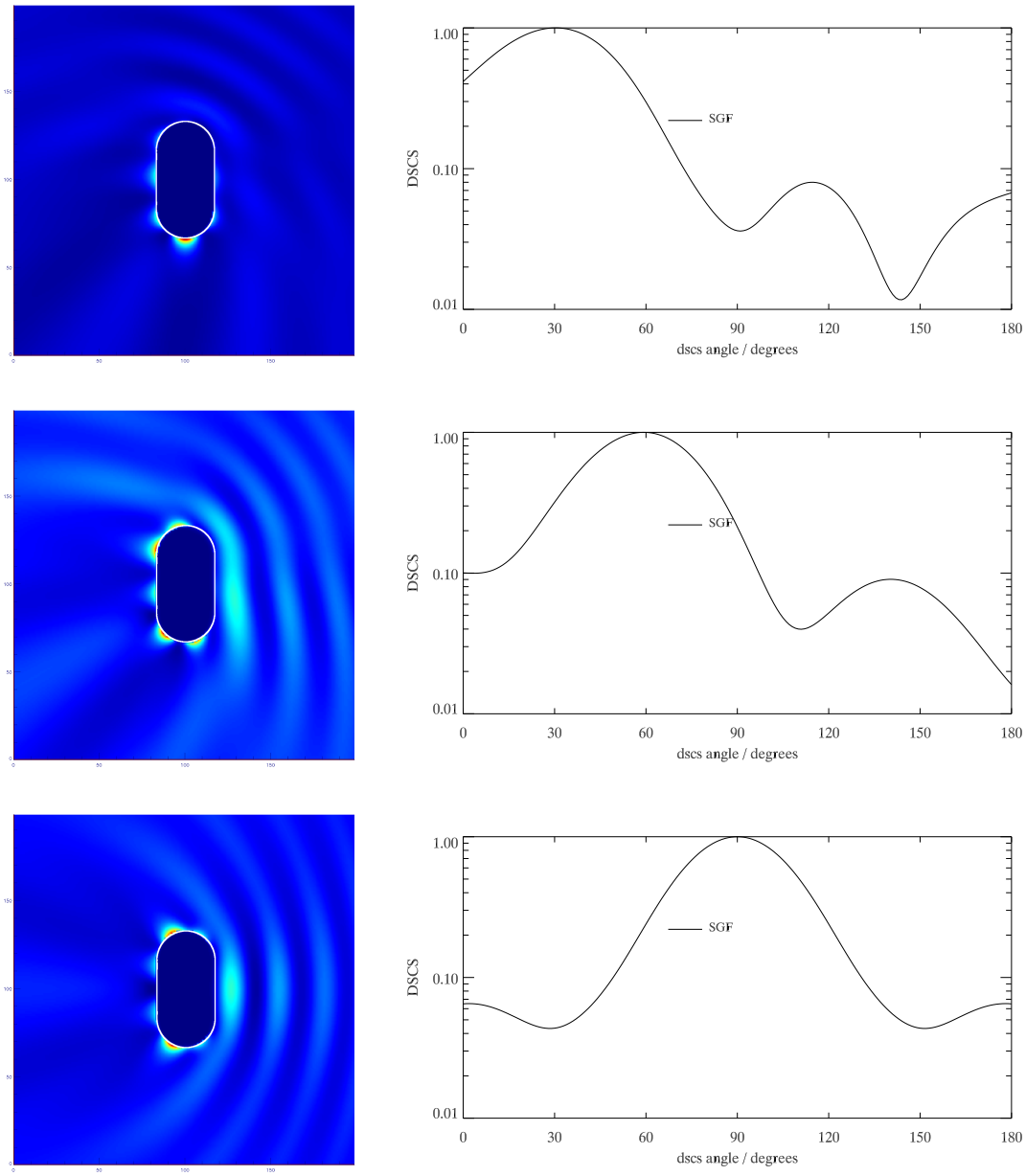

Figure 2.27: *Near fields and DSCS's for a gold particle with* $n \approx 0.32+3.18i$, $SP = 4$ *and* $AR = 2$ *illuminated at* $\Omega_k = 30°, 60°, 90°$ *(from top to bottom). The corresponding errors are* $\delta_{av} = 3.597 \times 10^{-4}$, $\delta_{av} = 4.419 \times 10^{-4}$, $\delta_{av} = 5.110 \times 10^{-4}$

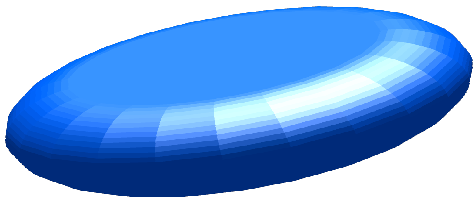

Figure 2.28: *Geometry of an flat (oblate) rounded cylinder*

symmetry axis and so there is no benefit to distributing sources in this way. We require a modification to our theory and we shall see that this naturally leads us to the idea of sources of radiation deposited in the complex plane.

2.5.2 Complex Sources

For flattened particles, it can be understood from an intuitive viewpoint that depositing sources along the symmetry axis of the particle leads again to a poorly conditioned problem, in much the same way as the localized source solution would be ill conditioned. Furthermore, we choose not to deposit the sources in some other area in real space (other than the symmetry axis), since our surface integrals would not simplify to $1-d$ integrals and so would become more complicated and time intensive to evaluate. In order to solve this problem, we use analytic continuation to generalize the SVWF's into the complex plane [59] such that the sources are distributed as shown in Fig. 2.5.2. These complex distributed sources fulfill our criteria of being complete, linearly independent solutions of the Maxwell equations [60].

2.5.3 Asymptotic form of imaginary distributed SVWF's

In order to find the far field properties of particles modeled with complex SVWF sources, we need to find the asymptotic form of these functions also. Consider the geometry illustrated in Fig. 2.30. By studying Fig. 2.30 we may make an analogous argument for the complex sources as we carried out

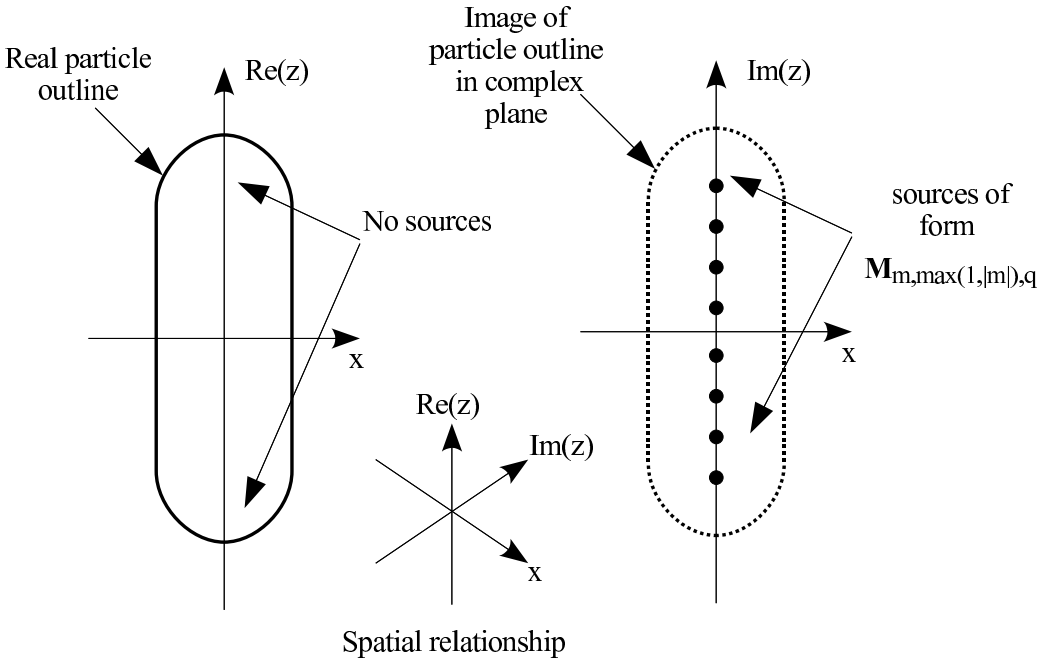

Figure 2.29: *The distribution of complex sources on the imaginary z axis.*

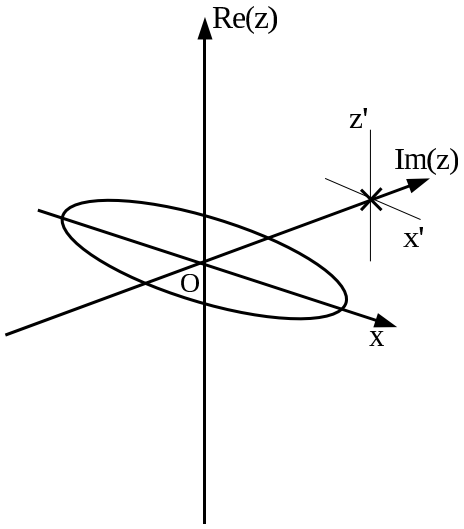

Figure 2.30: *A source deposited in the complex plane.*

for the sources deposited in the real plane. We can thus show that as the observation point moves to infinity:

$$r' \rightarrow r - iL\cos(\theta) \tag{2.39}$$

where L is real number that determines the distance of the source point along the imaginary axis from the particle coordinate system. Furthermore

$$\theta' \rightarrow \theta \tag{2.40}$$

and

$$\phi' \rightarrow \phi \tag{2.41}$$

From these relations we can show that the asymptotic form of the complex distributed functions, where each individual source on the complex axis is deposited some real distance L_q from the origin:

$$\tilde{\mathbf{M}}^{\infty}_{mq} \sim \exp\left(k_s L_q \cos\theta\right)\frac{\exp ik_s r'}{r'}(-i)^{n'+1}\mathbf{m}(\theta,\phi)_{m,n'} + 0(\frac{1}{r'^2}) \tag{2.42}$$

$$\tilde{\mathbf{N}}^{\infty}_{mq} \sim \exp\left(k_s L_q \cos\theta\right)\frac{\exp ik_s r'}{r'}(-i)^{n'}\mathbf{n}(\theta,\phi)_{m,n'} + 0(\frac{1}{r'^2}) \tag{2.43}$$

where the imaginary terms in the first exponents have eliminated each other.

2.6 Simulations of flattened particles

In order to illustrate the differing electromagnetic properties of prolate and oblate particles we shall study the corresponding flat dielectric particle to the elongated particle studied in Section. 2.4.4. We therefore choose our rounded cylinder to have $n = 1.50$, $SP = 13$ and $AR = 0.231$. First, in Fig. 2.31, we check the behavior of the average surface error as we alter the number of solution functions: We can see from Fig. 2.31 the general trend that increasing the number of solution functions decreases the error,

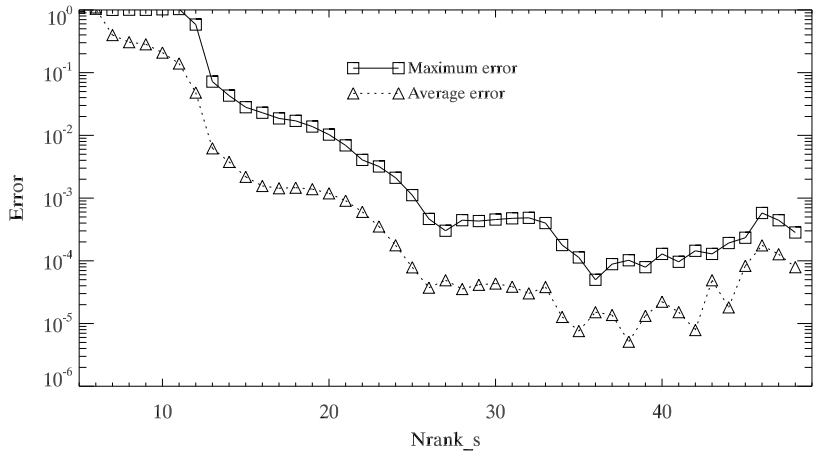

Figure 2.31: *Variation of δ_{av} and δ_{max} surface errors for a dielectric particle with $n = 1.50$, $SP = 13$ and $AR = 0.231$ illuminated axially for increasing numbers of solution functions.*

although there is a noticeable variation in the error level. The minimum error is approximately $\delta_{av} = 10^{-5}$ and is reached at $N_s = 37$ functions. We study the convergence of the DSCS is Fig. 2.32. We see that the DSCS in Fig. 2.32

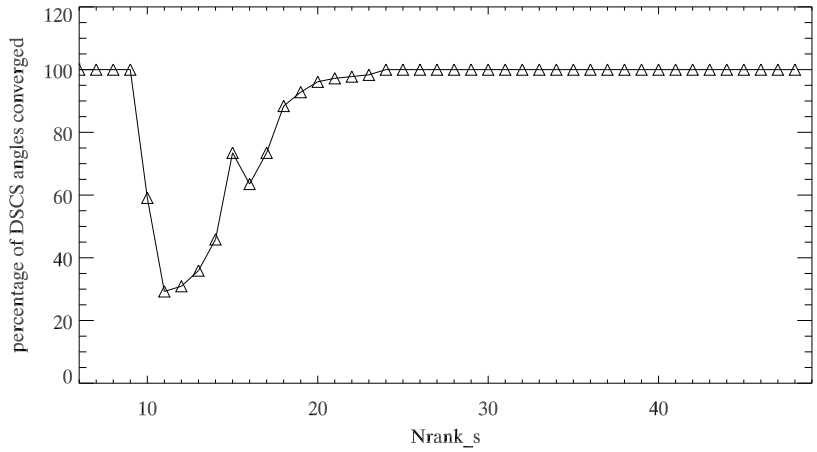

Figure 2.32: *Convergence of the DSCS for a dielectric particle with $n = 1.50$, $SP = 13$ and $AR = 0.231$ illuminated axially for increasing numbers of solution functions.*

displays false convergence but eventually converges at $N_s = 18$, ultimately progressing to 100% converged at $N_s = 24$ where it remains converged over the range considered. We may then select the solution with the number of sources at which we obtain the lowest error result and study how the error varies over the surface of the particle, which we show in Fig. 2.33. The error

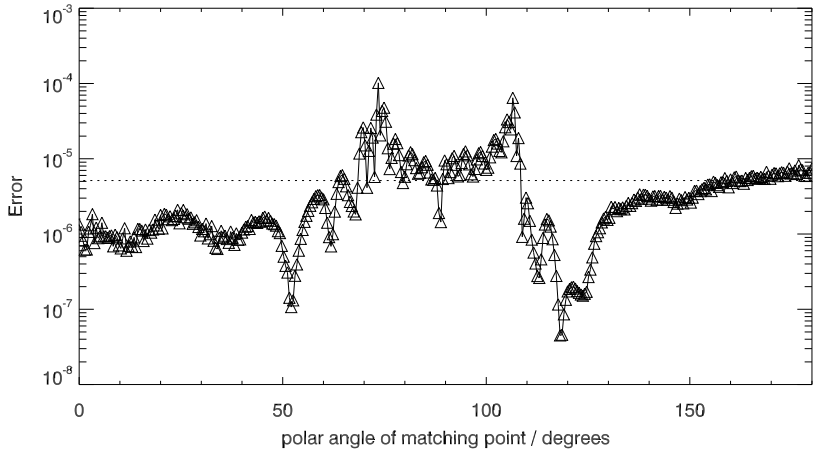

Figure 2.33: *Variation in δ_p as a function of matching point on the particle surface for a dielectric particle with $n = 1.50$, $SP = 13$ and $AR = 0.231$ illuminated axially for $N_s = 37$ functions $\delta_{av} = 5.097 \times 10^{-6}$.*

at the surface varies by around two orders of magnitude and is maximal at the discontinuities in the derivatives of the surface curvature. After studying these results we satisfy our requirements that our results are convergent with low average and maximum errors. We are confident in the quality of our solution and proceed to calculate the scattering properties in both the near and far field in Fig. 2.34.

Results for $\Omega_k \neq 0$

We may now study the near and far fields for this particle as a function of input beam angle. If we illuminate the particle at angles $\Omega_k = 30°, 60°, 90°$ and solve for an appropriate number of azimuthal modes ($M = 4$ in this

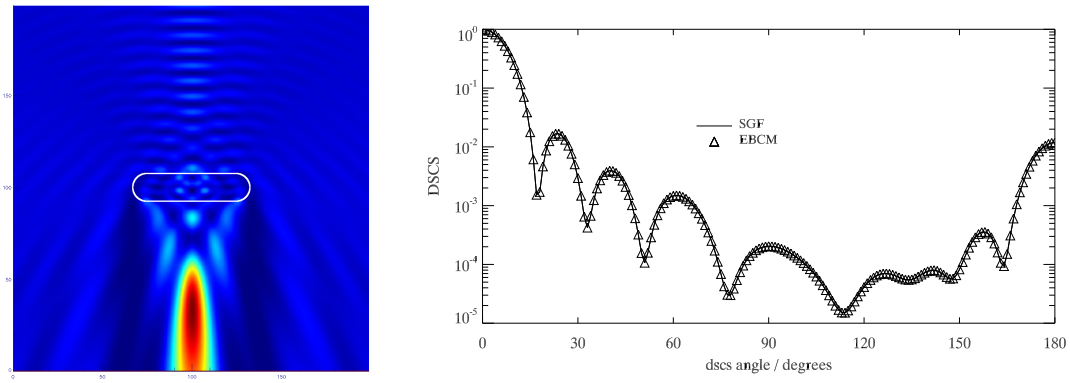

Figure 2.34: *Near field and DSCS for a dielectric particle with* $n = 1.50$*,* $SP = 13$ *and* $AR = 0.231$*. We overplot the results of the EBCM in the DSCS for comparison and see that the agreement between results is excellent.*

case), we produce the near and far field results shown in Figure. 2.35. We can see again that the intensity distribution is very sensitive to the input beam angle and that the cross sections are in excellent agreement with those calculated with the EBCM.

2.6.1 Flat metallic particles

Next we progress to study a gold particle with $n \approx 0.32 + 3.18i$, $SP = 4$ and $AR = 0.5$ and in the same was as previously discussed we may view the convergence of the average surface error and scattering cross section in Figs.(2.36-2.37) respectively. We can see that the error in Figure. 2.36 approaches $\delta_{av} = 10^{-5}$ as we increase the number of solution functions, and appears to converge smoothly. We also show the convergence of the DSCS in Figure. 2.37. We observe that the DSCS in Figure. 2.37 converges to total convergence at $N_s = 13$ functions where it remains converged over the range considered. If we select the solution with the number of sources at which we obtain the lowest error result we produce Fig. 2.38. Again, in Figure. 2.38, we see that the surface error is maximal at the points on the surface where there is a discontinuity in the derivative of the surface curvature. We plot

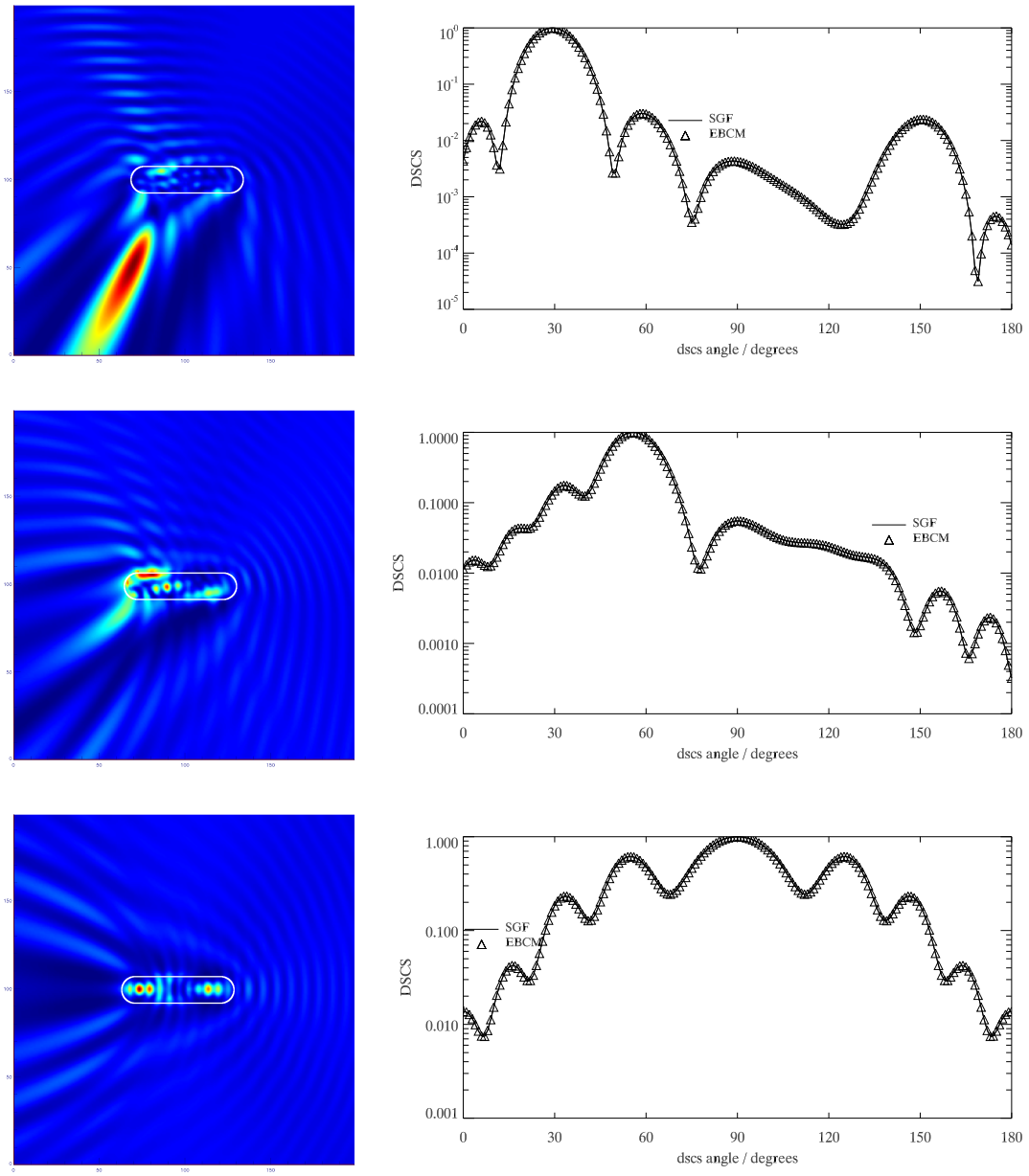

Figure 2.35: *Near fields and DSCS's for a dielectric particle with SP=10, AR=0.231, n=1.5 illuminated at* $\Omega_k = 30°, 60°, 90°$ *(from top to bottom). The corresponding errors are* $\delta_{av} = 8.527 \times 10^{-5}$, $\delta_{av} = 7.663 \times 10^{-5}$, $\delta_{av} = 9.419 \times 10^{-5}$.

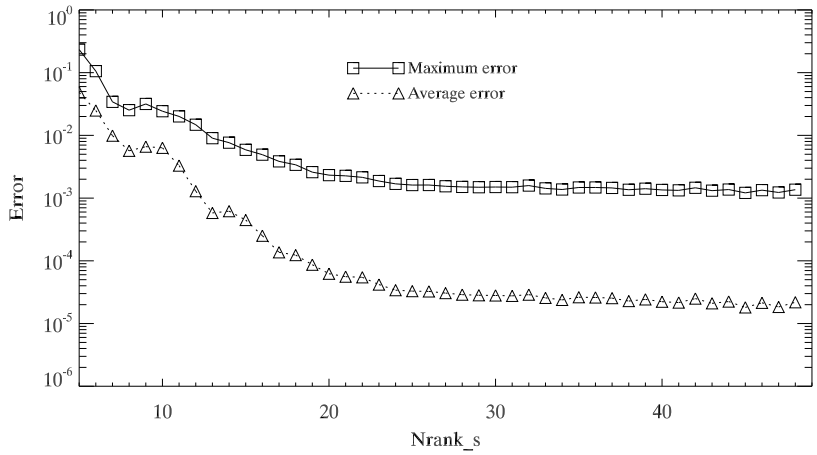

Figure 2.36: *Variation average and maximum surface errors for a gold particle with* $n \approx 0.32 + 3.18i$*,* $SP = 4$ *and* $AR = 0.5$ *illuminated axially for increasing numbers of solution functions.*

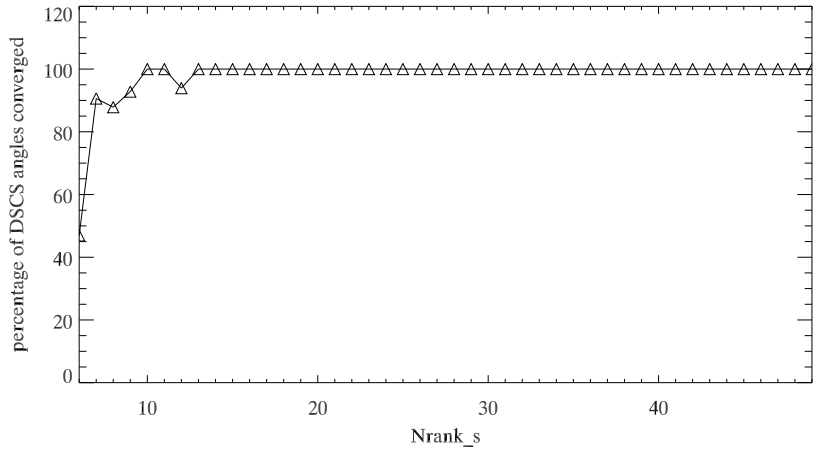

Figure 2.37: *Convergence of the DSCS for a gold particle with* $n \approx 0.32 + 3.18i$*,* $SP = 4$ *and* $AR = 0.5$ *illuminated axially for increasing numbers of solution functions.*

the near and far field for this particle in Fig. 2.39.

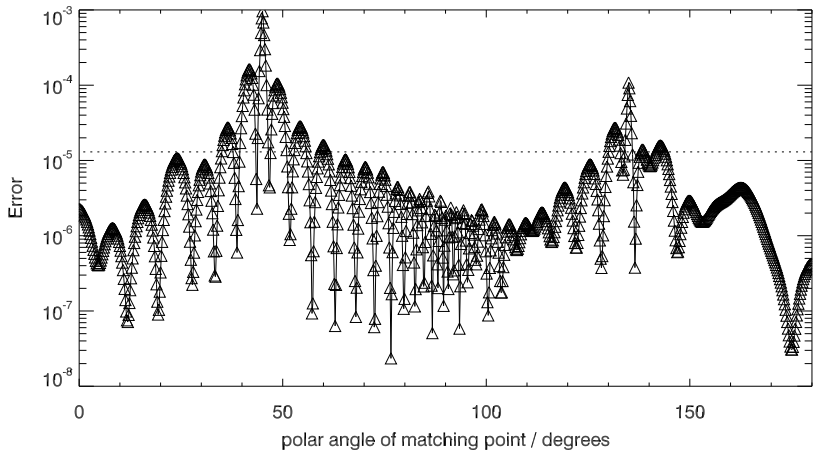

Figure 2.38: *Variation in δ_p as a function of matching point on the particle surface for a gold particle with $n \approx 0.32 + 3.18i$, $SP = 4$ and $AR = 0.5$ illuminated axially for $N_s = 50$ functions. showing $\delta_{av} = 1.498 \times 10^{-5}$.*

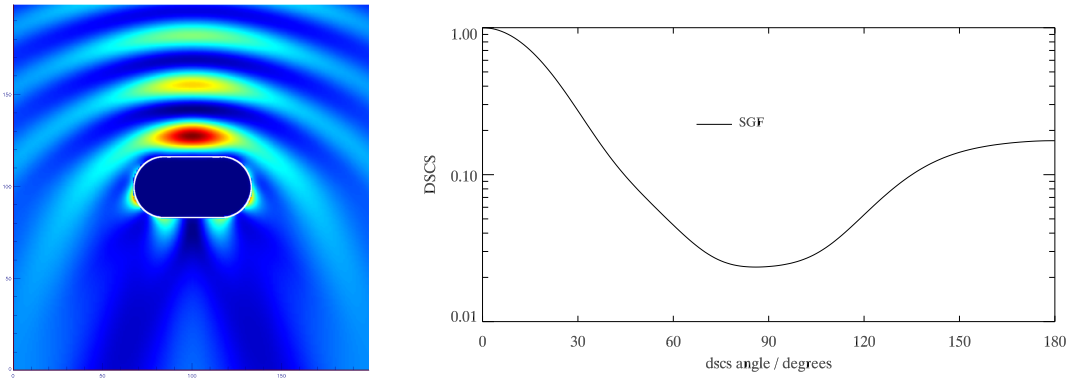

Figure 2.39: *Near field and DSCS for a gold particle with $n \approx 0.32 + 3.18i$, $SP = 4$ and $AR = 0.5$.*

Results for $\Omega_k \neq 0$

We may study the near and far field variation as a function of input beam angle for this metallic particle, which is shown in Figure. 2.40

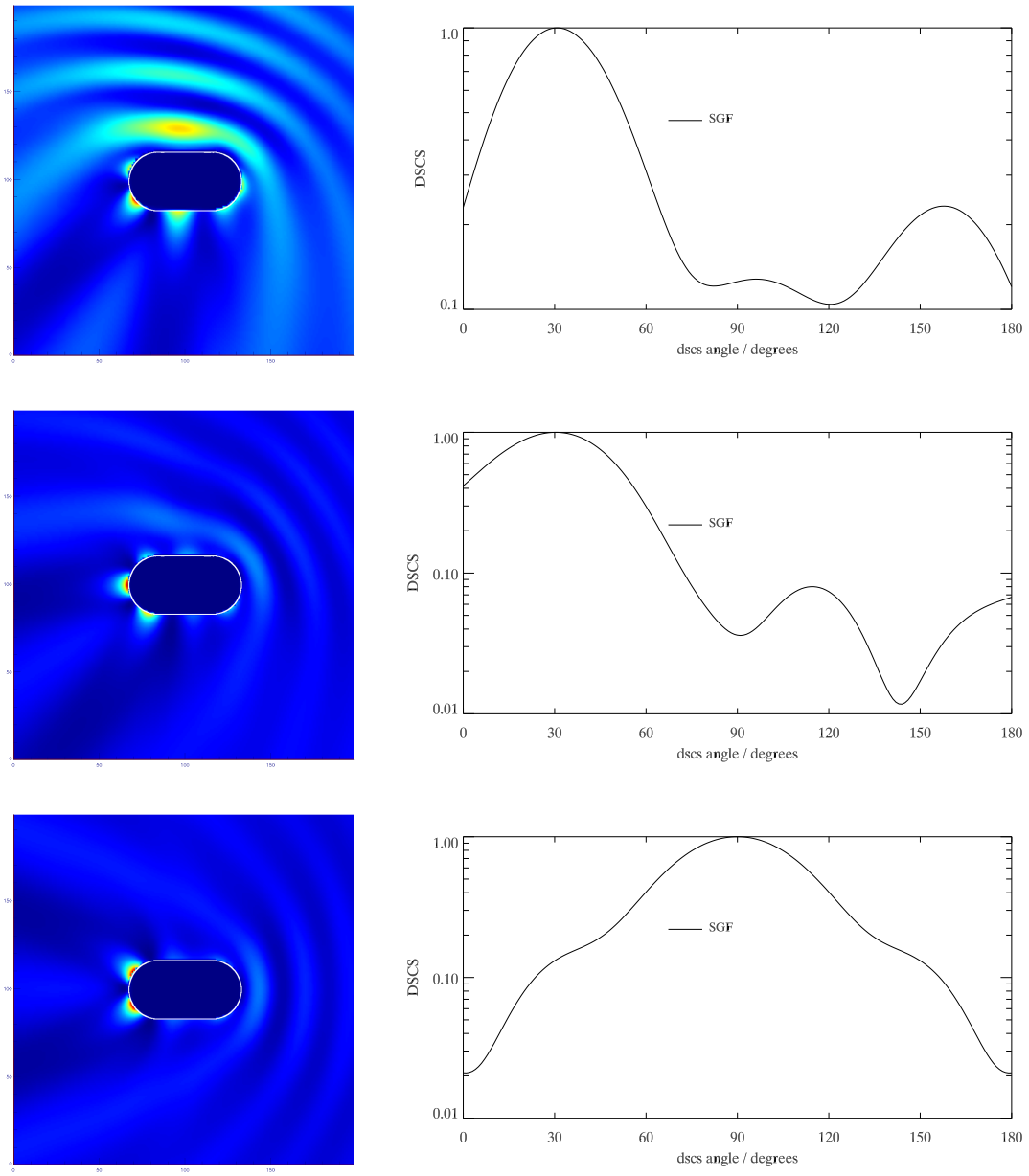

Figure 2.40: *Near fields and DSCS's for a gold particle with* $n \approx 0.32+3.18i$, $SP = 4$ *and* $AR = 0.5$ *illuminated at* $\Omega_k = 30°, 60°, 90°$ *(from top to bottom). The corresponding errors are* $\delta_{av} = 6.497 \times 10^{-5}$, $\delta_{av} = 5.503 \times 10^{-5}$, $\delta_{av} = 8.466 \times 10^{-5} \times 10^{-5}$.

2.6.2 Particle shapes

The analysis throughout this work is applicable to any shape of particle, provided it is axisymmetric and is generated by the rotation of a generatrix about the symmetry axis. As we have discussed, the main particle we shall study in this work is the rounded cylinder owing to its similarity to the majority of practically produced oblate and prolate nanoparticles and its difficulty to model due to the combination of straight and curved sections. However, we can just as easily generate our particle from the rotation of any generatrix about the axis of symmetry. In Fig. 2.41 we show the near field plots for a dielectric prolate cylinder with $SP = 12$, $AR = 6$, $n = 1.5$ solved for $N_s = 40$ functions and a gold oblate ellipsoid with $SP = 3$, $AR = 3$, $n \approx 0.32 + 3.18i$ also solved for $N_s = 40$ functions. The DSCS's for these particles and incident fields (not shown) match to a very high precision. Note the higher value of the error in Fig. 2.41 for the cylindrical particle. One of the most difficult challenges in the modelling of particles in computational electromagnetics (beside dealing with complex refractive indices) is the presence of edges in the particle to be modeled. For the cylinder, the system of functions is no longer complete on the surface (one of the fundamental requirements we specified in for our functions) due to the presence of sharp edges. We note however the ability of the method to model with the particle albeit with reduced accuracy. Contrastingly, the ellipsoidal particle has no edges whatsoever and as such the surface error is correspondingly less even though it is metallic. These examples illustrate the flexibility of the method, however, for the rest of this work the majority of the examples we study will be rounded top cylinders as previously justified.

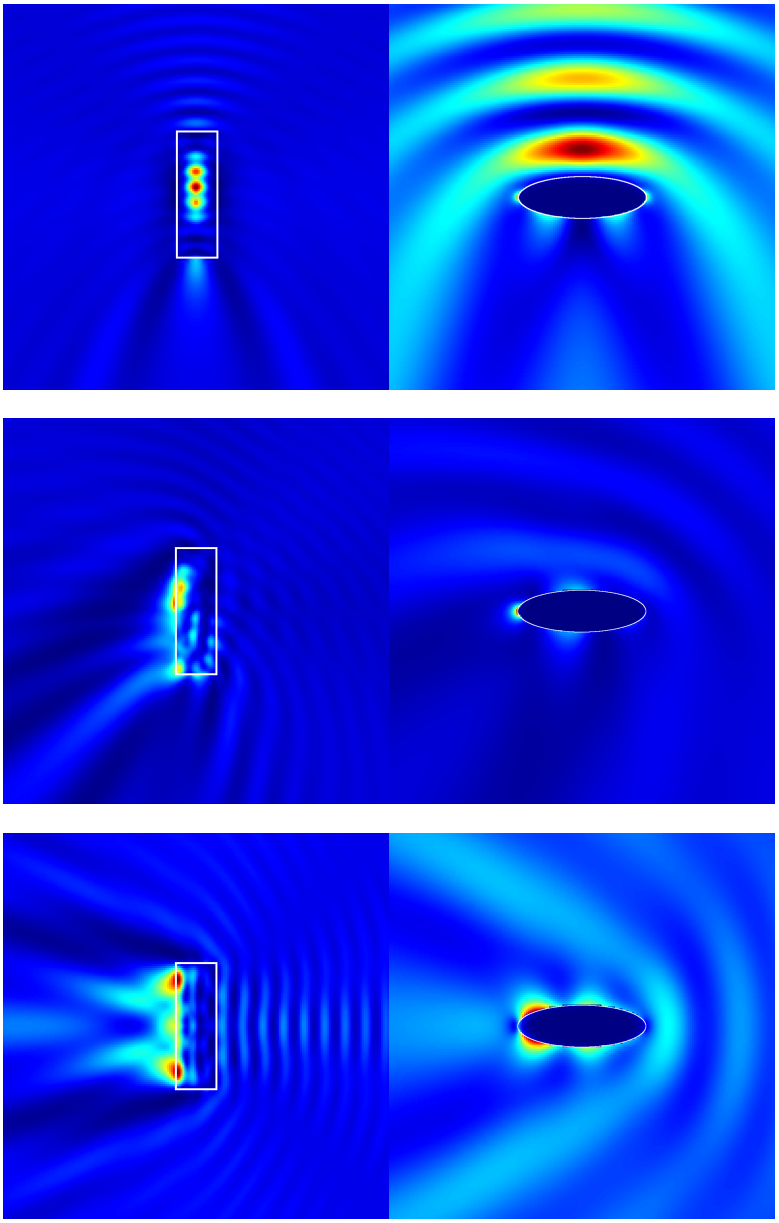

Figure 2.41: *Near fields for a dielectric prolate cylinder illuminated at* $\Omega_k = 0°, 45°, 90°$ *(left column and from top to bottom) and an oblate gold ellipsoid illuminated at the same angles (right column). The corresponding errors are* $\delta_{av}^{cylinder} = 8.491 \times 10^{-4}, 9.492 \times 10^{-4}, 9.566 \times 10^{-4}$ *and* $\delta_{av}^{ellipse} = 1.319 \times 10^{-6}, 1.679 \times 10^{-6}, 1.372 \times 10^{-6}$ *from top to bottom.*

Chapter 3

Improvements to the SGF approach

In Chapter. 2 we laid down theory which enabled us to find the electromagnetic properties of axisymmetric nanoparticles via Surface Green functions at any point in space, whether internal or external to the particle. We have discussed the practical evaluation of these Green functions via Singular Value Decomposition and outlined the modification of our theory to deal with particles that were either elongated or flat. We have used this theory to model several example particles, while studying the convergence properties, errors and near and far field behavior of these particles. In the following chapter we will make considerable refinements to our theory, we aim to define the error in our solutions in a more mathematically correct manner and find effective methods for evaluating these errors. We also investigate the practical evaluation of the SGF via SVD and modify our approach in an attempt to improve the accuracy of our solutions. We also aim to study the relative importance various parameters have in our solution error, in much the same way as we studied the surface error as a function of the number of solution functions in Chapter. 2. By doing so, we aim to find optimized SGF's which minimize our error for all possible excitation fields incident on our particle. By car-

rying out this optimization, we shall see that we can study wide families of particles with a tight control over the surface error. This enables us to study these families of particles to investigate how the size, shape and composition of the particles affect the distribution of near field intensity and measurable far field intensity.

3.1 Surface errors revisited

In Chapter. 2 we defined our surface error at a point on the surface as the ratio of the field residual at that point respect to the incident field at the same point.

$$\delta_p = \frac{|\mathbf{f}_p^0 - \mathbf{f}_p^i + \mathbf{f}_p^s|^2}{|\mathbf{f}_p^0|^2}, \tag{3.1}$$

and correspondingly we defined average and maximum errors. These are indeed well defined and useful measures of the error, especially when studying the surface error variation, but we believe that a more useful overall definition of the error makes use of the Euclidean norm of the fields on the surface. The L_2, or Euclidean, norm of a function $f(x)$ defined on an interval (a, b) is [61]

$$L_2[f(x)] = ||f(x)||_2 = \left(\int_a^b |f(x)|^2 dx \right)^{\frac{1}{2}}. \tag{3.2}$$

For surface integrals, this can be generalised to the surface norm

$$L_{2,S}[\mathbf{g}] = ||\mathbf{g}||_{2,S} = \left(\int_S |\mathbf{g}|^2 dS \right)^{\frac{1}{2}} \tag{3.3}$$

where $\mathbf{g}$ is a vector function defined on S. From this definition of surface norm, we can define an overall error for a single particle via

$$\delta_{L^2} = \frac{||\mathbf{f}_p^0 + \mathbf{f}_p^s - \mathbf{f}_p^i||_{2,S}^2}{||\mathbf{f}_p^0||_{2,S}^2}. \tag{3.4}$$

We therefore have a new definition of the error we wish to minimize in

our problem which is defined using surface integrals. We have a few options on how to proceed in the calculation of these surface integrals. Firstly, we note that for axisymmetric particles, the azimuthal integration is carried out analytically and as a result the surface integral reduces to a line integral:

$$\int_S |\mathbf{g}|^2 \, dS = \int_{\phi=0}^{2\pi} \int_{\theta=0}^{\pi} |\mathbf{g}|^2 \, r^2 \sin\theta d\theta d\phi = \sum_m \int_{\theta=0}^{\pi} |\mathbf{g_m}|^2 \, r^2 \sin\theta d\theta \qquad (3.5)$$

where $\mathbf{g}_m$ are the m components of an azimuthally symmetric vector field $\mathbf{g}$ defined at the surface. So in order to find the surface integrals for our error we in fact only have to perform a much simpler line integrals in θ.

3.1.1 Evaluating errors via numerical integrals

For the case as in Chapter. 2 where we solved our electromagnetic problem on a set of equally spaced points in θ, we may calculate the surface integral via the crude numerical sum:

$$\int_S |\mathbf{g}|^2 \, dS = \sum_{p=1}^{N_p} |\mathbf{g}_p^e|^2 r_p^{e2} \sin\theta_p^e, \qquad (3.6)$$

where the superscript e signifies that the points are equally spaced, θ_p^e are the set of discrete angles at the matching points and r_p^e are the corresponding radial coordinates of the points.

However, there are far more accurate, stable and reliable methods of calculating these types of integrals that involves Gaussian Legendre quadrature [62]. One possibility is that we could continue to solve our problem by point matching at arbitrary equally spaced points along the generatrix and then re-evaluating the fields at the Gaussian quadrature points to form the error. However, this is computationally wasteful and may not give the best measure of the error. Instead we can choose to point match and solve our problem at the Gaussian quadrature points which are used in the calculation of the error.

This saves computational time by removing the need for field re-evaluation. The new form of the sum using Gaussian quadrature would be:

$$\int_S |\mathbf{g}|^2 \, dS = \sum_{p=1}^{N'_p} |\mathbf{g}_p^G|^2 w_p^G r_p^{G2} \sin\theta_p^G, \tag{3.7}$$

where the superscript G signifies the matching points are chosen via Gaussian quadrature, the factor w_p^G is the Gaussian weighting factor and N'_p is the number of matching points with $N'_p = max\{N_p, N_G\}$ where N_G is the number of points required in the Gaussian integration to have integral convergence. Obviously, we must ensure that the number of matching points is large enough so that the integral converges..

We can, however, take our evaluation of the error one step further. As previously discussed, we aim to minimize the residual at the particle surface in a least squares sense such that

$$\sum_p |\mathbf{f}_p^0 + \mathbf{f}_p^s - \mathbf{f}_p^i|^2 = \sum_p |\mathbf{f}_p^R|^2 \tag{3.8}$$

is minimal where $\mathbf{f}_p^R$ is the total residual summed over all fields. However, since our error δ_{L^2} is defined in terms of surface integrals, we can instead choose **not** to minimize the sum of the residuals around the particle but instead minimize δ_{L^2} directly. We can do this by taking advantage of the fact that we are evaluating the functions at the particle surface at the Gaussian quadrature points and by rescaling the functions in our linear system such that:

$$\mathbf{f}^G \rightarrow \mathbf{f}^G \sqrt{w_p^G r_p^{G2} \sin\theta_p^G} = \mathbf{f}^{R,G} \tag{3.9}$$

Where $\mathbf{f}^{R,G}$ denotes the rescaled functions evaluated at the Gaussian quadra-

ture points. In this way, our least squares solution now minimizes:

$$\sum_p |\mathbf{f}^G \sqrt{w_p^G r_p^{G2} \sin\theta_p^G}|^2 = \sum_p |\mathbf{f}^G|^2 w_p^G r_p^{G2} \sin\theta_p^G \tag{3.10}$$

which is exactly the definition of the surface integral which forms our error in Eqn. 3.7. Thus by rescaling the functions used in our linear system and point matching at the Gaussian quadrature points we can minimize the δ_{L^2} error directly.

3.1.2 Comparison of error calculations

We will now study the relationship between the various errors that come from the different possible methods of calculating the surface integrals. To recap, we will study the error formed by:

1. Point matching our problem at equally spaced matching points and evaluating our integral error by re-evaluating our surface fields at the Gaussian quadrature points.

2. Point matching our problem at the Gaussian quadrature points and calculating our integral error using the fields defined at these points.

3. Point matching our problem at the Gaussian quadrature points with rescaled functions and calculating our integral error using the fields defined at these points.

In theory, methods one and two should give a similar error as the basic principle is the same, method one just requires an additional computational step of re-evaluating the fields at a different set of points than the problem was solved for. This additional computational step has the possibility of introducing error. The third method should give lower error estimates since, as discussed, we minimize the surface integral directly. We evaluate these errors for an example particle in Fig. 3.1. It can be seen from Fig. 3.1 that

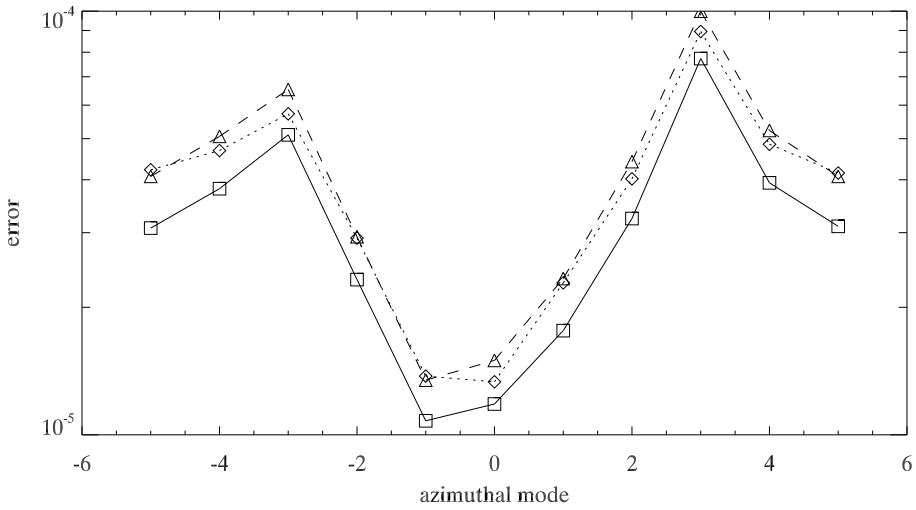

Figure 3.1: *δ_{L_2} for the various azimuthal modes for a prolate (flat) dielectric rounded ellipsoid (SP=12, AR=6, n=1.5) illuminated by an plane wave at $\Omega_k = 45°$. The errors are evaluated with 1) equally spaced matching points, field re-evaluation and Gaussian quadrature integration (triangles) 2) Gaussian quadrature matching points and Gaussian quadrature integration (diamonds) and 3) Gaussian quadrature matching points with rescaled functions and Gaussian quadrature integration (squares).*

the errors become progressively better for all modes as we move from the simple method of solving our problem on a set of equally spaced matching points to using matching points at Gaussian quadrature nodes with rescaled functions. Thus we can see that by rescaling our functions and using an appropriate set of matching points we can decrease the error in our solutions.

Comparison of δ_{L_2} and δ_{av}

In this work we have studied the errors of simulations of particles in terms of two errors. In Chapter. 2 we introduced the measure δ_{av}, which was the average size of the residual with respect to the incident field at each matching point. In this chapter we have introduced δ_{L_2}, the integral norm error. We highlight this distinction for clarity, the reasons behind the differing error selections are mostly historical. In reality, both errors are useful. Since δ_{av} is defined in terms of the average error at all the points on the surface, it (and

δ_p) enable us to study how accurate our field solutions are at different points on the surface, which could be of crucial importance in the study of surface effects of particles. The δ_{L_2} error is more useful in providing an overall estimate of the error for the particle and has a more strict mathematical formulation in terms of the Euclidean norm.

3.1.3 Azimuthal and total errors

We must also be careful in this work to understand the difference between the total error for a particle δ_{L_2} which takes into account fields from all azimuthal modes considered in the solution, and the individual azimuthal mode errors $\delta^m_{L_2}$. Extra care must be taking when comparing errors from different azimuthal modes since a large error calculated for only one mode does not necessarily mean that summing across all modes will produce a solution that is invalid, since the mode in question may contribute a vanishingly small contribution to the solution field. In fact, in general, as the order of the azimuthal modes increases, the error **for that mode** increases while the field contribution **of that mode** to the total solution field decreases. Therefore we cannot simply add the errors in the final error estimate as the sum of the individual azimuthal mode errors.

$$\delta_{L_2} \neq \sum_{m=-M}^{M} \delta^m_{L_2} \tag{3.11}$$

Instead we must sum the errors as

$$\delta_{L_2} = \frac{\sum_{m=-M}^{M} ||\mathbf{f}^0_p + \mathbf{f}^s_p - \mathbf{f}^i_p||^m_{2,S}}{\sum_{m=-M}^{M} ||\mathbf{f}^0_p||^m_{2,S}}, \tag{3.12}$$

such that the vanishingly small contributions in the fields from larger azimuthal modes are given their proper weighting in the evaluation of the total error.

3.2 Modifications to the SVD

The pseudoinverse via SVD described in Chapter. 2 could be calculated to an arbitrary precision by using every singular value to calculate the pseudoinverse. Practically, however, the SVD is calculated using computational methods and as a result there are numerical issues which can affect the accuracy. For instance, we will see that in the solution of electromagnetic problems there can be tens of orders of magnitudes between the magnitudes of the largest and smallest singular values and as such the small singular values can be heavily influenced by numerical noise and need to be treated carefully. However, since we know the many of our singular values may be affected by noise we may take steps to minimize the error we introduce into our solution. We can, in fact, choose a value below which the singular values are discarded, thus building a so called truncated SVD. This serves to remove the singular values which are most susceptible to numerical noise. We will see that using the truncated SVD can be advantageous in our analysis, and study it in more detail in 3.2.1.

3.2.1 Truncated SVD

Consider the general form of the SVD as discussed in Section. 2.1.4 where we decomposed our original matrix via:

$$\mathbf{A} = \mathbf{U}\mathbf{S}\mathbf{V}^H \tag{3.13}$$

where $\mathbf{U}$ was an $m \times m$ unitary matrix with entries $u_{ij} \in \mathbb{C}$, $\mathbf{V}$ was an $n \times n$ unitary matrix with entries $v_{ij} \in \mathbb{C}$ and $\mathbf{S}$ was an $m \times n$ matrix which is zero

everywhere except for the main diagonal which contained the entries $\sigma_i \in \mathbb{R}$ with $\sigma_i \geq 0$.

The truncated SVD of the same matrix is defined in a similar way, although instead of using all of the $min(m, n)$ singular values of the matrix we only use the r largest values, where $r < min(m, n)$, thus producing the approximation [63]:

$$\mathbf{A} \approx \mathbf{U}_r \mathbf{S}_r \mathbf{V}_r^H \tag{3.14}$$

where $\mathbf{U}_r$ is an $m \times r$ unitary matrix with entries $u_{ij} \in \mathbb{C}$, $\mathbf{V}_r$ is an $r \times n$ unitary matrix with entries $v_{ij} \in \mathbb{C}$ and $\mathbf{S}_r$ is an $r \times r$ matrix with the r largest singular values on the main diagonal in decreasing magnitude. This change in structure of the matrix $\mathbf{S} \rightarrow \mathbf{S}_r$ is illustrated in Eqn. 3.15.

$$\begin{bmatrix} \sigma_1 & 0 & 0 \\ 0 & \sigma_2 & 0 \\ 0 & 0 & \sigma_3 \\ 0 & 0 & 0 \\ 0 & 0 & 0 \end{bmatrix} \rightarrow \begin{bmatrix} \sigma_1 & 0 \\ 0 & \sigma_2 \end{bmatrix} \tag{3.15}$$

Where we stress that there matrices $\mathbf{U}$ and $\mathbf{V}$ are reduced in size also, such that the matrix multiplication which forms the approximation is well defined. The truncation of an SVD can be of use not only in decreasing the number of numerical calculations needed in the evaluation of the SGF, but can also serve to remove values dominated by noise which are detrimental to the error in the solution. In practice we may choose to truncate off any values with $\sigma_i < \epsilon^t$, where ϵ^t is the truncation parameter. We effectively define a floor in the singular value spectrum below which we assume the singular values are dominated by noise and so will not be used in our decomposition. We will see later that the value of the parameter ϵ^t can drastically affect the error in our solution, and we will aim to find the best parameter for a particular problem that minimizes this error. The effect of truncated SVD is discussed

in greater detail in Section. 3.2.2.

3.2.2 Truncated SVD and error

In order to understand the implications of using the truncated SVD on the solution of our linear systems, it is helpful to have a clear idea of the relationship between the singular values. The singular value spectrum for a matrix used in the evaluation of a SGF for a typical particle (a rounded cylinder with $n = 1.5$, $SP = 9$ and $AR = 4.5$ for the $m = 1$ mode) is shown in Fig. 3.2. Note the spectrum in Fig. 3.2 is for one azimuthal mode only.

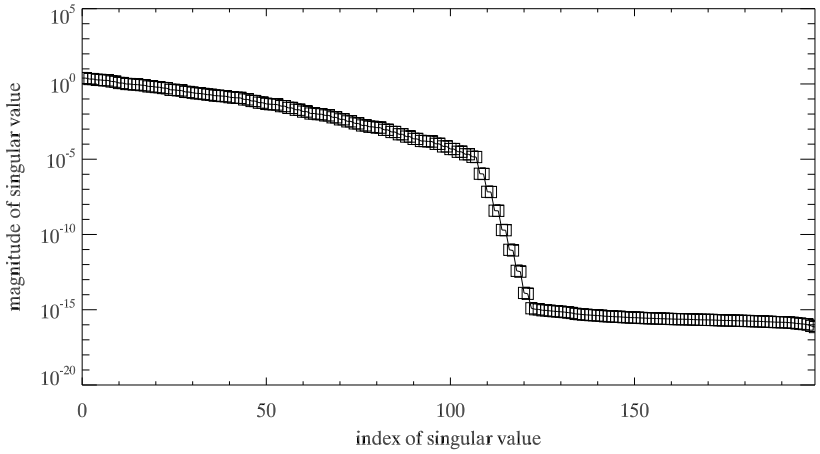

Figure 3.2: *A typical singular value spectrum encountered in the evaluation of the SGF of a particle.*

There are of course similar graphs for the rest of the azimuthal modes used in the solution of the problem in question. We can identify three distinct areas in the singular value spectrum from Fig. 3.2:

1. For the largest singular values, there is a gentle but noticeable decrease in the magnitude of the singular values

2. At a particular singular value index, there is a rapid transition in the spectrum where the magnitude of the singular values decrease rapidly.

3. For the lowest singular values, there is effectively a plateau in the spectrum.

The relative positions and proportions of these spectrum features change from particle to particle, but are almost always present in all spectra, for all particles and azimuthal modes we consider in our study. At first glance, it is natural to treat the smallest singular values with caution since their numerical value relative to the largest singular value is of the same order as the precision of our calculations (the machine precision in double precision). We thus suspect that these values may have be subject to numerical noise and including these may be detrimental to our approximation of our SGF and ultimately the error in the solution of our problem. We will thus study the effect of truncating the SVD of our matrix at various levels on the error in the solution when a particular excitation field is incident upon our particle. We can envisage the structure of the truncated matrices used by examining the singular value spectrum with the various truncation levels as shown in Fig. 3.3. If we then choose to have the particle in question have a plane

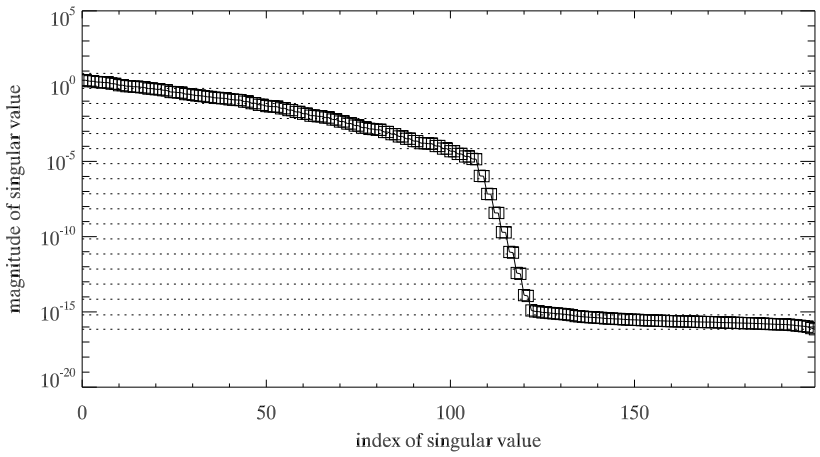

Figure 3.3: *The singular value spectrum from Figure. 3.2 with possible truncation levels shown as horizontal dotted lines. The lowest horizontal line represents no truncation while the highest is total truncation. As we move vertically from one truncation line to another we produce smaller truncated matrices.*

wave incident upon it with $\Omega_k = 45°$ and study the error in our solution as a function of the truncation levels as shown in Fig. 3.3, we produce Fig. 3.4.

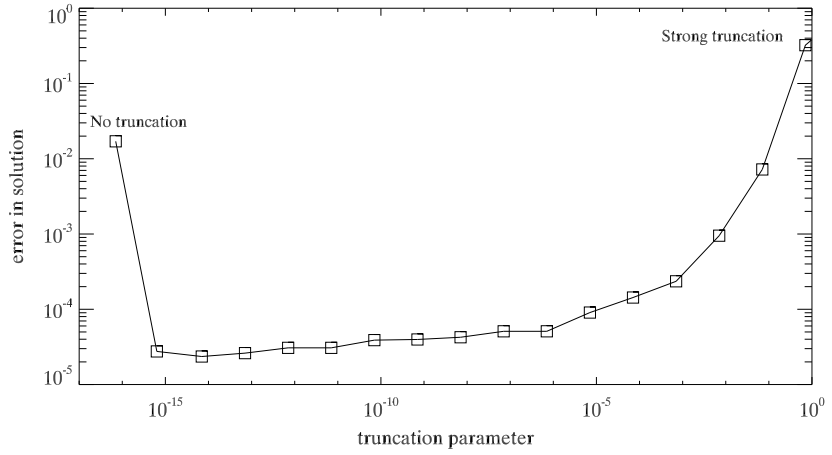

Figure 3.4: *L_2 error as a function of truncation parameter for the particle corresponding to Figure. 3.2 when subject to a plane wave at $\Omega_k = 45°$. We see that there is an optimum level of truncation at which the error is minimal. In this case, the optimum truncation level corresponds to the third horizontal line from the bottom in Fig. 3.3 with corresponding optimal error $\delta_{L_2} = 2.360 \times 10^{-5}$.*

If we study similar graphs to Figs.(3.3-3.4) for a wide variety of particles and input fields we find a very common trend about the optimal level of truncation. We find that the optimal place to truncate our singular value spectrum is at the last point before the lower plateau in the spectrum begins. This gives quantitative evidence to support our concerns that the lower plateau may contain singular values which are significantly affected by noise. We thus refer to the lower plateau from now on as the noise level, and we aim to always truncate our system at this optimal point. We will discuss the practical aspects of doing so when we discuss optimization in a broader sense, in Section. 3.3.

3.3 Optimization

We have previously discussed the fact that one of the main advantages of the SGF method is that once we calculate a suitable approximation of the SGF, it may be stored and re-used for any possible incident field. It is therefore important to ensure that our initial evaluation of the SGF is to a sufficiently high quality to be able to produce results with low errors in any given situation. We therefore aim to optimize our analysis and be able to calculate optimal SGF's for particles, as the additional initial effort in calculating the optimized SGF is justified since it is being stored ad re-used potentially many times. We define our SGF's to be optimal if they are constructed via a specific set of parameters which minimize our error for all possible incident fields. Before we proceed it is important to have an idea of some of the fundamental concepts in the field of optimization and we will outline some of the basic concepts of optimization in Section. 3.3.

3.3.1 Global and Local minima

The field of optimization is a broad with many analytical and computational techniques depending on the particular problem in question, and a broad overview can be found in [64]. We aim to highlight some key concepts, advantages and limitations through a simple example. Suppose we solve some general numerical problem computationally and the solution has an error associated with it. Let us further assume that we have no *a priori* method of calculating the error of this problem, but we wish to minimize the error in our solution. If the problem is one involving two variables a and b, and the error function is denoted by $f(a, b)$, we wish to find the values of a and b such that f is minimal. We can think of our error function f as being a surface plot of the two variables a and b as shown Fig. 3.5. In Fig. 3.5 we aim to highlight the distinction between the local and global minimum for the problem. A local minimum is defined as being any point

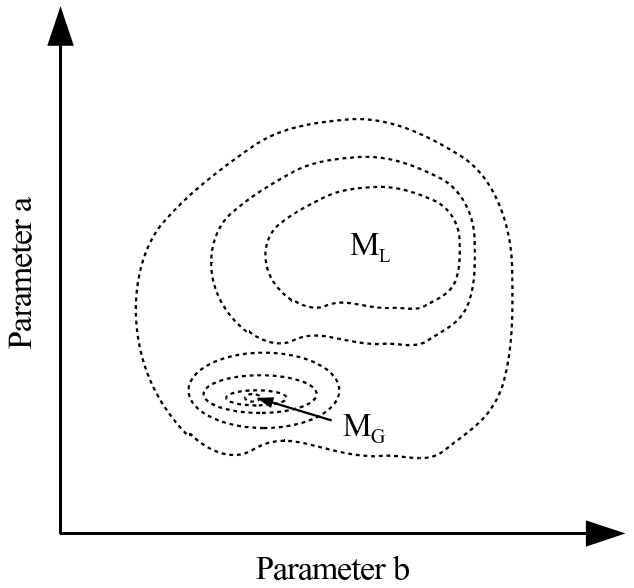

Figure 3.5: *A contour plot of the error in a general numerical problem as a function of two independent variables showing both a global and local minimum, M_G and M_L, respectively. We assume that the entire parameter space for these variables is shown.*

in the parameter space where moving some infinitesimal distance along any direction results in a larger error. Furthermore, the global minimum is simply the lowest overall local minimum in the entire parameter space. Finding global minimum is, in general, a computationally expensive process as a very high number of calculations need to be performed. Additionally, the parameter space may not be bounded and so the lowest minimum in some subset of the space is not necessarily the true global minimum. In our analysis we do not attempt to find the global minimum in our parameter space as this would be computationally very demanding. We can, however, optimize our SGF's such that we can find local minima in our parameter space with relatively low cost. In this way, we aim to drive down the errors in our solutions and study wider ranges of particles than would be possible without any optimization procedures. The procedure in finding a local minimum is shown in Fig. 3.6. We see in Fig. 3.6 that we begin our optimization procedure

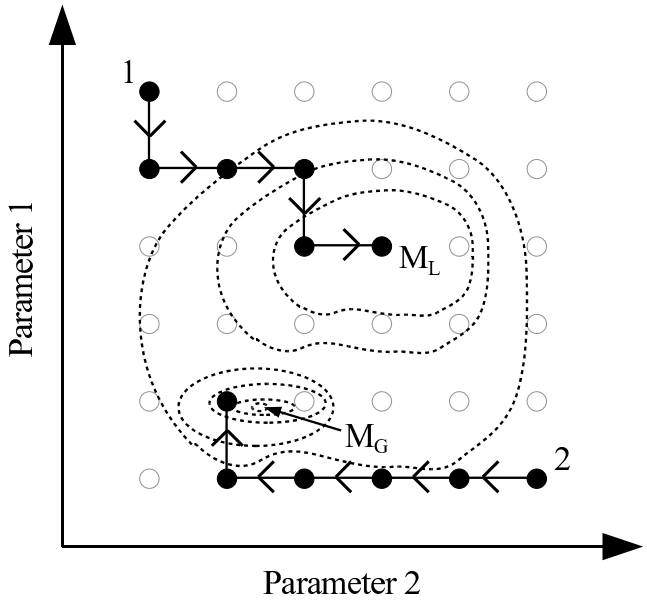

Figure 3.6: *A diagramatical representation of the search for a minimum in a general parameter space. The circles represent a grid at which the error in the solution can be evaluated, darkened circles represent the "walk" of the optimal error through the space until a local minimum is found. The explicit shape of the function we are sampling at the grid points is not known at points off the grid, although it is shown for illustrative purposes. We can see that different initial guesses of parameters can lead to different minima found by the optimization procedure.*

by guessing some combination of parameters at point 1. We may then sample the errors at the nearest neighbors of the initial parameter guess combination. By selecting the surrounding point with the lowest error and repeating the same procedure at this new point we "walk" through the parameter space always moving to a point with a parameter combination with lower error. Eventually we reach a combination where a specific point is a local minimum and the optimization procedure stores the parameters for this local minimum. We can see from Fig. 3.6 that the selection of the initial guess can affect the minimum where the optimization procedure stops.

We now move form this general example of an optimization procedure to our electromagnetic problem, where we must find a suitable set of parameters

to optimize over.

3.3.2 Selection of optimization parameters

For our electromagnetic problem we saw in Chapter. 2 that differing numbers of solution functions had an effect on our error. There are, however, several solution factors which can affect our error which we kept constant in Chapter. 2. Explicitly, factors which affect the error in our solutions are:

1. The total number of solution functions used (which we have studied in Chapter. 2)

2. The ratio between the number of functions for the internal and external fields

3. The number of matching points used on the surface (i.e. how overdetermined our linear system is)

4. The position of the distributed sources within the particle

5. The number of singular values in the solution which are used

Each of these factors can affect our error, although some are more important than others. It is important to find a minimum set of factors we wish to optimize over since the number of operations needed in our optimization procedure increases exponentially with the number of parameters we optimize over. The ratio between the number of functions used for the internal and scattered fields is important, however it has been shown in related electromagnetic studies [51] that the optimal ratio should be equal to the relative refractive index between the two materials. In this way, we use more functions for the expansion of the internal field than the scattered field. The number of matching points (i.e. the degree to which our system is overdetermined) can also be set at a fixed level between $2-4$ [51] times the total number of solution functions used for the problem, such that the system is

overdetermined but not unnecessarily so. We thus do not need to optimize over these parameters since well established criteria already exist.

However, we have already seen in Chapter. 2 that the overall error in our solution varies strongly with the number of functions used in the solution and so we choose this to be one of our optimization parameters. Additionally, we have seen in Section. 3.2.2 that by making use of the truncated SVD, we can greatly decrease the error in our solutions, we thus choose this truncation level to be our second optimization parameter. Finally, we suspect that the error in our solution may vary with the position of sources within the particle, but a quantitative analysis is needed, which we shall now study.

Error as a function of distributed source location

In Chapter. 2 we discussed the fact that we placed the distributed sources evenly on the symmetry axes when modeling elongated or flat particles. We distribute sources such that they are evenly spaced but we have control over how close we allow the sources to come to the particle surface, as indicated in Fig. 3.7. We give the length L_{prox} as the percentage distance from the surface with respect to the size parameter of the particle. Therefore, if we were to place sources over only half the total length of the symmetry axis we would have $L_{prox} = 25\%$. We may study how our surface error varies as we change the proximity of sources to the surface for example particles, and we show these results in Figs.(3.8-3.9). We can see from Figs.(3.8-3.9) that the surface error does indeed vary significantly with the proximity of the sources to the surface. These results are typical of the behavior for a variety of particles, the lowest errors are typically found when $L_{prox} < 10\%$. However, the precise optimum value of L_{prox} for different particles does not vary in a predictable way and so we choose to optimize this parameter also in our optimization set.

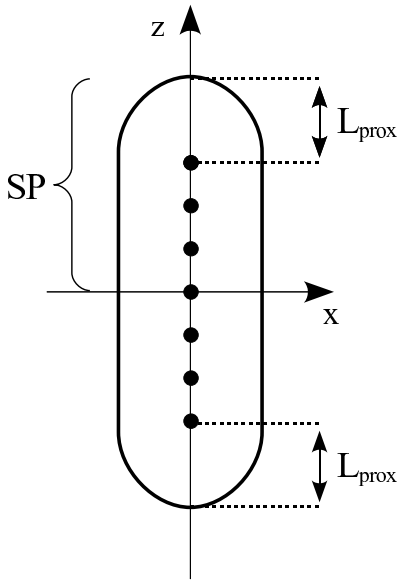

Figure 3.7: *A typical prolate particle showing the location of the distributed sources on the symmetry axis, with minimum separation from the surface* L_{prox}.

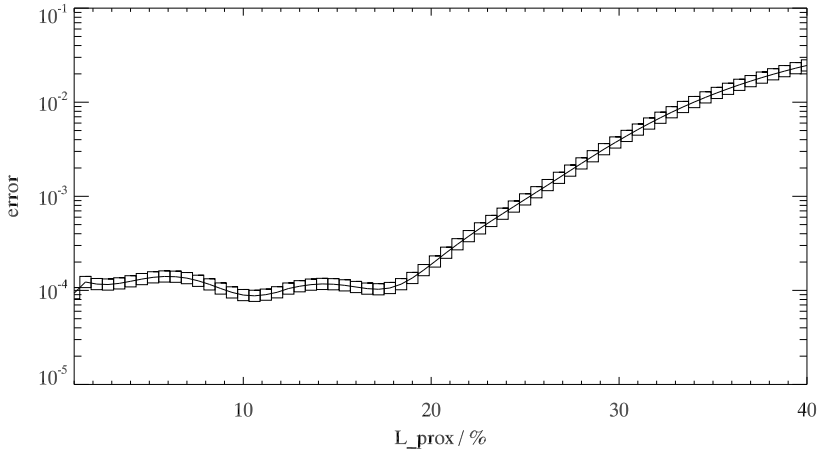

Figure 3.8: δ_{L_2} *for the* $m = 1$ *mode as a function of* L_{prox} *for a prolate dielectric ellipsoid with* $n = 1.5$, $SP = 9$ *and* $AR = 4.5$, *illuminated at* $\Omega_k = 45°$ *for* $N_s = 30$ *solution functions.*

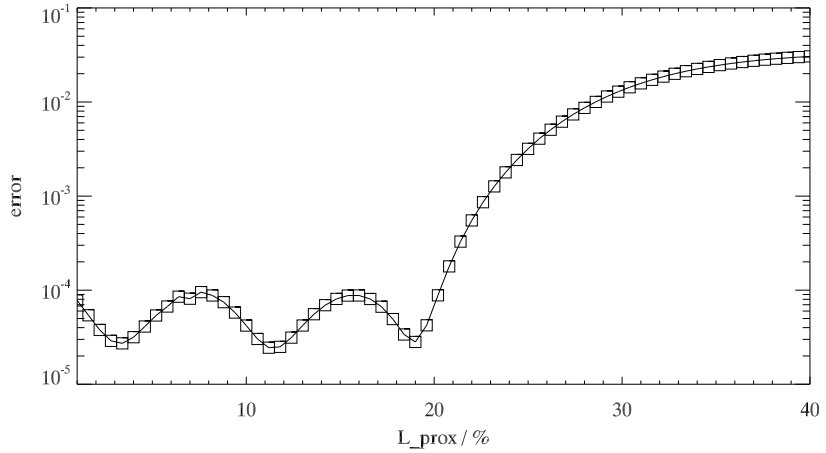

Figure 3.9: *δ_{L_2} for the $m = 1$ mode as a function of L_{prox} for an oblate dielectric ellipsoid with $n = 1.5$, $SP = 9$ and $AR = 0.22$, illuminated at $\Omega_k = 45°$ for $N_s = 30$ solution functions.*

3.3.3 Practical optimization considerations

Now that we have identified the three main parameters that we with to optimize, namely the number of solution functions, the SVD truncation parameter and the distributed source surface proximity we may consider the practical implementation of our optimization procedure. Recall that we require to solve our problem for a range of azimuthal modes, and as such there are two ways main ways in which we can choose to optimize our problems:

1. Optimize for **one** set of parameters that are used in the calculation of all azimuthal modes. We produce a global set of parameters $\mathbf{P_{opt}} = \{\alpha_{opt}, \beta_{opt}, ...\}$ which are used in the solution for each mode $-M \leq m \leq M$, where α_{opt} is the optimum value of some parameter α which affects our error. Similarly for β, and any other parameters we optimize over.

2. Take advantage of the natural azimuthal mode decoupling of the problem and optimize each azimuthal mode individually, thus producing a set of optimal parameters indexed by each mode $\mathbf{P_{opt,m}} = \{\alpha_{opt,m}, \beta_{opt,m}, ...\}$

for each mode $-M \leq m \leq M$. Here, the optimal parameters have only been optimized for **one** azimuthal mode.

Since the problem we are solving naturally decouples into a series of problems over a set of azimuthal modes we should be able to produce a lower error by optimizing over each mode individually, rather than optimizing all modes together.

Next, before we begin our optimization procedure we must decide which error we wish to minimize. Throughout we shall always use the δ_{L_2} error, but we may either optimize the average or maximum δ_{L_2}. We highlight the distinctions and outline our general optimization procedure in Fig. 3.10. The

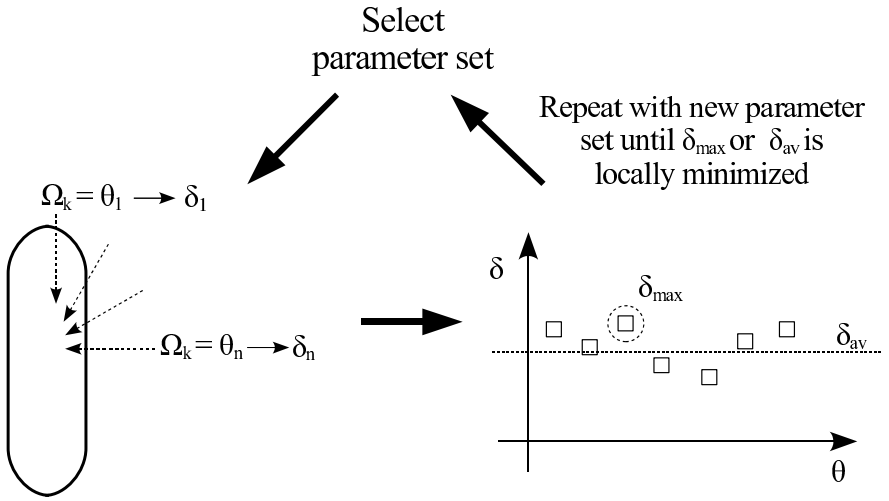

Figure 3.10: *An optimization cycle, where the errors are the δ_{L_2} integral errors for each input field. The cycle continues until we find a local minimum in either the maximum or average δ_{L_2} for all the input fields considered.*

optimization procedure in Fig. 3.10 involves

1. Selecting an initial guess set of parameters

2. For this parameter set, calculating δ_{L_2} for a series of input fields for various Ω_k incident upon the particle

3. Comparing the δ_{L_2} errors calculated for each input field and storing either the maximum or average δ_{L_2} error

4. Repeating this cycle a number of times with a series of new parameter sets until a set is found that locally minimizes the average or maximum δ_{L_2}.

Very careful attention must be paid to the notions of average and maximum errors used in this context. Explicitly, these refer to the maximum and average δ_{L_2} surface integral errors of **a series of input fields**. That is, each input field incident upon the particle has a single surface integral error associated with it. So a series of n input fields would produce a series of n errors which we aim to minimize in a maximum or averaged sense. This is different form the notions of average and maximum errors discussed in Chapter. 2, where the maximum and average refer to the errors as a function of angular position of the matching point for a **single input field**.

We now have a clear understanding of the meaning of the average and maximum δ_{L_2} surface errors, we must decide on which measure we wish to optimize. Since we aim for our SGF's to be as flexible as possible and to be able to find accurate solutions for any incident field, we choose in this work to optimize on the maximum error. In this way, providing we subject our particle to a sufficiently high number of incident fields in our optimization procedure, we can state the optimized surface error in such a way that **any** incident field on the particle will produce an error result below our optimized value. In this way, our optimized maximum surface integral error δ_{L_2} forms an upper bound on the error for the particle in question, thus quantifying the error in the solutions for this particle in a well defined and succinct manner. Furthermore, if we evaluate the average and maximum δ_{L_2} errors we see that they are often comparable, thus indicating that the maximum error is reasonable choice for the overall level of the error in our optimization procedures.

	one parameter set for all modes	separate parameter sets for each mode
Dielectric particle, average δ_{L_2}	5.792×10^{-6}	2.167×10^{-6}
Dielectric particle, maximum δ_{L_2}	7.629×10^{-6}	$\mathbf{3.840 \times 10^{-6}}$
Gold particle, average δ_{L_2}	5.629×10^{-5}	2.968×10^{-5}
Gold particle, maximum δ_{L_2}	9.854×10^{-5}	$\mathbf{3.227 \times 10^{-5}}$

Table 3.1: *Comparison of the optimization calculations for two example particles, an ellipsoidal prolate dielectric with $SP = 12$, $AR = 5.5$ and a gold oblate rounded cylinder with $SP = 5.5$, $AR = 3$. The selected optimized errors for these particles are shown in bold.*

We can tie up our discussion regarding the optimization options with respect to treatment of azimuthal modes and specific error measures on which to optimize in Table 3.1, where we compare the options for two typical example particles, both calculated for $M = 4$ modes and subject to ten incident fields during the optimization procedure between $\Omega_k = 0°..90°$. From Table 3.1 we can see that optimizing on each mode individually does indeed produce lower errors than optimizing for all modes with one parameter set. We also see that the average and maximum δ_{L_2} surface integral errors are comparable. Throughout the rest of this work, the stated δ_{L_2} surface integral errors will refer to the optimized maximum errors over a set of input fields unless otherwise stated.

3.3.4 Optimization results; families of particles

We aim for the SGF method presented in this work to be applicable for a wide range of axisymmetric particles and we have laid down in Section. 3.3.3 an optimization procedure which aims to maximize the range of particles that can be studied by minimizing our maximum integral surface error over a range of input fields. We aim in this section to highlight the flexibility of the SGF method by studying families of particles which range from being elongated to flat, as depicted in Fig. 3.11.

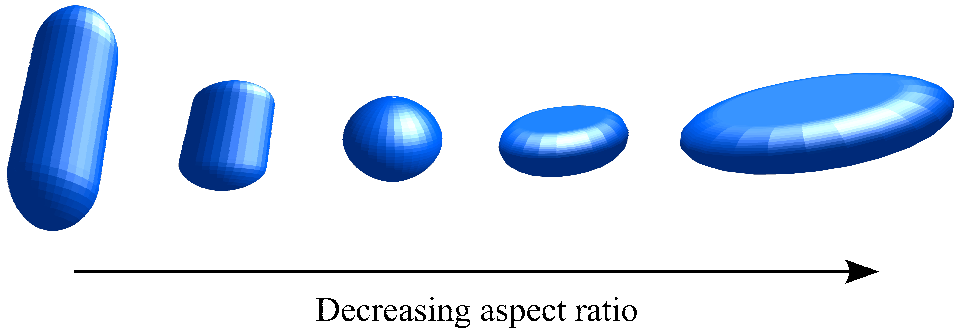

Figure 3.11: *A diagramatical representation of a family of axisymmetric particles ranging from prolate to oblate, highlighting the drastically different geometries.*

Results for particle families

If we carry out an optimization procedure on families of gold and dielectric particles, ranging from elongated to flat we may study the error in our solutions as a function of aspect ratio as shown in Fig. 3.12. For these families we optimize each particle over a set of ten input waves ranging from $\Omega_k = 0°..90°$ in equally spaced increments. As we make note of in the caption, the error in Fig. 3.12 is the total error for the particles, i.e. we have optimized each mode individually thus producing a set of optimal parameters for each mode and then evaluated the total errors by summing the errors for each mode as outlined in Eqn. 3.12. We note that the optimization produces a wide and flat distribution of errors across the families of aspect ratios. There is only significant deviation at the extreme edges and when the particle is close to spherical, as we would expect.

Additionally, we may directly observe the action of the optimization procedure as it minimizes the error as we "walk" through the parameter space. We show in Fig. 3.13 the various steps in the optimization procedure for a dielectric particle of AR 1/5 for the mode $m = 1$ contained in Fig. 3.12. Note that although each step in Fig. 3.13 decreases the error, the optimization procedure in fact evaluates a range of parameters between each step and

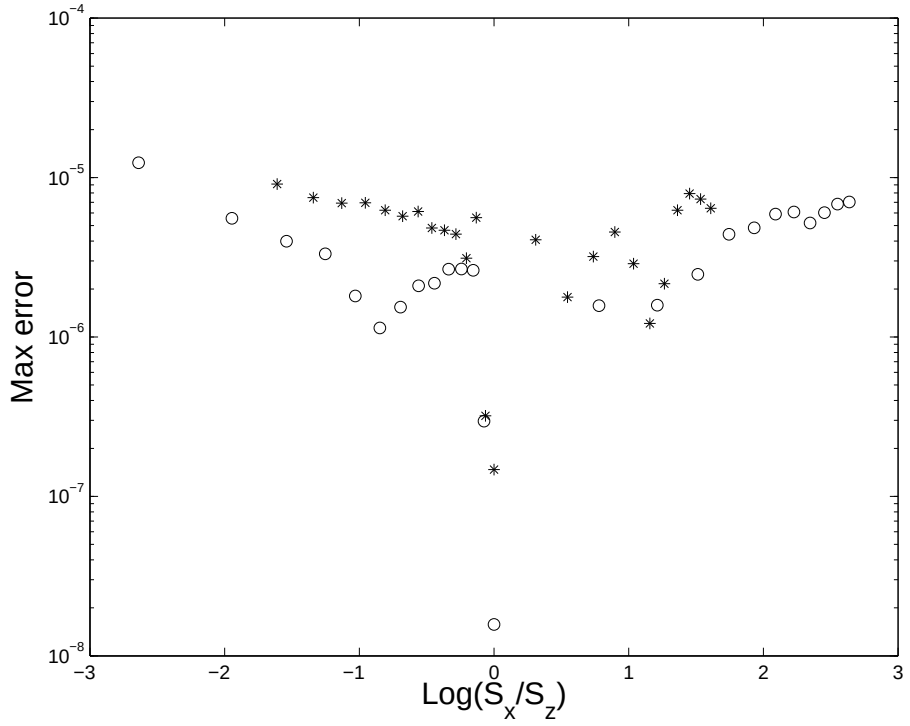

Figure 3.12: *The variation in total (summed over all m) optimized maximum surface integral errors δ_{L_2} as a function of aspect ratio (S_x/S_z where $S_{x,z}$ are the lengths of the particle along the x and z axes respectively) for families of dielectric (circles) and gold particles (stars).*

finds the lowest error out of these intermediate parameter sets and selects it as the next optimization point. These intermediate spikes with higher error have been omitted from the graph as they are not optimal error points in the section of the parameter space that has been examined at each step. The process is repeated until the last point (a local minimum) is reached.

3.4 Experimentally measurable optical effects

So far in this study in the far field we have only studied the DSCS. Although the DSCS is a very useful measure of the electromagnetic properties of particles, it is experimentally not practical to measure and as such we aim to study properties which can be easily evaluated experimentally. Probably the

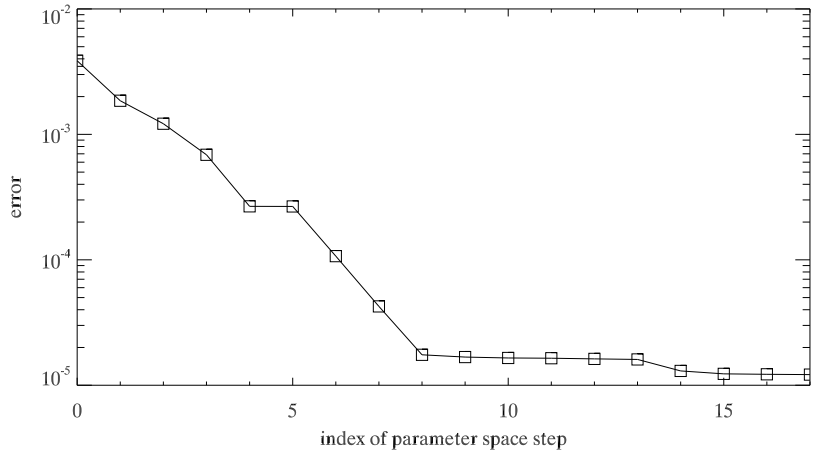

Figure 3.13: *δ_{L_2} maximum surface error for a dielectric particle as a function of position in the three dimensional parameter space of our optimization. Each iteration in the process moves the error to a lower (or equal) error value until a local minimum is obtained at step 17. The value at step 17 is our optimized error for the mode $m = 1$ for this particle. Note that the index of iteration physically corresponds to a move along any of the three orthogonal directions in our parameter space, the direction of the "walk" in the parameter space is not indicated.*

most simple property of a particle that can be easily measured is the amount of power that it removes from a beam incident upon it. The power removed from the beam is due to scattering and absorption by the particle and is determined by the the extinction cross section, C_{ext}. The extinction cross section is defined in the optical theorem [65]- a fundamental theorem in wave scattering theory as:

$$C_{ext} = \frac{4\pi}{k_s|\mathbf{E}_0|^2} Im\{\mathbf{E}_0^* \cdot \mathbf{E}_{s\infty}(e_{\mathbf{\Omega_k}})\} \tag{3.16}$$

This gives the relation between the total amount of radiation scattered or absorbed as a function of the amplitude of the scattered field in the forward direction $e_{\mathbf{\Omega_k}}$. Because of this relationship, the optical theorem is sometimes referred to as the extinction or forward scattering theorem. This simple

formulation allows us to readily compute the extinction cross section from the asymptotic form of the electric field in the forward direction, which we already calculate as part of the DSCS. The extinction cross section quantifies the combined effect of two physical processes, namely the amount of power both absorbed and scattered by a particle. We therefore define separate cross sections for the various processes:

$$C_{ext} = C_{scat} + C_{abs} \tag{3.17}$$

where C_{scat} is the **total** scattering cross section and C_{abs} is the absorption cross section. For the total scattering cross section we move from the concept of the relative angular amplitude of the scattered radiation at infinity (the DSCS) to a measure of the **total** amount of radiation scattered by the particle over the solid angle $\Omega = 4\pi$. Thus the total scattering cross section is defined in terms of the integral [65]:

$$C_{scat} = \frac{1}{|\mathbf{E}_0|^2} \int_{4\pi} \sigma^s d\Omega \tag{3.18}$$

where we have integrated the DSCS over the solid angle $\Omega = 4\pi$, and divided by the amplitude of the incoming wave such that C_{scat} gives the fractional size of the incoming wave amplitude scattered by the particle over $\Omega = 4\pi$. In much the same way as we defined the total scattering cross section, we can define an absorption cross section as a coefficient which indicates the amount of power absorbed by the particle. Since we can calculate directly C_{ext} and C_{scat}, by using Eqn.(3.17) we can find C_{abs} trivially via:

$$C_{abs} = C_{ext} - C_{scat} \tag{3.19}$$

We note that for non-absorbing particles (such as the dielectrics we study in this work) $C_{abs} = 0$ and so $C_{ext} = C_{scat}$, i.e. the only removal of power from the incident beam is due to scattering by the particle.

We have now defined the cross sections of a particle which quantify how much power has been removed form a beam incident upon it and found relations that relate the proportions of power lost via the processes of scattering and absorption. However, typically, we study these parameters as a function of the size parameter or aspect ratio of a range of particles. As such, the cross sections are not directly comparable as the size of the various particles is not constant. In order to account for this we define three corresponding particle efficiencies, which are given by the ratio of the cross sections to the cross sectional area of the particle perpendicular to the direction of propagation, G, (i.e. the area of the particle "seen" by the incoming wave):

$$Q_{ext} = \frac{C_{ext}}{G} \quad Q_{scat} = \frac{C_{scat}}{G} \quad Q_{abs} = \frac{C_{abs}}{G}. \tag{3.20}$$

By defining these efficiencies, we may study the relative ability of different sized particles to absorb and scatter radiation incident upon them. In Fig.3.14 we show the scattering efficiencies of the optimized gold particle family we studied in Section. 3.3.4. The effect of the angle of incidence is

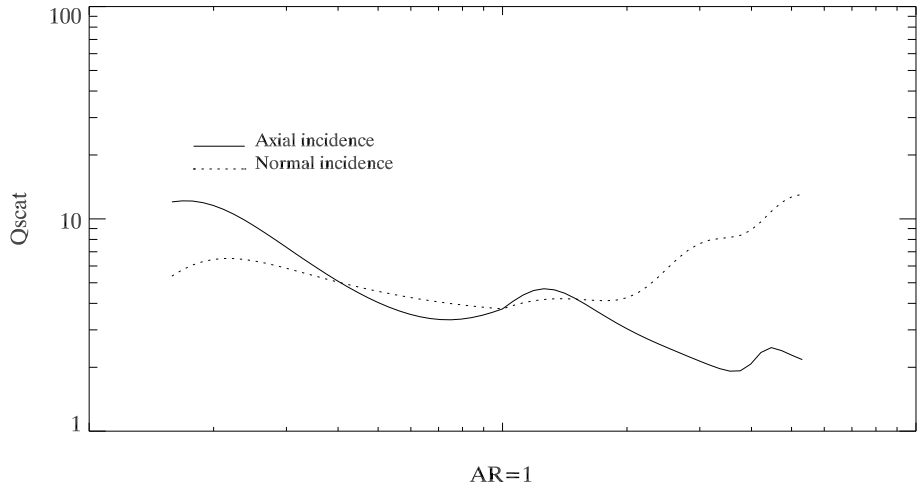

Figure 3.14: *The scattering efficiencies (arbitrary units) of the family of optimized gold particles studied in Section. 3.3.4. At $AR = 1$ the particles are spheres.*

very obvious in Fig.3.14, this shows that depending on the angle of incidence, the scattering properties of the particles can be very different.

3.5 Near field detail and internal field

One of the major advantages over the SGF method over methods which discretize the particle volume or have areas where the field solution is unknown (such as FDTD and EBCM respectively) is the ability to resolve the fields of interest at any point in space. The limitations of the EBCM in the near field are apparent, as there are large areas between the inscribing and superscribing spheres to the particle where the field is unknown. However, this is a method principally used for far field simulations. With discretizing methods such as FDTD, however, the method is primarily targeted at near field modelling. One of the main disadvantages of this method is that there is always a degree of staircasing in the solution, as discussed in Section. 1.5.2. This is where there are discontinuities in the field at the particle edges due to the discretizing of the space that are an unavoidable aspect of the solution method. For certain materials, particularly real metals, the most interesting area we wish to study is precisely the surface of the particle itself and so this can be problematic. With the SGF method, however, there is no staircasing in the boundary and as a result we may produce near field plots on any scale without showing field discontinuities due to approximations in the surface shape. This makes the SGF method an ideal approach in studying the near field and surface effects of particles, particularly in real metals. We have shown many such examples throughout this work.

There are further problems with methods that approximate metals as being perfect conductors when in reality they have finite conductivity. In these methods the internal field is artificially set to zero. In the SGF method, however, by using the real finite conductivities of materials we can model how the internal field varies even within real metals. In Fig. 3.15 we show

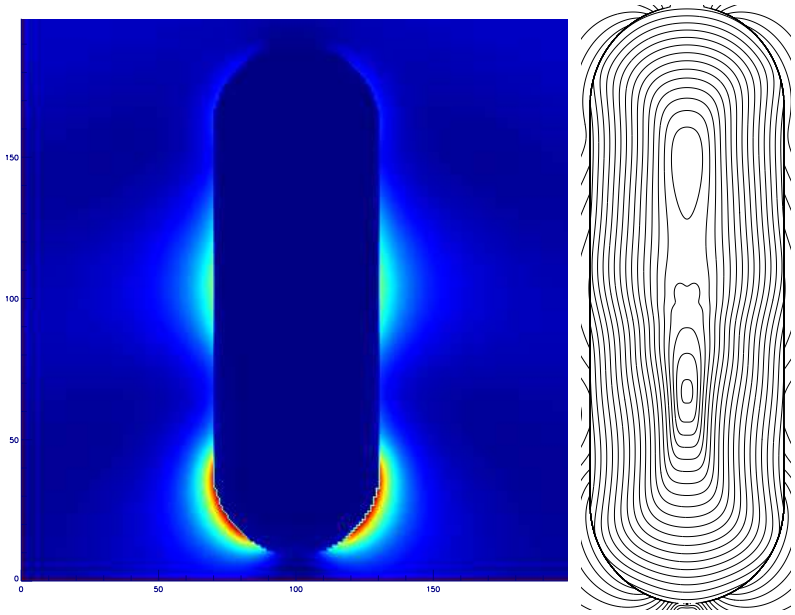

Figure 3.15: *A standard near field image of a gold rounded cylinder illuminated axially and a near field contour plot on a log scale of the same particle.*

a regular near field image of a gold prolate rounded cylinder under axial incidence ($\Omega_k = 0°$). Observing near field variations within the particle is difficult on a linear scale and when using colour plots. We therefore also show on Fig. 3.15 a log contour plot of the intensity in the interior of the particle showing the field variation. We note that this plot is somewhat artificial since it is on a log scale, but it does serve to highlight that we have field permeating into the particle (albeit a vanishingly small intensity) and being attenuated to a very low level at the center.

3.6 Qualitative near field analysis

For the particles investigated in Section. 3.3.4 our optimization procedure leads to errors below the convergence threshold. This allows us to study the effect of the particle's shape and the direction of incidence field on sur-

face fields.. The optimal distribution of distributed sources and the analytical form of their fields allow us to analyze qualitatively the position of the sharpest and most intense spots around the particle, a problem of great practical relevance. The brightest and sharpest spots will be in a region of space where a relatively large number of multipole fields have one or two components in phase. This will depend on the phase of the coefficients of our expansion functions that, for a given incident field, depends on the geometry and the relative refractive index of the particles. By looking at the optimal distribution of the distributed sources and at the analytical form of their fields we can see that points along the symmetry axis for rods have two special properties: they have the same angular coordinates in all spherical systems centered on the multipolar sources, and the radial component of the total field at these points is the sum of the radial components of the multipoles, and similarly for each of the two tangential components. We can see that these points are most likely to have many multipoles with one or two components in phase when the direction of incidence is at 0°. This produces a bright or a dark region depending on the relative phase between the corresponding components of scattered and incident fields. For disks a similar situation happens at points on the equatorial plane when the direction of incidence is at 90°. In both cases, the incident wave is perpendicular to the smallest section of the particles. This analysis does not distinguish between backward and forward directions but, for the dielectric and metallic particles considered here, we expect the sharpest and brightest intensity spots to appear on the shadow area because, for these angles of incidence, the flow of energy is larger in the forward than in the backward direction. Bright spots can be found in other positions for different angles of incidence, but will in general be less sharp. When the direction of incidence is orthogonal to the largest section, a similar analysis shows that multipoles of a given order have fields components that are almost in phase on straight sections orthogonal to the direction of incidence, if the expansion coefficients are in phase. When

the incident field is a plane wave, this leads to the formation of standing waves in the backward direction, even when most energy is scattered in the forward direction.

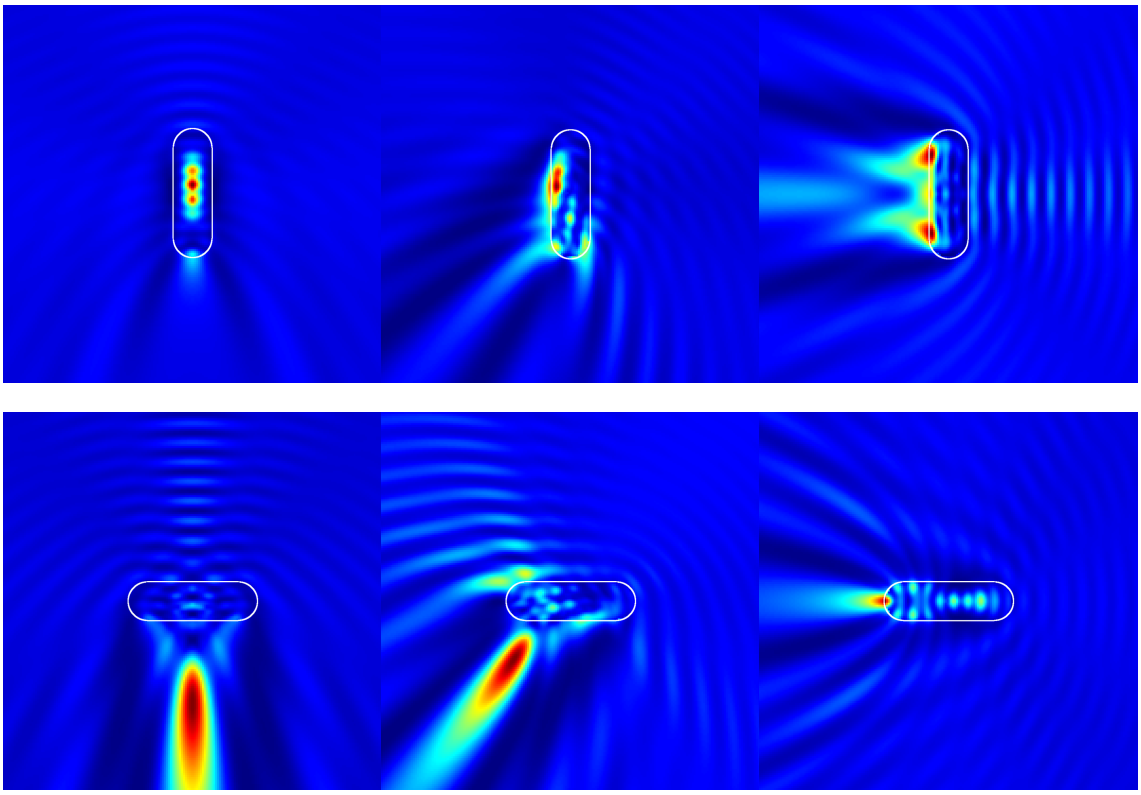

Figure 3.16: *Near field electric field intensity plots for elongated and flat dielectric particles with incident excitation at* 0° *(left column),* 40° *(middle column) and* 90° *(right column) to the symmetry axis.*

This qualitative analysis is confirmed by a quantitative numerical investigation. We show the near field results for both dielectric and metallic prolate and oblate particles calculated in our optimization procedure in Figs.(3.16-3.17). For dielectric rods the region of highest intensity moves from the inside to the outside as the incidence varies from 0° to 90° degrees. For these particles, the most intense points on the surface are not necessarily near the regions of highest curvature. This is very different in dielectric discs, where

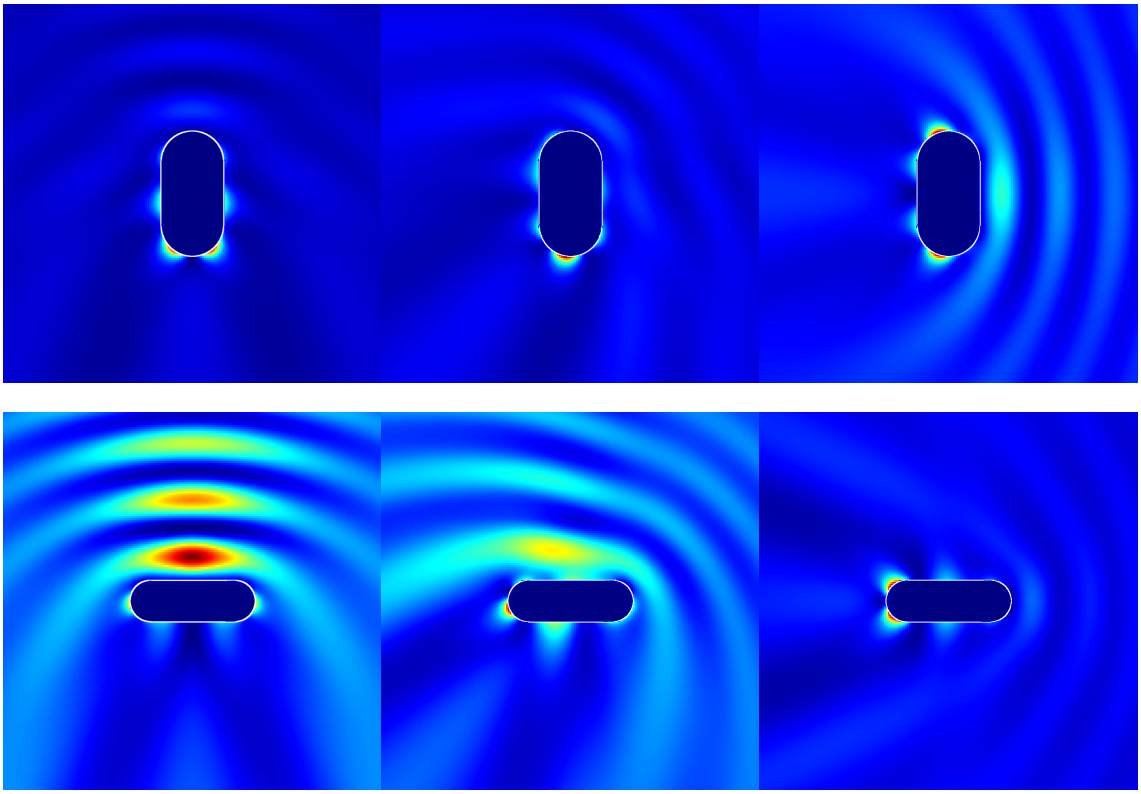

Figure 3.17: *Near field electric field intensity plots for elongated and flat metallic particles with incident excitation at* 0° *(left column),* 40° *(middle column) and* 90° *(right column) to the symmetry axis.*

the region of highest intensity are mostly outside the particle and away from the surface, except at 90°. In both cases, sub-wavelength jets appear on the shadow side, in agreement with the fact that the differential scattering cross section (not shown) is larger in the forward than in the backward direction.

For metals, internal fields are confined very closely to the surface, because of the very strong absorption and small skin depth. High intensity points on the surface are mostly in the regions of high curvature and are strongest in the shadow regions. In agreement with the previous analysis, the sharpest structures are observed with incidence at 0° and 90° for rods and discs, respectively. We also observe the formation of standing waves in the backward direction when the long side is illuminated for both dielectrics and metals.

Chapter 4

Conclusions and Future Work

4.1 Conclusions

In this work we have found accurate optical responses for real metallic and dielectric axisymmetric rods and disks at any point in space in terms of a finite number of exact solutions of the Maxwell equations, by approximating the surface Green function of the particles. We have shown that the choice of the functions we use to carry out this analysis depends on the particle we ultimately model. We found that for spherical particles, we could obtain accurate results by using a set of functions defined solely at the origin of the particle. However, the rapid deterioration in the quality of the solution as the particles became more elongated from spherical required a modification to our theory. For prolate particles, we found that we could greatly improve the conditioning of our system and ultimate error by depositing our sources of radiation on the symmetry axis of the particle. Furthermore, for oblate particles, we have shown that by placing our sources on analogue of the symmetry axis in the complex plane, we could also greatly improve our ability to accurately model flat particles. Using these three distinct systems of functions; localized, real distributed and complex distributed we have studied both the near and far field optical properties for a variety of particles. In

doing so we shown that in the far field our results match exactly to the accepted results in literature, namely Mie theory for spheres and the Extended Boundary Condition Method (EBCM) for elongated and flat particles. However, since the field solutions for the SGF method are valid at all points in space, we have also been able to study the near field properties of particles, a feat not possible with the EBCM. We have examined near field effects for dielectric particles, such as photonic nanojets, which are an active and exciting area of current research with many potential applications. For metallic particles, we have seen that we could effectively find the position of surface hot spots on the particle, without approximating our particle as being spherical, infinitely extending or perfectly conducting - approximations often used in computational electromagnetics. The complete optical characterization of these real metallic particles is one of great current interest across many areas of nanoscience, for instance in Surface Enhanced Raman Spectroscopy and Surface Enhanced Fluorescence.

In Chapter. 3, we made several important refinements our theory and method. We formulated mathematically well defined representations of our errors and outlined efficient numerical methods of evaluating these errors. We also examined in detail the relative importance of various parameters on our solution error. By doing so, we saw that we could find optimized SGF's which minimized our error for a series of input fields and defined the maximum error for our solutions for any input field at any point in space. By carrying out this optimization, we studied wide families of dielectric and real metallic particles with a tight control over the surface error. This enabled us to accurately investigate how the size, shape and composition of the particles affected the distribution of near field intensity. We also investigated the behavior in the far field of particles which can be measured experimentally, and have shown high resolution near field images without staircased boundaries and with real internal fields.

4.2 Future work

There are several potential modifications to our method that are currently being developed or could possibly be implemented.

By using our optimization procedure, it is theoretically possible to define an *a priori* estimate to the error for any possible incident field on a particular particle. This would be a significant improvement on our method since in the work presented we have only an *a posteriori* error which is found by the solution of a particular problem. Work in this area is currently partially complete.

As discussed, one of the major problems in dealing with metallic particles is the complex refractive index which causes rapid oscillations in the special functions we employ at the particle surface. One possible modification would be to rescale the special functions such that the rapid oscillations are minimized [66]. At present, the rescaled functions have been partially implemented.

The procedure outlined in this work could also be implemented to solve the reciprocal problem of the scattering of a bubble inside a medium, in this case we would require more functions to expand the scattered field than the internal field, the opposite of the case for the problems we solve in this work. This work has not been yet studied, however the computer codes in their current form could be used to solve this problem with minimal editing.

We discussed that the truncation parameter of the SVD was one of the parameters over which we optimized. By studying the error that resulted from the solution of linear systems at different levels of truncation within our singular value spectrum, we found, semi-quantitatively that the optimal position of the truncation should be just above the lower plateau in the spectrum. We assigned this plateau to be the noise level, and designed optimization procedures to locate it. A more efficient method of optimization, based on this analysis would be to curve fit the total spectrum of the singular values and truncate at the last value below the maximum in the second order

derivative of the spectrum. In this way, the singular value spectrum would not need to be sampled at various levels during the optimization procedure and computational cost could be saved.

More general future research involves using the theory laid down in this work to try to determine the position and orientation of single molecules and examine optical trapping forces especially with respect to single molecules. Additionally, this work could be expanded to determine resonances and hot spots of photonic particles and clusters of such particles and to calculate of the the energy levels of the composite system made of a multilevel quantum system and a photonic cluster as a function of the relative position and orientation between the molecule and photonic structure.

Appendix A

Coordinate systems

Throughout this work will use both Cartesian and spherical polar coordinates and the relationships between these must be clearly established for the avoidance of doubt. The diagramatical representation of the re relationship between the two systems is shown below in figure A.1:

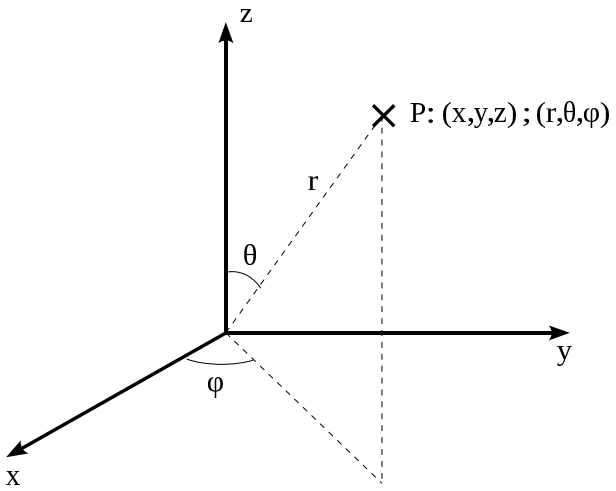

Figure A.1: *Diagramatical relationship between a point expressed in both the Cartesian and Spherical Coordinate systems.*

where

$$x, y, z \in (-\infty, \infty) \tag{A.1}$$

and

$$r \in [0, \infty) \tag{A.2}$$

$$\theta \in [0, \pi] \tag{A.3}$$

$$\phi \in [0, 2\pi) \tag{A.4}$$

From Fig. A.1, it can be seen that:

r is the distance from the origin to a given point P

θ is the angle between the positive z-axis and the line formed between the origin and P.

ϕ is the angle between the positive x-axis and the line from the origin to the P projected onto the $x - y$-plane.

Explicitly:

$$r = \sqrt{x^2 + y^2 + z^2} \tag{A.5}$$

$$\theta = \arccos z/r \tag{A.6}$$

$$\phi = \arctan y/x \tag{A.7}$$

and, conversely

$$x = r \sin\theta \cos\phi \tag{A.8}$$

$$y = r \sin\theta \sin\phi \tag{A.9}$$

$$z = r \cos\theta \tag{A.10}$$

As a result, the unit vectors can be related by the matrix:

$$\begin{bmatrix} \hat{\mathbf{r}} \\ \hat{\boldsymbol{\theta}} \\ \hat{\boldsymbol{\phi}} \end{bmatrix} \begin{bmatrix} \sin\theta\cos\phi & \sin\theta\sin\phi & \cos\theta \\ \cos\theta\cos\phi & \cos\theta\sin\phi & -\sin\theta \\ -\sin\phi & \cos\phi & 0 \end{bmatrix} = \begin{bmatrix} \hat{\mathbf{x}} \\ \hat{\mathbf{y}} \\ \hat{\mathbf{z}} \end{bmatrix} \tag{A.11}$$

It should be noted that this matrix is orthogonal, and as such, its inverse is

simply its transpose :

$$\begin{bmatrix} \hat{\mathbf{x}} \\ \hat{\mathbf{y}} \\ \hat{\mathbf{z}} \end{bmatrix} \begin{bmatrix} \sin\theta\cos\phi & \cos\theta\cos\phi & -\sin\phi \\ \sin\theta\sin\phi & \cos\theta\sin\phi & \cos\phi \\ \cos\theta & -\sin\theta & 0 \end{bmatrix} = \begin{bmatrix} \hat{\mathbf{r}} \\ \hat{\boldsymbol{\theta}} \\ \hat{\boldsymbol{\phi}} \end{bmatrix} \tag{A.12}$$

Appendix B

Spherical Vector Wave-Functions

A basic understanding of various special functions used in this work will be assumed, although the reader is directed to [67] for further details of fundamental special functions. We shall highlight the structure of some of the important vector functions used in this work which are built from a combination of these basic special functions. The Spherical Vector Wavefunctions (SVWF's) are defined (in such a way as to be consistent with [34]) as the product:

$$\mathbf{M}_{mn}^{1,3}(r,\theta,\phi) = z_n^{1,3}(kr)\mathbf{m}_{mn}(\theta,\phi), \tag{B.1}$$

$$\mathbf{N}_{mn}^{1,3}(r,\theta,\phi) = z_n^{1,3}(kr)\mathbf{n}_{mn}(\theta,\phi) = k^{-1}\nabla\times\mathbf{M}_{mn}^{1,3}(r,\theta,\phi) \tag{B.2}$$

where the indices $1,3$ refer to the regular and radiating functions and $z_n^{1,3}(kr)$ are the spherical Bessel and Hankel functions respectively. The angular functions $\mathbf{m}_{mn}, \mathbf{n}_{mn}$ are the vector spherical harmonics and are given by

$$\mathbf{m}_{mn}(\theta,\phi) = \frac{i}{\sqrt{n(n+1)}}(\hat{\boldsymbol{\theta}}\frac{im}{\sin\theta} - \hat{\boldsymbol{\phi}}\partial_\theta)Y_{mn}(\theta,\phi), \tag{B.3}$$

$$\mathbf{n}_{mn}(\theta,\phi) = \frac{i}{\sqrt{n(n+1)}}(\hat{\boldsymbol{\theta}}\partial_\phi + \hat{\boldsymbol{\phi}}\frac{im}{\sin\theta})Y_{mn}(\theta,\phi) \tag{B.4}$$

where Y_{mn} are the usual spherical harmonics [68].

Appendix C

Unitary normal and elemental area

It is necessary in our analysis to find both the unitary normal at a surface of a particle as well as the unitary area element. The unitary normal at a point on the surface in spherical polar coordinates is given by

$$\hat{\mathbf{n}}_+ = \frac{\frac{\partial \mathbf{r}}{\partial \theta} \times \frac{\partial \mathbf{r}}{\partial \phi}}{\left| \frac{\partial \mathbf{r}}{\partial \theta} \times \frac{\partial \mathbf{r}}{\partial \phi} \right|} \tag{C.1}$$

where $\mathbf{r}$ is the vector from the origin to the surface point and

$$\frac{\partial r}{\partial \theta} \times \frac{\partial r}{\partial \phi} = r^2 \sin\theta \hat{\mathbf{r}} - r \sin\theta \frac{\partial \mathbf{r}}{\partial \theta} \hat{\boldsymbol{\theta}} - r \frac{\partial \mathbf{r}}{\partial \phi} \hat{\boldsymbol{\phi}} \tag{C.2}$$

where $r = |\mathbf{r}|$, i.e. $\mathbf{r} = r\hat{\mathbf{r}}$. In our studies we consider particles which are axisymmetric in ϕ and we solve our problem on the generatrix. In this case, the last term in Eqn. C.2 is zero. Also of importance to our analysis is the element of surface area on the scattering object, dA. This is related to the unitary normal by

$$dA = \left| \frac{\partial \mathbf{r}}{\partial \theta} \times \frac{\partial \mathbf{r}}{\partial \phi} \right| \tag{C.3}$$

Appendix D

Matrix inverses

D.1 Matrix inverses

Matrix inverses are used in many areas of mathematics, statistics and the sciences and are crucial in the solution of systems of equations. Depending on the specific nature of the matrix which is to be inverted, we may use different techniques to calculate the inverse, if one exists.

D.2 True inverse

There is often confusion surrounding the nature of inverses of matrices, and the term 'inverse' is often used to refer to different procedures depending on the specific matrix in question. The true matrix inverse is defined only for square matrices, but not all square matrices have an inverse. A matrix $\mathbf{A}$ which has an inverse $\mathbf{A}^{-1}$ is said to be invertible and the original and inverse matrices are related by

$$\mathbf{A}\mathbf{A}^{-1} = \mathbf{A}^{-1}\mathbf{A} = \mathbf{I_n} \tag{D.1}$$

where $\mathbf{A}$ and $\mathbf{A}^{-1}$ are both $n \times n$ matrices and $\mathbf{I}_n$ is the identity matrix, also of size $n \times n$. Invertible matrices have many additional properties which we may not make use of and need not discuss here, but an exhaustive list of

these properties is provided in [69]. As previously mentioned, not all matrices are invertible and matrices which do not have an inverse are called singular or degenerate. Below, we give two simple examples of $2x2$ matrices, one of which is invertible and one of which is singular. For $2x2$ matrices, there is a simple formula which provides the inverse of a matrix:

$$\mathbf{A}^{-1} = \begin{bmatrix} a & b \\ c & d \end{bmatrix}^{-1} = \frac{1}{ad - bc} \begin{bmatrix} d & -b \\ -c & a \end{bmatrix} \tag{D.2}$$

so it can be easily seen that the matrix

$$\begin{bmatrix} 6 & -2 \\ 9 & 3 \end{bmatrix} \tag{D.3}$$

has an inverse since $ad - bc \neq 0$, while the similar matrix

$$\begin{bmatrix} 6 & -2 \\ -9 & 3 \end{bmatrix} \tag{D.4}$$

does not since the term $ad - bc = 0$ produces a singularity. For larger matrices, analytical expressions become numerically intractable however there are techniques which can be employed to find the inverse of invertible matrices, such as Gaussian elimination [70].

D.3 Generalized inverse

For non square matrices, the matrix inverse is not defined. There does exist, however, a generalization of the matrix inverse which has some of the properties associated with real inverse but not necessarily all of them. This generalized inverse is often called the Pseudoinverse or the Moore-Penrose pseudoinverse, described independently by E. H. Moore and R. Penrose in 1920 and 1955 respectively [71, 72]. Throughout this work the term pseu-

doinverse will be used to refer to the Moore-Penrose pseudoinverse. The pseudoinverse of an $m \times n$ matrix $\mathbf{A}$ with entries $a_{ij} \in \mathbb{C}$ is the $n \times m$ matrix $\mathbf{A}^+$ which also has entries $a_{ij}^+ \in \mathbb{C}$. A unique pseudoinverse exists for any matrix and must must satisfy the criteria:

1. $\mathbf{A}\mathbf{A}^+\mathbf{A} = \mathbf{A}$. Note that $\mathbf{A}\mathbf{A}^+$ is not in general the identity matrix.
2. $\mathbf{A}^+\mathbf{A}\mathbf{A}^+ = \mathbf{A}^+$
3. $(\mathbf{A}\mathbf{A}^+)^H = \mathbf{A}\mathbf{A}^+$. Where H is the Hermitian, or conjugate transpose. Therefore $\mathbf{A}\mathbf{A}^+$ is Hermitian.
4. $(\mathbf{A}^+\mathbf{A})^H = \mathbf{A}^+\mathbf{A}$. $\mathbf{A}^+\mathbf{A}$ is also Hermitian.

As with the real inverse, the pseudoinverse has many properties which we will not discuss here, but an exhaustive list is provided in [49].

Bibliography

[1] P. Ferrand. *Optics Express*, 16:6930, 2008.

[2] M. Sax I. Freestone, N. Meeks and C. Higgitt. A roman nanotechnology. *Gold Bull.*, 40:270, 2007.

[3] M. Faraday. The bakerian lecture: experimental relations of gold (and other metals) to light. *Philosophical Transactions of the Royal Society of London*, page 145, 1847.

[4] Rayleigh. *Phil. Mag*, 41:107120, 1871.

[5] H. Zimmer. *Geometrical optics*. Springer, 1979.

[6] G. Mie. Beitraege zur optik trueber medien, speziell kolloidaler metalosungen. *Annales de Physik*, 25:337–445, 1908.

[7] C. Castro. *Nanoparticles from Mechanical Attrition*. American Scientic Publishers, 2002.

[8] J.M.A. Caiu. Elaboration of boehmite nano-powders by spray-pyrolysis. *Powder Technology*, 190:95–98, 2009.

[9] M. Daniel and D. Astruc. Gold nanoparticles: Assembly, supramolecular chemistry, quantum-size-related properties, and applications toward biology, catalysis and nanotechnology. *Chem. Rev.*, 104:293–346, 2004.

[10] J. Champion. *Proc. Nat. Acad. Sci.*, 104:11901, 2007.

[11] T. Wriedt. E. Eremina, Y. Eremin. Review of light scattering by fiber particles with a high aspect ratio. *Recent Res. Devel. Optics*, 3:297–318, 2003.

[12] S. Dermott E. Green, B.Gustafson. *Interplanetary Dust*. Springer, 2001.

[13] W. A. Challener A. V. Itagi. Optics of photonic nanojets. *J. Opt. Soc. Am.*, 22:2847–2858, 2005.

[14] X. Cui. *Optics Express*, 16:13560, 2008.

[15] A.Taflove S. Kong, A.Sahakian and V.Backman. Photonic nanojet-enabled optical data storage. *Optics Express*, 16(18):13713–13719, 2008.

[16] A. Taflove Z. Chen and V. Backman. Photonic nanojet enhancement of backscattering of light by nanoparticles: a potential novel visible-light ultramicroscopy technique. *Optics Express*, 12:1214–1220, 2004.

[17] A. Ashkin and J.M. Dziedzic. *Phys. Rev. Lett.*, 38:1351, 1977.

[18] J. R. Buck and H. J. Kimble. *Physical Review A*, 67, 2003.

[19] F. Vollmer. *Applied Physics Letters*, 80:4057, 2002.

[20] P. Jain. Review of some interesting surface plasmon resonance-enhanced properties of noble metal nanoparticles and their applications to biosystems. *Plasmonics*, 2:107, 2007.

[21] M. El-Sayed. *Acc Chem Res*, 34:257, 2001.

[22] K. Kelly. *J Phys Chem*, 107:668, 2003.

[23] S. Ghosh. *J Phys Chem*, 108:13963, 2004.

[24] K. Su. *Nano Lett*, 3:1087, 2003.

[25] N. Rosi. *Chem Rev*, 105:1547, 2005.

[26] V. Zharov. *Laser Med Surg*, 37:219, 2005.

[27] A. Haes. *Nano Lett*, 4:1029, 2004.

[28] C. Chen. *Phys Rev B*, 27:1965, 1983.

[29] K. Aslan. *Curr Opin Chem Biol*, 49:538, 2005.

[30] B. Nikoobakht. *Chem Phys Lett*, 17:336, 2002.

[31] J. Hulteen. *J Vac Sci Technol A*, 13:1553, 1995.

[32] J. Jiang. *J Phys Chem B*, 107:9964, 2003.

[33] S. Nie. *Science*, 275:1102, 1997.

[34] J. Jackson. *Classical Electrodynamics*. Wiley, 1998.

[35] A. Taflove. *Computational electrodynamics: the finite difference time-domain method*. Artech House, 1995.

[36] R. Landau. *Computational physics: problem solving with computers*. Wiley, 2007.

[37] C. Pennypacker E. Purcell. *Astrophys. J.*, 186:705, 1973.

[38] P.C. Waterman. Matrix formulation of electromagnetic scattering. *Proc. IEEE*, 53:805, 1965.

[39] Y. Eremin A. Doicu, T. Wriedt. *Light Scattering by Systems of Particles*, pages 295–301. Springer, 2006.

[40] T. Wriedt. *Journal of Quantitative Spectroscopy and Radiative Transfer*, 106:535, 2007.

[41] F. Odeh. *Uniqueness theorems under the radiation condition*. University of California Press, 1961.

[42] M. Buhmann. *Radial basis functions: theory and implementations*. Cambridge University Press, 2003.

[43] T. Wriedt. *Generalized multipole techniques for electromagnetic and light scattering*. Elsevier, 1999.

[44] T. Rother. Self-consistent green's function formalism for acoustic and light scattering. *Optics Communications*, 251:254–269, 2005.

[45] F. Papoff K. Holms, B. Hourahine. *J. Opt. A: Pure Appl. Opt.*, 11:389–391, 2009.

[46] A. Bjorck. *Numerical Methods for Least Squares Problems*. SIAM, 1996.

[47] J. Gentle. *Numerical Linear Algebra for Applications in Statistics*, pages 102–103. Berlin: Springer-Verlag, 1998.

[48] M. Kahnert. A. Doicu T. Rother and J. Wauer. Surface green's functions of the helmholtz equation in spherical coordinates. *Prog. Electromag. Res.*, 38:47–95, 2002.

[49] C. Loan G. Goulb. *Matrix Computations*. JHU Press, 1996.

[50] D. Cohen A. Ben-Israel. On iterative computation of generalized inverses and associated projections. *SIAM Journal on Numerical Analysis*, 3:410, 1966.

[51] T. Wriedt E. Eremina, Y. Eremin. *Optics Communications*, 267:524–529, 2006.

[52] A. Modinos. *Physica A*, 141:575, 1987.

[53] R. Newton. *Scattering theory of waves and particles*. McGraw-Hill, 1966.

[54] S.Hill P. Barber. *Light scattering by particles: computational methods*. World Scientific, 1990.

[55] Y. Eremin A. Doicu, T. Wriedt. *Light Scattering by Systems of Particles*. Springer, 2006.

[56] D. Huffman C. Bohren. *Absorption and Scattering of Light by Small Particles*. Wiley, 1998.

[57] R. Sambles. Gold loses it's lustre. *Nature*, 438:295, 2005.

[58] T. Wriedt A. Doicu. Calculation of the t matrix in the null-field method with discrete sources. 16(10):2539–2544, OCT 1999.

[59] T. Wriedt A. Doicu. Extended boundary condition method with multipole sources located in the complex plane. *Optics Communications*, 139:85–91, 1997.

[60] T. Wriedt. *J. Qual. Spect. Rad. Trans.*, 110:833, 2009.

[61] V. Katz J. Fraleigh. *A first course in abstract algebra*. Addison-Wesley, 2003.

[62] W. Press. *Numerical recipes: the art of scientific computing*. Cambridge University Press, 2007.

[63] P. Hansen. *Rank-deficient and discrete ill-posed problems: numerical aspects of linear inversion*. SIAM, 1998.

[64] S. Wrightl J. Nocedal. *Numerical optimization*. Springer, 1999.

[65] L. Tsang. *Scattering of electromagnetic waves*. Wiley, 2000.

[66] D. M. O'Brien. Radiation from a whip antenna mounted on a sphere. *J. Phys. D: Appl. Phys.*, 13:2185, 1980.

[67] I. Segun M. Abramowitz. *Handbook of Mathematical Functions*. Dover, 1964.

[68] C. Muller. *Spherical Harmonics*. Springer Verlag, 1966.

[69] F. Ayres. *Schaum's Outline of Theory and Problems of Matrices*. Schaum, 1962.

[70] K. Atkinson. *An Introduction to Numerical Analysis*. Wiley, 1989.

[71] E. H. Moore. On the reciprocal of the general algebraic matrix. *Bulletin of the American Mathematical Society*, 26:394, 1920.

[72] R. Penrose. A generalized inverse for matrices. *Proceedings of the Cambridge Philosophical Society*, 51:406, 1955.